Universidade de São Paulo
Instituto de Física

Transporte eletrônico e efeito Hall quântico de spin em poços quânticos de InAs/GaSb

Marcos Henrique Lima de Medeiros

Orientador: Prof. Dr. Luis Gregório G. V. Dias da Silva

Tese apresentada ao Instituto de Física da Universidade de São Paulo, como requisito para a obtenção de Doutorado em Ciências.

Banca Examinadora:
Prof. Dr. Luis Gregório Godoy de Vasconcellos Dias da Silva - Orientador (IFUSP)
Prof. Dr. Felix Guillermo Gonzalez Hernandez (IFUSP)
Prof. Dr. Alexandre Reily Rocha (IFT UNESP)
Prof. Dr. Gerson Ferreira Junior (UFU)
Prof. Dr. Caio Henrique Lewenkopf (UFF)

São Paulo
2022

FICHA CATALOGRÁFICA
Preparada pelo Serviço de Biblioteca e Informação
do Instituto de Física da Universidade de São Paulo

Medeiros, Marcos Henrique Lima de

Transporte eletrônico e efeito Hall quântico de spin em poços quânticos de InAs/GaSb/Electronic transport and quantum spin Hall effect in InAs/GaSb quantum wells. São Paulo, 2022.

Tese (Doutorado) – Universidade de São Paulo. Instituto de Física. Depto. de Física dos Materiais e Mecânica

Orientador: Prof. Dr. Luis Gregório Godoy de Vasconcellos Dias da Silva
Área de Concentração: Física do Estado Sólido

Unitermos: 1. Física computacional; 2. Física do estado sólido; 3. Superfície física.

USP/IF/SBI-034/2022

University of São Paulo
Physics Institute

Electronic transport and quantum spin Hall effect in InAs/GaSb quantum wells

Marcos Henrique Lima de Medeiros

Supervisor: Prof. Dr. Luis Gregório G. V. Dias da Silva

Thesis submitted to the Physics Institute of the University of São Paulo for the acquisition of Doctorate in Science.

Examining Committee:
Prof. Dr. Luis Gregório Godoy de Vasconcellos Dias da Silva - Supervisor (IFUSP)
Prof. Dr. Felix Guillermo Gonzalez Hernandez (IFUSP)
Prof. Dr. Alexandre Reily Rocha (IFT UNESP)
Prof. Dr. Gerson Ferreira Junior (UFU)
Prof. Dr. Caio Henrique Lewenkopf (UFF)

São Paulo
2022

Acknowledgements

Words cannot express my gratitude to professor Luis Gregório Dias da Silva for his invaluable patience, hard work and feedback while supervising me. I also would like to express my deepest gratitude to professor Guilherme Sipahi, and professor Jaroslav Fabian who generously provided knowledge and expertise without which the conclusion of this work would not be possible. Additionally, this endeavor would not have been possible without the generous support from the National Council for Scientific and Technological Development (CNPq), and German Academic Exchange Service who financed my research.

I am also grateful to my classmates and cohort and my office mates, for their contributions during the research, feedback sessions, and moral support. Special thanks for my group mate Raphael Teixeira for his contribution in the paper, as well for Dr. Paulo Faria Júnior and Dr. Denis Kochan for their tutoring during my stay in Regensburg. Thanks should also go to the librarians, research assistants, and study participants from the university of São Paulo and from university of Regensburg, who impacted and inspired me.

Lastly, I would be remiss in not mentioning my family, and my girlfriend Lara Akemi Lucchezi Miyahara, for all love and support. Their belief in me has kept my spirits and motivation high during this process.

Abstract

The challenges inherent to the research of topological insulators in two dimensions based on HgTe/CdTe quantum wells have spurred the search for alternative platforms to study systems exhibiting the quantum Hall effect of spin. In this context, InAs/GaSb semiconductor quantum wells stand out as an alternative. In this work, we focus on the transport properties in InAs/GaSb quantum well systems in the topological regime. Using an effective Hamiltonian obtained from the $k \cdot p$ formalism, it was possible to develop *tight-binding* models for different heterostructure configurations (double and triple wells) based on the set of sites in the discretized position space. Using this model, it was possible to calculate the transport properties in different InAs/GaSb nanostructures by numerical calculations with the KWANT package. In the case of double InAs/GaSb wells, we show the topological transition and the formation of edge states by setting the value of a perpendicular electric field. In particular, oscillations occur in the energy gap as a function of the field, indicating an experimentally measurable signature of the formation of topological edge states. Moreover, for symmetric GaSb/InAs/GaSb triple-well systems, our results show the formation of circular current patterns when the Fermi energy is at the threshold between the bulk bands and the Dirac cone. Since the formation of these circular current patterns coincides with pronounced conductivity peaks, this phenomenon can be associated with the Fabry-Pérot effect. In addition to the main work, the formation of excitons in dichalcogenide monolayers of transition metals was also studied, as well as the phenomenon known as *weak localization* in graphene functionalized with the addition of hydrogen atoms, both works resulting from a stay in the group of prof. Jaroslav Fabian at the University of Regensburg. **Keywords:** quantum spin Hall effect; topological insulators; Landauer's formalism; excitons; graphene.

Resumo

Os desafios inerentes à pesquisa de isolantes topológicos em duas dimensões baseados em poços quânticos de HgTe/CdTe têm fomentado a busca por plataformas alternativas para se estudar sistemas que apresentem o efeito Hall quântico de spin. Neste contexto, poços quânticos semicondutores de InAs/GaSb se destacam como alternativa. Neste trabalho, focamos nas propriedades de transporte em sistemas de poços quânticos de InAs/GaSb no regime topológico. Utilizando um Hamiltoniano efetivo, obtido a partir do formalismo $k \cdot p$, foi possível desenvolver modelos *tight-binding* para diferentes heteroestruturas (poços duplos e triplos) usando como base o conjunto dos sítios do espaço de posições discretizado . A partir desse modelo pôde-se calcular propriedades de transporte em nanoestruturas de InAs/GaSb por meio de cálculos numéricos com o pacote KWANT. No caso de poços duplos InAs/GaSb, mostramos a transição topológica e formação de estados de borda ajustando o valor de um campo elétrico perpendicular. Notavelmente, aparecem oscilações no gap de energia em função do campo, indicando uma assinatura da formação de estados de borda topológicos que pode ser medida experimentalmente. Nossos resultados para sistemas de poços triplos simétricos GaSb/InAs/GaSb também mostram a formação de padrões circulares de corrente quando a energia de Fermi é posicionada no limiar entre as bandas do tipo-bulk e o cone de Dirac. Como a formação desses padrões circulares de corrente coincide com picos na condutância, pode-se associar tal fenômeno ao efeito do tipo Fabry-Pérot. Além do trabalho principal, investigou-se também a formação de excitons em monocamadas dicalcogenetos de metais de transição bem como o fenômeno conhecido por *localização fraca* em grafeno funcionalizado com a adição de átomos de Hidrogênio, ambos os trabalhos resultantes de um período de estadia no grupo do prof. Jaroslav Fabian na Universidade de Regensburg. **Palavras-chave:** efeito Hall de quântico spin; isolantes topológicos; Formalismo de Landauer; excitons; grafeno.

List of Figures

List of Tables

Contents

Chapter 1

Quantum spin Hall insulators

1.1 Introduction

One of the main concerns of condensed matter physics is the discovery and classification of new phases of matter. Large atomic aggregates can give rise to entirely new physical phenomena and exhibit behavior that cannot possibly be predicted by extrapolating the behavior of the individual atomic constituents. Systems classified as crystalline solids, magnetic materials, and superconductors are some of these aggregates. To classify such systems, the traditional paradigm relies on the idea of spontaneous symmetry breaking, itself one of the greatest achievements of condensed matter physics in the last century [9]. According to this paradigm, a crystalline solid is considered to be a system that breaks translational symmetry in space, whereas a magnet breaks rotational symmetry and a superconductor has no gauge symmetry. The Ginzburg-Landau theory [10] is an effective field theory developed to describe such quantum states of matter and its basis is the notion of order parameter related to the symmetries of the system.

In 1980, however, a new phase of matter was discovered whose classification did not fit into the paradigm described. The quantum Hall state [11] consists of a two-dimensional system that has an insulating bulk, but at the same time has a chiral electric current that flows only at the edges of the system sample. This was the first system that is considered topologically different from all other systems known since then. Moreover, the Hall conductance (quantized in units of e^2/h) is the first topological invariant adopted in the classification of a material phase [12, 13].

Topology is the branch of mathematics that deals with the global aspects of geometric objects independent of their local features. The traditional example is that the surface of a cup and the surface of a torus are considered topologically equivalent, since one can be deformed into the other without cuts or breaks. In this classical example, the number of holes in the object acts as a topological invariant which, more precisely and mathematically, can be translated as an integral of the Gaussian curvature over the entire surface, i.e., the *genus number*.

The concept of "smooth deformation" is central to the topological classification of quantum phases of matter. As mentioned earlier, mathematically we call a deformation of a geometric object smooth if there are no breaks or cuts during the deformation process, i.e., if there are no holes opening, holes closing, or cuts of any kind. Thus, two objects are said to belong to the same equivalent topological class if it is possible to transform one object into the other by applying only smooth deformations. If the objects are physical systems such as insulators and superconductors, we can study their Hamiltonians and define an equivalence class for systems with a gapped band structure. According to such a classification, smooth deformations are those that do not close the energy gap. In other words, in a transition between two non-equivalent systems, the gap must close.

Just as the genus number of a closed surface is related to the integral of the Gaussian curvature over the entire surface, the QH state is also related to a topological invariant. The Chern number is a quantity closely related to the theory of fiber bundles [14] and is the topological invariant characterizing gapped systems. For all purposes, we can consider it in terms of the Berry phase. In this way, we define the Chern number n_m as

$$n_m = \frac{1}{2\pi} \int d^2\mathbf{k} \mathcal{F}_m, \tag{1.1}$$

where $\mathcal{F}_m = \nabla \times \mathcal{A}_m$, the so called Berry's flux, is integrated over the entire Brillouin zone and $\mathcal{A}_m = i \langle u_m | \nabla_k | u_m \rangle$ where $|u_m(\mathbf{k})\rangle$ is a function of the Bloch's wave of the occupied states. Performing a sum over all occupied states

$$n = \sum_{m=1}^{N} n_m, \tag{1.2}$$

we have the total Chern number, which takes integer values (since n_m in turn can only be an integer value) and is an invariant as soon as the energy gap between empty and occupied states is finitely held. In 1982, the seminal work of Thouless, Kohmoto, Nightingale, and den Nijs (TKNN)[13] showed that the conductance calculated with the Kubo formula is related to the Chern number in the following way

$$\sigma_{xy} = ne^2/h. \tag{1.3}$$

This relationship between the conductance σ_{xy} and the Chern number is the reason for the stability of the quantization of the quantum Hall effect. The QH effect opens the doors for a topological classification of the quantum phases of matter. Since the QH state is a phase without time-reversal symmetry, the discovery of the topological nature of this effect led to the question of whether it was possible to obtain a topological nontrivial phase that preserved time-reversal symmetry. The answer to this question led to the discovery of the so-called 2D topological insulators.

1.2 Two-dimensional topological insulators: the BHZ model

To trigger the quantum Hall effect, the system must break the time reversal symmetry. Normally, this is possible if an external magnetic field is applied. In the so-called topological insulators, instead of one chiral channel through which the current circulates, we have two chiral channels in which the current circulates in opposite directions, so that the time reversal symmetry is preserved. The first system proposed as a platform for this described phenomenon, now known as the *quantum spin Hall effect*, was the graphene sheet.

In 1988, Haldane proposed a spinless model in which the quantum Hall effect could take place without Landau levels. To achieve such a system, a periodic magnetic field should be assumed that would lead to a flux of zero per unit cell [15]. Including the spin degree of freedom and considering spin-orbit coupling, Kane and Mele proposed a model in which the magnetic field was not necessary [16]. Considering a generalization of the Haldane model for spin $\frac{1}{2}$ electrons, Kane and Mele's work not only introduces the quantum Hall effect, but also introduces a new topological invariant to classify it: the well-known Z_2 invariant [17].

Nevertheless, spin-orbit coupling in graphene proved to be too weak to form the quantum spin Hall state. The logical next step in the research was systems composed of heavy elements, for which spin-orbit coupling would be of greater importance. With this goal in mind, Bernevig, Hughes, and Zang (BHZ) presented the important work predicting the quantum spin Hall effect in HgTe/CdTe quantum wells in 2006 [1].

The bottom of the conduction band and the top of the valence band of CdTe have s-orbital symmetry and p-orbital symmetry, respectively. This arrangement is the most common among semiconductors and is therefore often referred to as the *usual* arrangement. On the other hand, HgTe has an *inverted* band structure where the s levels are energetically below the p levels, as we can see in Figure 1.1, taken from [1]. Bernevig *et al.* has shown that for quantum wells where the HgTe layer with a thickness of $d < d_c = 6.3$ nm is surrounded by two CdTe layers, the symmetry of the energy levels for bound states follows the usual order (as for CdTe), while for $d > d_c = 6.3$ nm the order acquires an inverse character (corresponding to the behavior of HgTe). According to Fu and Kane, and assuming an approximation where inversion symmetry is present, the parity change of the lower valence band state leads to a phase transition observed by the change of the Z_2 invariant [18].

Only one year after the publication of the BHZ model, the research group led by Prof. Laurens Molenkamp in Würzburg (Germany) studied electronic transport in samples of HgTe/CdTe. These experiments confirmed the HgTe/CdTe quantum wells as the first 2D topological insulators or quantum spin Hall insulators experimentally discovered [2]. The obtained results can be seen in the figure 1.2 from reference [2], where one can see the resistivity curves as a function of gate potential in different samples. The results for the samples III e IV show a conductance of $2e^2/h$. Since these samples have different widths, $w = 1$ and 0.5 μm, respectively, the results indicate edge-localized currents. In the figure, we also see results for a sample whose well thickness is less than the critical value (sample I) and another (sample II) that has a well thickness greater than the critical value but has scattering effects due to finite temperature (30 mK) and greater length compared to samples III and IV.

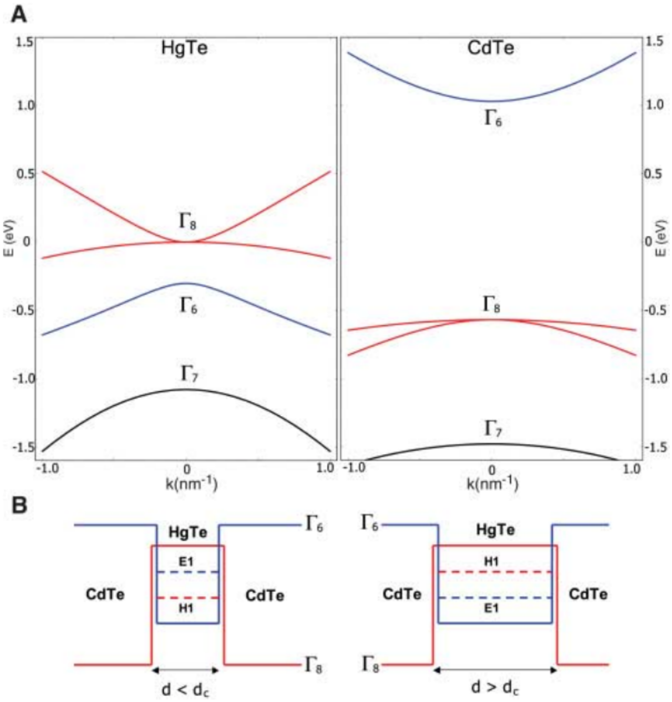

Figure 1.1: Figure from the reference [1]. **A** HgTe/CdTe bulk bandstructure near the Γ-point. **B** Ordering of the well subbands for thickness less than critical value (left) and greater than the critical value (right).

1.3 InAs/GaSb quantum wells

Although other systems had been proposed as potential candidates for 2D topological insulators [19, 20, 21, 22], only two systems could be experimentally realized. As mentioned above, HgTe/CdTe quantum wells were the first systems where the 2D topological insulator-like behavior was experimentally confirmed. However, the fabrication of samples with the required quality is not easy for most research groups. One of the main problems is the weak bonding between the atoms of Hg and Te, which makes the fabrication process extremely dangerous due to the toxicity of these compounds.

The second experimentally confirmed system as a quantum spin Hall insulator were the asymmetric quantum wells composed by InAs/GaSb with a *broken-gap* [3, 23]. Since it is a heterostructure of semiconductors III-IV, the growth process is much more accessible by molecular beam epitaxy (MBE). In addition, we also have a safer fabrication process because the bonding between the compounds is stronger than the HgTe/CdTe quantum well. Another difference between these two systems is that in the InAs/GaSb

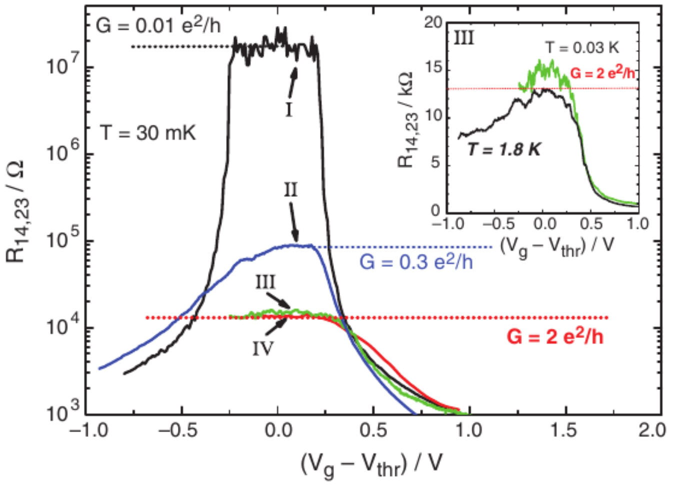

Figure 1.2: Figure from reference [2]. Experimental results for the resistivity of 4 samples of HgTe/CdTe. Sample I has thickness less than the critical value ($d = 5.5$ nm), being in this way in a trivial insulator state. Samples II-IV have thickness grater than the critical value ($d = 7.3$ nm). Sample II have dimensions $20 \times 13.3 \mu\text{m}^2$ while samples III and IV have 1×1 μm^2 and 0.5×1 μm^2 respectively. Inset: results the sample III in a linear scale for $T = 30$ mK (green) and for $T = 1.8$ K (black).

system, the electron subbands and the hole subbands are localized in different layers, as we can see in the figure 1.3 from reference [3].

One of the properties that make the asymmetric InAs/GaSb quantum well suitable for the study of topological phase transitions is the fact that, unlike HgTe/CdTe quantum wells, the inversion of the subbands can be controlled by applying an electric field perpendicular to the plane of the system sample. As mentioned in the previous section, this inversion occurs in HgTe/CdTe when the thickness of the middle layer (Hg) exceeds the critical value $d_c = 6.35$nm. In this way, we can think not only of a finely tunable experimental setup where the phase transition is controllable, but also of a new concept of transistors where the topological and trivial states could play the role of the ON and OFF states, respectively.

However, an important property of 2D topological insulators for application in electronics and spintronics is the size of the energy gap between bulk states. Apart from the advantages of using InAs/GaSb, the energy gap in this system is considerably smaller than that in the HgTe/CdTe quantum well [3]. Various ways to increase the energy gap in

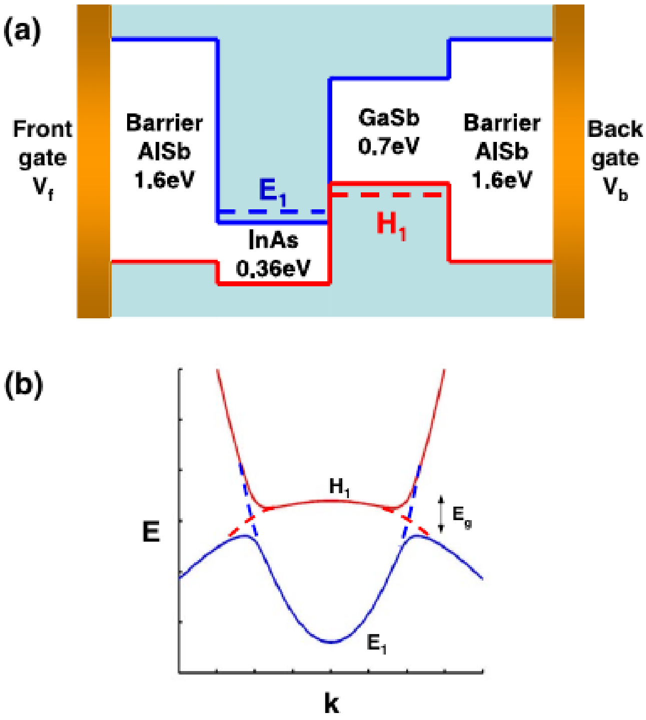

Figure 1.3: Figure from the reference [3]. **(a)** Conduction and valence bands limits of the quantum well constitute layers. Inset shows the inversion between the electron subbands ($\mathbf{E}_1$) and the hole subbands ($\mathbf{B}_1$) in different layers. **(b)** Hybridization gap opening after energy levels of different type (electron and hole) crossing.

InAs/GaSb quantum wells have been a recurring theme in recent work [23, 24] as well as in the study of symmetric heterostructures such as GaSb-InAs-GaSb and InAs-GaSb-InAs [25, 26].

In this work we will be concerned with the study of charge and spin transport in symmetric InAs/GaSb quantum wells. In particular, we will focus here on the system consisting of two GaSb layers forming a "sandwich" with an InAs layer in the middle, as shown in Figure 1.4. Therefore, as with the work described in [26], our main interest is to control the topological phase transition by applying an electric field in a direction perpendicular to the plane of the sample. It is important to emphasise that in this work, whenever we refer to an out-of-plane field, we are referring to a breaking of the structural symmetry in the growth direction of the quantum well, as shown in the pictorial representation in Figure 1.5.

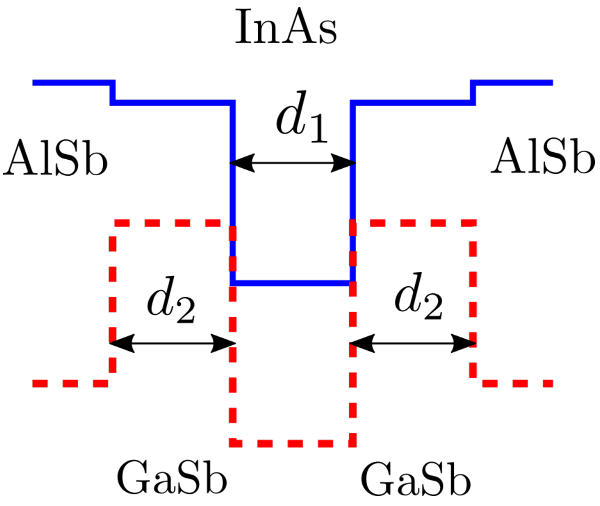

Figure 1.4: Pictorial representation for the limits of the conduction (blue) and valence (red) bands for the quantum well of InAs/GaSb.

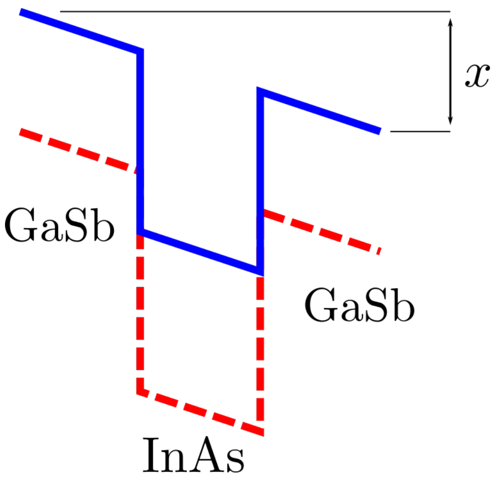

Figure 1.5: Representation of the limits of the bands when an electrical field is applied in the well's growth direction.

Chapter 2

Electronic transport calculations

Throughout this thesis, transport calculations were performed adopting the *Kwant* Python library [27]. This choice is based on the stability, the avaiability of a comprehensive documentation and its numerical performance.

The *Kwant* was designed to solve the scattering problem is infinite systems composed of a finite scattering region coupled to semi-infinite *leads*. To be treated by Kwant, the physical system has to be modeled in the language of tight-binding formulation, i.e.: the Hamiltonian of interest must be written as

$$\hat{\mathbf{H}} = \sum_{i,j} H_{ij} c_i^\dagger c_j \tag{2.1}$$

or, in the first quantization language

$$\hat{\mathbf{H}} = \sum_{i,j} H_{ij} \left| i \right\rangle \left\langle j \right| . \tag{2.2}$$

The developed model for this work as obtained through the discretization of the quantum operators, where, in particular, differential operators was written in terms of finite differences. In other words, the continuum space is replaced by a discrete grid where $|i\rangle$ represents the i-th site of this grid. From this Hamiltonian and from the geometry specification of the system, the Kwant-code uses the symmetries to generates from an infinite system, a finite graph representation where the nodes represent the discrete spatial sites and the links represent the hoppings (or couplings) between them. In the figure 2.1 we see such a graph representation. Notice that, being the relations amog the sites determined

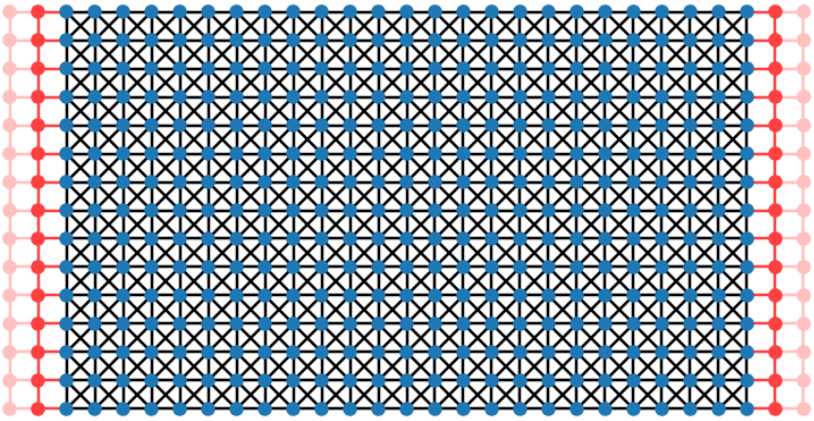

Figure 2.1: Graphical representation of a bidimesional system generated by Kwant. Red sites belong to the semi-infinite leads while blue sites describe the scattering region of the system.

by the Hamiltonian, it is possible to set different Hamiltonians for different parts of the system.

2.1 Scattering theory in nanostructures

The strategy adopted internally by Kwant is based on the method matching of the wavefunction of the different portions of the system. This formulation of the scattering problem is equivalent to that based on non-equilibrium Green's functions, which is assured by the Fisher-Lee relation [28].

Without losing generality, one can represent a system, defined by N *leads* connected to a scattering region, through the following Hamiltonian matrix

$$H = \begin{pmatrix} \ddots & V_L & & & \\ V_L^\dagger & H_L & V_L & & \\ & V_L^\dagger & H_L & V_{LS} & \\ & & V_{LS}^\dagger & H_S & \end{pmatrix}, \tag{2.3}$$

where all the N leads are grouped into a single “effective lead" whose unit cell Hamiltonian is denoted by H_L. The matrices V_L and $V_L^\dagger$ are *hopping* matrices that connect the leads unit cells. The scattering system Hamiltonian is given by the matrix H_S while the matrices V_{LS} and $V_{LS}^\dagger$ are hopping matrices that coupled the scattering system and the effective lead.

The infinite system's wavefunction, scattering system plus the effective lead, can be written as

$$\psi = \begin{pmatrix} \vdots \\ \psi^L(2) \\ \psi^L(1) \\ \psi^S \end{pmatrix}, \tag{2.4}$$

where ψ^S is the wavefunction in the scattering region and $\psi^L(i)$ is the wavefunction in the ith unit cell of the effective lead. Since we are considering the effective lead as infinite but translational symmetric, one can consider the solution for the Schrödinger equation given by

$$\mathcal{H}^L \left|\phi_n\right\rangle = E \left|\phi_n\right\rangle, \tag{2.5}$$

where

$$\mathcal{H} = \begin{pmatrix} \ddots & V_L & & \\ V_L^\dagger & H_L & V_L & \\ & V_L^\dagger & H_L & V_L \\ & & V_L^\dagger & \ddots \end{pmatrix}, \tag{2.6}$$

and

$$\left|\phi\right\rangle = \begin{pmatrix} \vdots \\ \phi(j-1) \\ \phi(j) \\ \phi(j+1) \\ \vdots \end{pmatrix}. \tag{2.7}$$

Using, as an ansatz, the eigenstate of the translation operator in the lead, $\phi_n(j) = (\lambda_n)^j \chi_n$, we arrive in a set of coupled equations that, after the division by the common factor, results in

$$\left(H_L + V_L \lambda_n^{-1} + V_L^\dagger \lambda_n\right) \chi_n = E \chi_n. \tag{2.8}$$

To $\phi(j)$ be bounded it is necessary that $|\lambda_n| \leq 1$. Thus, if $|\lambda_n| < 1$ we are going to have evanescent solutions while for $|\lambda_n| = 1$ one can write the translation eigenvalue in termos of the longitudinal momentum $\lambda_n = e^{ik_n}$, where the index, n designates a specific channel, which are also called *modes*. The normalization of these modes is given accordingly with the current expected value, in such a way that

$$\langle I \rangle \equiv 2 \operatorname{Im} \langle \phi_n(j) \left| V_L \right| \phi_n(j-1) \rangle = \pm 1. \tag{2.9}$$

Therefore, the modes can be classified as

- Incommig modes $\phi_n^{\text{in}} \to \langle I \rangle = +1$;
- Reflected and transmited modes $\phi_n^{\text{out}} \to \langle I \rangle = -1$; e
- Evanescent modes $\phi_n^{\text{ev}} \langle I \rangle = 0$.

With such a notation, one can denote the states inside the leads as

$$\psi_n(i) = \phi_n^{\text{in}}(i) + \sum_m S_{mn} \phi_m^{\text{out}}(i) + \sum_p \tilde{S}_{pn} \phi_p^{\text{ev}}(i), \tag{2.10}$$

being the wavefunction inside the scattering system denoted as

$$\psi_n(0) = \phi_n^S. \tag{2.11}$$

The crucial role of the Kwant library is to obtain the wavefunction ϕ_n^S and the scattering matrix S_{nm}. The calculation of such objects is realized upon the numerical matching of the wavefunctions at the leads with that in the scattering region. One of the most important quantities in the context of this work is the differential conductance, which is given by

$$G_{ab} = \frac{dI_a}{dV_b}, \tag{2.12}$$

where *a* and *b* identify the two electrodes connected to the system, and can be calculated by the Landauer equation

$$G_{ab} = \frac{e^2}{h} \sum_{n \in a, m \in b} |S_{nm}|^2 . \tag{2.13}$$

The local density of states and the current densities are also of great interest for this work, and can all be obtained through the knownledge of the wavefunction in the scattering region (ϕ_n^S).

2.2 BHZ model in Kwant

As a introduction to *Kwant* package and initial benchmark, we performed a couple of calculations with known results. One of such calculations was the electronic transport in 2D topological insulators. In particular, the model adopted was that described as the Bernevig-Hughes-Zhang model (BHZ) [1] for HgTe-CdTe quantum well. The system's effective Hamiltonian in this formulation is given by

$$H_{\pm} = (C - D\mathbf{k}^2)I_{2\times2} + (M - B\mathbf{k}^2)\sigma_z \pm A(k_x\sigma_x \mp k_y\sigma_y). \tag{2.14}$$

Where $\mathbf{k}^2 = k_x^2 + k_y^2$ is the absolute squared wavevector and σ_i (with $i = x,\ y$ and z) represent the corresponding Pauli's matrices. The parameters given by the capital letters (A, B, C, D and M) depend on the system's geometry, specifically they depend on the quantum well thickness. The adopted values are those presented in the Scharf *et al* [4], where, for a system presenting the quantum spin Hall (QSH) state are defined by: $A = 364.5$ meV nm, $B = -686.0$ meV nm^2, $D = -512.0$ meV nm^2, $M = -10.0$ meV.

It is almost trivial to get the band structure of the system using Kwant: for a system described by 2.14 with the shape of a strip with 200 nm of width. In the figure 2.2 we can see the characteristic result featuring the edge states with linear dispersion crossing what would be the energy gap in the *trivial* regime.

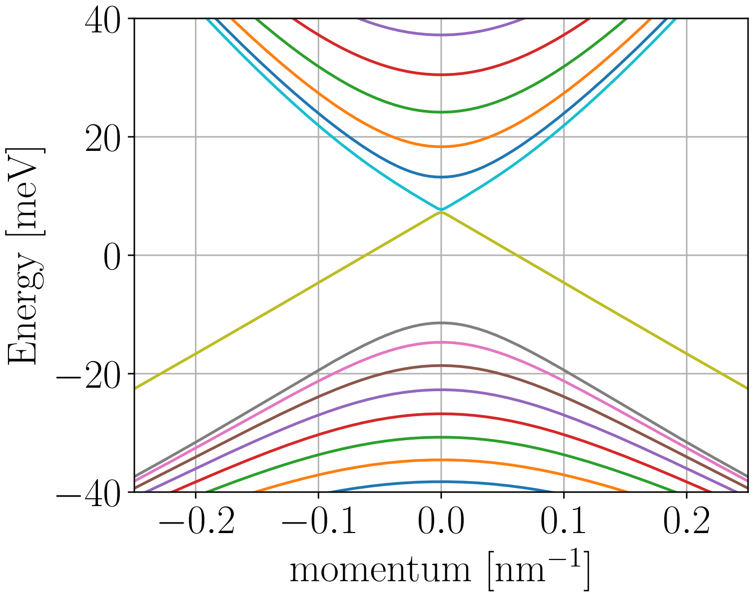

Figure 2.2: Band structure for a bidimesional strip with width of 200 nm and described by the BHZ model Hamiltonian [1, 4]. Although the horizontal axis is entitled as *momentum*, the values assumed here are those for the x-component of the wavevector: k_x.

The conductance between the sample contacts, or leads, is also easy to get with Kwant. The results presented in the figure 2.3 show us the conductance values separated by the spin component. We can see that, in this specific situation, the results for conductance are identical, which is not true in the presence of a magnetic field. Comparing with the results presented in [29], where the method adopted was based on recursive Green's functions, one can see an excelent agreement.

Yet as a benchmark, we introduced the effects of an out-of-plane magnetic field and compare the results with those from the literature. To consider the magnetic field we have to modify the Hamiltonian properly. Following the work of Sharf [4], we have

$$\hat{H}_{\uparrow(\downarrow)} = C + M\sigma_z - \frac{D + B\sigma_z}{\hbar}\left[\left(\hat{p}_x - \frac{\hbar y}{l_B^2}\right) + \hat{p}_y\right] \pm \frac{A}{\hbar\sigma_x}\left(\hat{p}_x - \frac{\hbar y}{l_B^2}\right) - \frac{A\sigma_y}{\hbar}\hat{p}_y \pm \frac{\mu_B \sigma_g}{2}, \tag{2.15}$$

where, besides the already known Pauli's matrices σ_i, we also have the matrix σ_g that is defined as

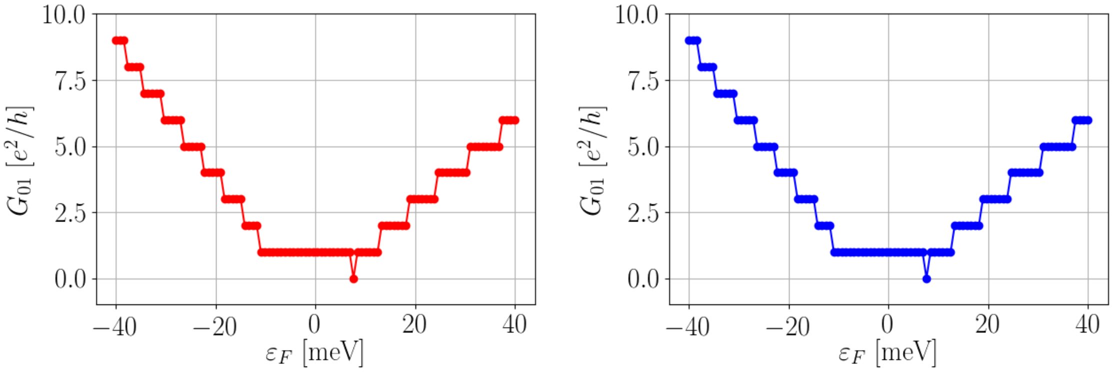

(a) Spin Up

(b) Spin Down

Figure 2.3: Conductance separated by spin projections.

$$\sigma_g = \begin{bmatrix} g_e & 0 \\ 0 & g_h \end{bmatrix}, \tag{2.16}$$

where g_e and g_h are the out-of-plane effective g-factors for the electron-type E and for the hole-type H bands respectively. Still in the equation 2.15,$l_B = \sqrt{\hbar/e|\mathbf{B}|}$ is defined as the magnetic length.

Diagonalizing the Hamiltonian (2.15) for $B = 0.1$ we have the band structure presented in the figure 2.4. From this result we can see a accordance, at least qualitatively speaking, with the results in [4]. By analysing what happens to the energy levels for $k_x = 0$ as a function of the magnetic field strength, we obtain the figure (2.4), which matches with the result presented in [4].

In order to evaluate the results for quantum transport, we simulate the same system studied in [29]. Specifically, we have simulated the transport through a system with a spatial dependent Fermi energy. In the first and the last third of the scattering region (near the right and left lead respectively) we keep the Fermi level in what is called the bulk region (away from the insulator gap or the where only the edge states appear). While the central part the Fermi level was kept over the edge states. The results are presented in the figures (2.5) e (2.6). Again, one notices agreement between the our results and those obtained via Green's function formalism.

However, it should be remembered that there are limitations in using Kwant, for ex-

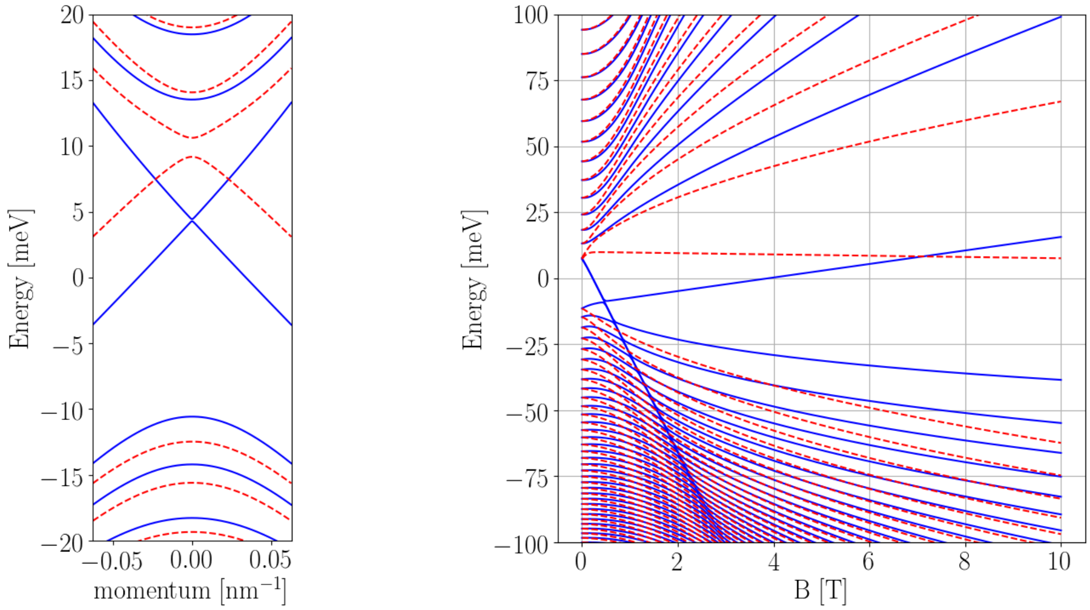

Figure 2.4: *Left:* Band structure for a quantum well with $d = 7$ nm of thickness and $w = 200$ nm of width submitted to an out-of-plane magnetic field of $B = 0.1$ T. (*Right:*) Energy levels for $k_x = 0$. For both (a and (b), solid and dashed lines represent spin-up and spin-down states respectively.

ample, it is impossible to include electron-electron interactions in the systems and there is no way to include potential difference between the leads without programing a great deal of code to get a potentially slow execution time. The great advantage is to have a excelent tool suitable to get fast an reliable results that otherwise would demand even more time to be implemented.

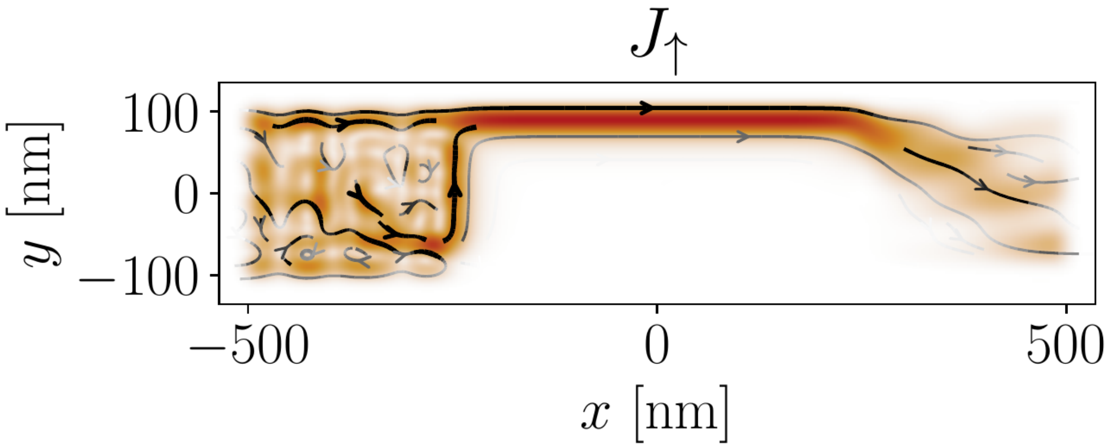

Figure 2.5: Local current density mapping for spin-up states.

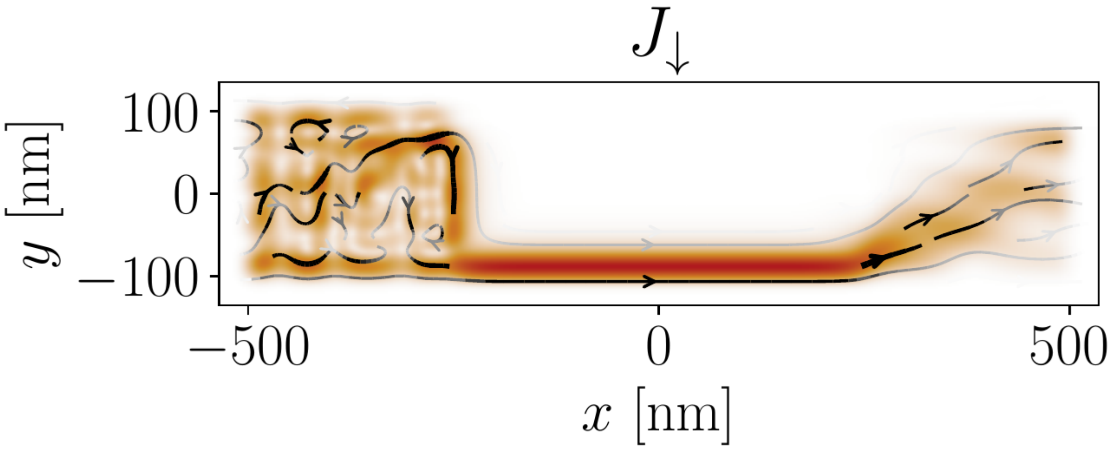

Figure 2.6: Local current density mapping for spin-down states.

Chapter 3

Edge state oscillations in InAs/GaSb quantum wells

Among the finds in the research for an alternative to HgTe/CdTe quantum wells as a platform for the spin quantum Hall effect, only one system among those proposed got experimental confirmation: the broken gap InAs/GaSb asymmetric quantum well [30]. What turns this system special is the fact that the bottom of the InAs conduction band is located bellow the top of the GaSb valence band [31]. Due to this characteristic energy bands allignment, the InAs conduction states hybridize with the valence states of the GaSb layer, allowing an energy gap inversion between the electron-like and the hole-like bands that are close in energy. The discution and the results presented in this chapter were published at Physical Review B 104, 195307 (2021) [32].

3.1 Introduction

It was predicted that broken-gap InAs/GaSb asymmetric quantum wells also behave as QSHI [3]. More importantly, 8-band $k \cdot p$ calculations have suggested that the topological transition (i.e., gap inversion) can be controlled by applying an external electric field along the growth direction [33] applied through a potential difference between front- and back-gates.

These theoretical predictions were then tested in a variety of experiments on InAs/GaSb quantum well samples. Evidence for a gap at charge neutrality [34] and quantized conductance [30, 35] were reported in small samples (with length $L \lesssim 2\mu$m).

More recently, the topological phase transition as a function of front and back-gate voltages was characterized [36, 37] such electric-field driven topological phase transitions was characterized in InAs/GaSb quantum wells [38, 39, 36, 37] and thin films of 3D topological insulators [40, 41].

In spite of these experimental developments, finding quantized conductance plateaus in these systems is a challenging task, as the actual conductance values can vary from sample to sample and in different experiments. For instance, the presence of helical sates at zero field in p-n junctions at zero magnetic field is inconclusive [42, 43]. More importantly, edge state transport has been detected in the *trivial* phase of InAs/GaSb/InAs quantum wells [44, 45]. Indeed, such states are seen in several samples and might be contributing to the conductance in the topological phase as well.

This telling example shows that it is not trivial to distinguish non-topological and topologically protected helical states from transport data alone. In a way, this is similar as in the case of Majorana zero modes in semiconductor nanowires where “quantized” values of the conductance can occur even in the absence of topologically-protected modes [46]. As such, it is desirable to have additional signatures of the presence of topologically-protected helical edge states in InAs/GaSb/InAs samples.

In this work, we address this question by studying a realistic model for InAs/GaSb/InAs quantum wells in the presence of an applied electric field and showing that the inter-edge coupling of edge states in narrow samples can lead to oscillations as a function of the field. Such oscillations occur only in the topological phase and can be directly linked to the presence of helical edge states and thereby, signal the onset of QSHI behavior. As such, the oscillations in the edge states can serve as a confirmation for the presence of topologically-protected helical edge modes in InAs/GaSb/InAs quantum well systems.

Moreover, we show that the electric field controls not only the topological transition but also increases the exponential localization of the edge states, similarly to the role played by the magnetic field in regular quantum Hall edge states. In this sense, the situation is analogous to the energy oscillations seen in other contexts such as Majorana systems [47, 48] and zeroth Landau level oscillations in nodal semimetals [49].

3.2 Model

We consider the asymmetric InAs/GaSb system depicted in Figure 3.1. In this geometry, the system is comprised by a single InAs quantum well in the conduction band (for electron-like states) next to a GaSb valence band quantum well (for hole-like states) leading to a band inversion at the InAs/GaSb interface. Similarly to the case of HgTe/CdTe [1] and InAs/GaSb single quantum wells [3, 33], a topological phase transition between a trivial insulator and quantum spin Hall phases can be controlled by varying the width d_1 of the InAs quantum well [26]. Throughout the investigation, we consider fixed widths d_1 and d_2 corresponding to the quantum spin Hall phase, namely $d_1 = 91$ Å (or 15 monolayers of InAs) and $d_2 = 48.8$ Å (8 monolayers of GaSb). As an additional consistency check, the calculations were performed for $d_1 = 97$ Å (16 monolayers of InAs), yielding similar results (see Table 3.1).

The low-energy BHZ Hamiltonian used in this work was obtained following a four-step process, which we now summarize. First, the GaSb/InSb/AlSb system is modeled with an 8-band Kane Hamiltonian properly parametrized. Next, a low-energy effective Hamiltonian is determined with a “folding-down" procedure and, from both the low-energy and the original 8-band Hamiltonians, the effect of the applied electric field in the system is introduced. Finally, the low-energy Hamiltonian is reviewed and parametrized in order to account the effects of the applied electric field. We discuss these steps in detail in the following sections.

3.2.1 $\mathbf{k} \cdot \mathbf{p}$ Hamiltonian

We start from a well-known eight-band Kane Hamiltonian [50], parametrized for the InAs, GaSb and AlSb bulk alloys. For the modeling of the heterostructure, the confinement of the quantum well in the growth (z) direction is included by considering the envelope function approximation (EFA), where the Kane model parameters are taken as z-dependent and the substitution $k_z \to -i\partial_z$ is made. We used a reciprocal space approach where the envelope function is solved by expanding the growth direction into the Fourier coefficients of the potential and z-dependent parameters [51, 52]. To describe each layer, we used realistic Kane model parameters depicted in Ref. [53].

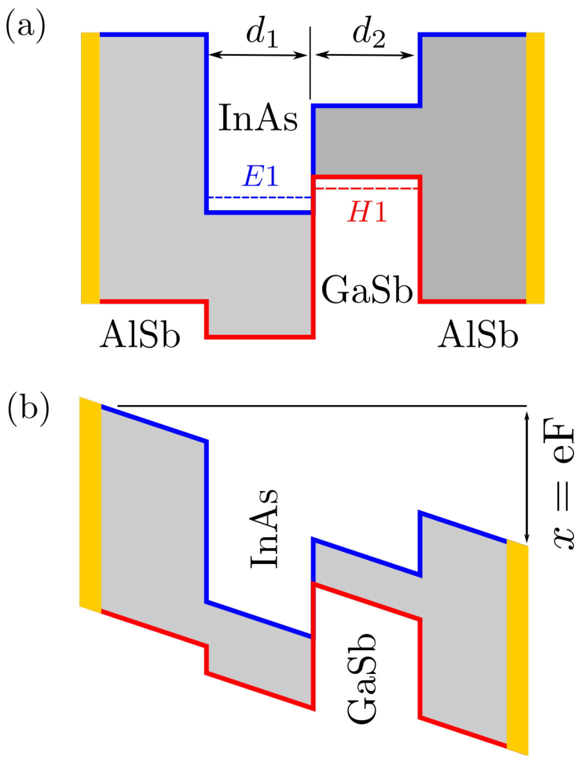

Figure 3.1: Schematic representation of the asymmetric InAs/GaSb quantum well. (a) Representation of "inverted" regime, with the hole-like state in the GaSb quantum well (width d_2) at a higher energy than the electron-like state at the InAs quantum well (width d_1). (b) Representation of the Stark shift eF referred henceforth simply as "electric field". The inverted regime can be obtained also by varying eF.

Due to the confinement in the z-direction, one can assume that the band structure along that direction is flat and that the eigenfunction of the states at Γ are a good description of all the functions along the Γ-Z direction.

Fig. 3.2 presents the system band profiles, wave functions and band structures. Panel (a) shows the band profiles for conduction and valence band. The box indicates the energy range around Fermi level inspected in this analysis. Panels (b), (c) and (d) present the density probabilities of the first conduction band, heavy and light hole states, respectively. The band structure associated with these lowest states in the [100]-direction is depicted in panel (e), and panel (f) details the 4 states that may be inverted under the application of the electric field along the growth direction in the region defined by the box in panel (e). The goal of our modeling is to define a realistic simplified Hamiltonian that reproduces the band structure presented on the last panel.

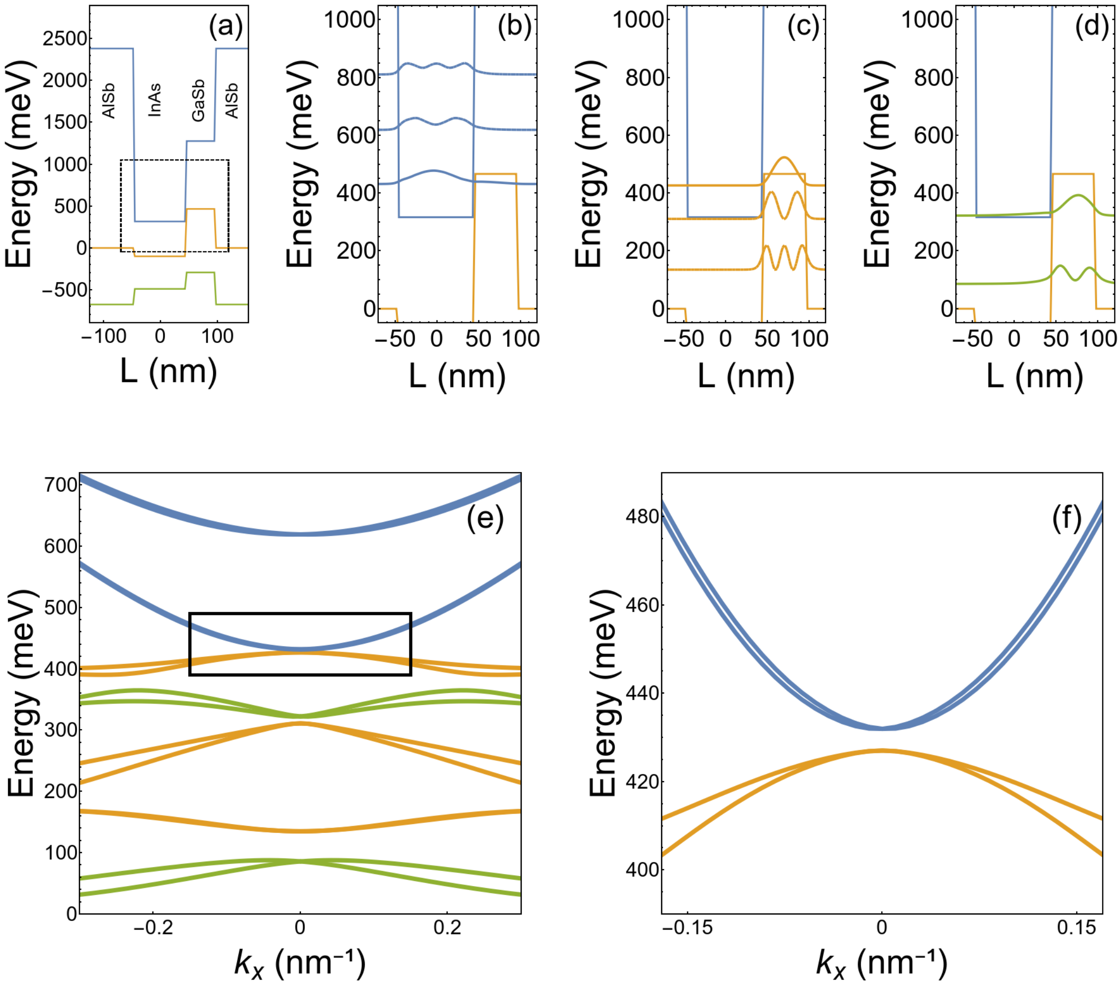

Figure 3.2: Results from the $\mathbf{k} \cdot \mathbf{p}$ calculations. In (a) we show the schematic view of the layered system used in the 8×8 k.p calculation. The dashed box in panel shows the energy range of the states around the Fermi energy that is used in panels (b), (c) and (d) that show the less energetic conduction band, heavy and light hole states, respectively. Panel e) presents in the same energy range the full 8×8 calculation along the parallel direction. The box in this panel presents the target band structure used to obtain the four-band effective model, shown in (f). Heavy hole, light hole and electron states are represented in green, yellow and blue respectively.

3.2.2 Projected perturbation method

After solving for the eigenenergies at the Γ point in momentum space ($k_x = k_y = 0$),

$$\mathcal{H}^0 |\varphi_n\rangle = E_n |\varphi_n\rangle \ , \tag{3.1}$$

we have selected the eigenstates $|\varphi\rangle$ most affected by the inversion of bands, i.e., where the mixing of conduction bands and valence bands would be more important. The influence of the states that does not belong to this set can be shown to be small in first order by the Löwdin [54] perturbation theory.

Therefore the full analytical 8×8 Kane Hamiltonian expanded into plane waves in the z-direction is projected over those selected states at the Γ-point, resulting in an effective 2D-Hamiltonian

$$H = (\langle\varphi_1| , \cdots , \langle\varphi_{16}|)\mathcal{H}(\mathbf{k}) \begin{pmatrix} |\varphi_1\rangle \\ \vdots \\ |\varphi_{16}\rangle \end{pmatrix} , \tag{3.2}$$

where we have taken eight doubly degenerate bands due to spin degeneracy presented in Figs. 3.2(b), (c) and (d).

The chosen 16 states are the ones most affected by the band inversion, where the mixing of CB and VB is important. Using the Löwdin perturbation scheme [54] to validate this set, we chose the set of states mostly affected by the inversion as our unperturbed set in which the first order corrections are small. Finally, the band structure of the 16-state Hamiltonian seemingly compares to the one found with the much more expensive envelope function $8\,\text{NPW} \times 8\,\text{NPW}$ Kane Hamiltonian, where NPW is the number of plane waves of the expansion.

3.2.3 Effective low-energy Hamiltonian

Coming back to the Löwdin perturbation scheme, since we have a Hamiltonian that fully describes our problem, we can still reduce it by defining a new set of unperturbed functions. We chose them as the functions in the small box in Fig. 3.2 e) and apply the first order correction using the other twelve states in a numeric folding down procedure by using the Schur's complement [55]. The final result is a 4×4 Hamiltonian matrix with the format

$$H = \begin{bmatrix} H_+(\mathbf{k}) & H_\pm(\mathbf{k}) \\ H_\mp(\mathbf{k}) & H_-(\mathbf{k}) \end{bmatrix}, \tag{3.3}$$

where the matrix H_+ is defined as

$$H_+(\mathbf{k}) = \begin{bmatrix} \varepsilon_c(\mathbf{k}) & iP\mathbf{k}_+ \\ -iP\mathbf{k}_- & \varepsilon_v(\mathbf{k}) \end{bmatrix}, \tag{3.4}$$

with

$$\varepsilon_c(\mathbf{k}) = E_c + \alpha_c\mathbf{k} + \gamma_c\mathbf{k}^2 \tag{3.5}$$

$$\varepsilon_v(\mathbf{k}) = E_v + \alpha_v\mathbf{k} + \gamma_v\mathbf{k}^2 \tag{3.6}$$

and the time-reversal symmetry guaranteeing that $H_-(\mathbf{k}) = H_+^*(-\mathbf{k})$. The coupling matrices $H_\pm(\mathbf{k})$ and $H_\mp(\mathbf{k})$ are given by

$$H_\pm(\mathbf{k}) = \begin{bmatrix} 0 & N_-(\mathbf{k}) \\ N_+^*(\mathbf{k}) & 0 \end{bmatrix}, \tag{3.7}$$

noticing that $H_\mp = (H_\pm)^\dagger$ due to the unitarity. The non-zero elements of coupling matrices are given by

$$N_\pm(\mathbf{k}) = -(k_x^2 - k_y^2)\eta_2 \pm k_x k_y \eta_3. \tag{3.8}$$

A closer inspection of the η_2 and η_3 values shows that the folded down off-diagonal terms in the $N_\pm$ blocks are responsible for corrections of the order of 0.01 meV in the region of the fitting ($|k_x| < 0.15$ nm^{-1}), having little or no impact at the band structures when compared to the case where we consider the bottom of conduction and top of the valence band states in the full Kane calculation. As such, the diagonal approximation ($\eta_2 = \eta_3 = 0$) turns out to give an excellent description of the low-energy physics around the Γ point.

3.2.4 Four-band BHZ model

Following these results, we opted for using a BHZ-like Hamiltonian [1] given by

$$H_{\mathrm{BHZ}} = \begin{bmatrix} \hat{H}_{2\times2}(\mathbf{k}) & 0 \\ 0 & \hat{H}_{2\times2}^*(-\mathbf{k}) \end{bmatrix}, \tag{3.9}$$

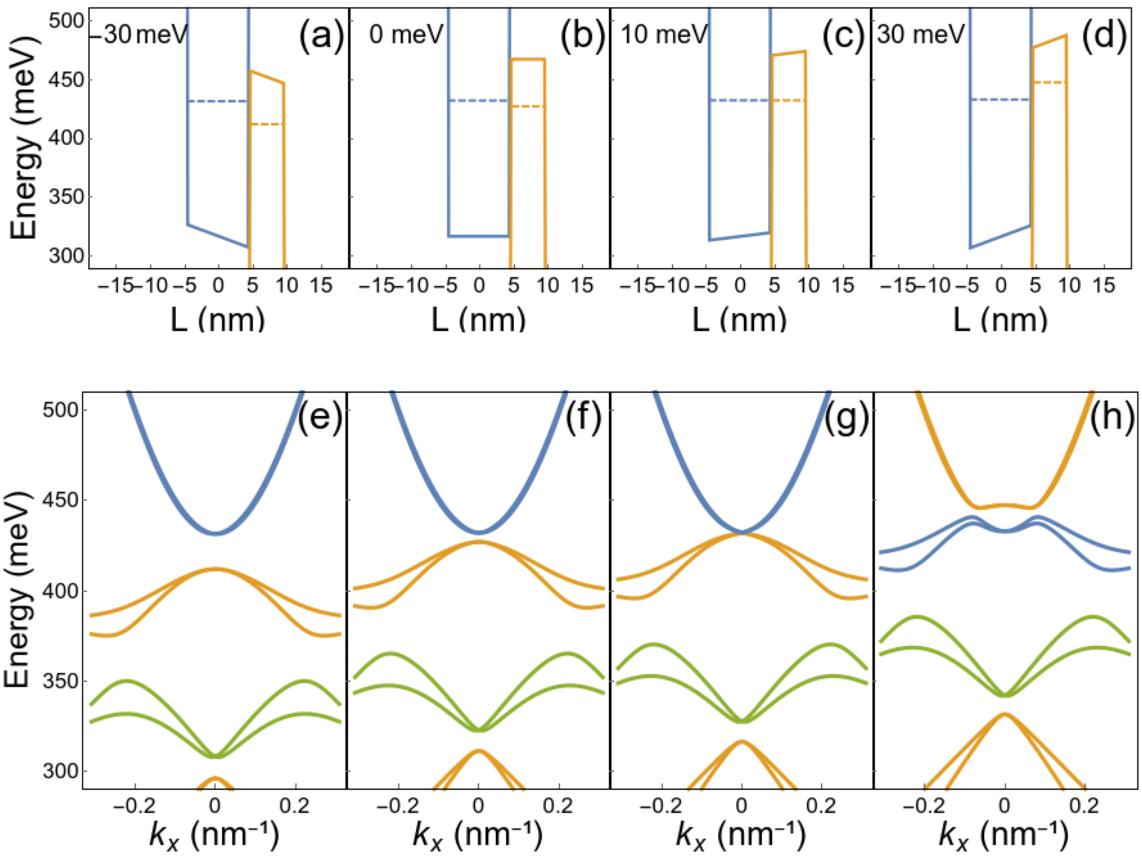

Figure 3.3: Panels (a), (b), (c) and (d) show the Schematic view of the confinement profiles including the heterostructure profile and the applied electric field creating a Stark shift between the interfaces with the AlSb layers on both sides of -30, 0, 10 and 30 meV, respectively. The bottom of the conduction band (blue, on the left) and the top of the valence band (orange, on the right) as well as the highest valence band and lowest conduction band states are shown. (e), (f), (g) and (h) panels show the band structures with the different applied fields.

with

$$\hat{H}_{2\times 2}(\mathbf{k}) = \begin{bmatrix} \varepsilon_c(\mathbf{k}) & iP\mathbf{k}_+ \\ -iP\mathbf{k}_- & \varepsilon_v\mathbf{k} \end{bmatrix} , \tag{3.10}$$

with $\varepsilon_c(\mathbf{k})$ and $\varepsilon_v(\mathbf{k})$ defined in Eqs. (3.5) and (3.6). The basis set is defined in the usual order [1] as

$$|E,+\rangle\,,\ \ |H,+\rangle\,,\ \ |E,-\rangle\,,\ \ |H,-\rangle\ \ , \tag{3.11}$$

defined by the character of the states of the Kane model at Γ-point heavy holes for $|H,\pm\rangle$ and a composition of conduction band electrons (mostly), light (smaller) and split-off holes (negligible) for $|E,\pm\rangle$.

3.2.5 Applied Electric field

The effect of applied electric field's potential drop across the z-directions is shown in Figure 3.3, both in the potential profile and in the Kane model band structures. A positive drop causes the inversion of conduction and heavy hole bands and a negative one increases the gap.

Figs. 3.3 (a)–(d) show the potential profiles, together with the Γ-point energies, across the topological phase transition. As the energy difference between HH and EL states become smaller [Figs. 3.3 (a),(b)], the gap closes [Figs. 3.3 (c)] and reopens [Figs. 3.3 (d)] with an inverted gap. The respective band structures show usual semiconductor behavior [Figs. 3.3(e) and (f)], a gap closure [Fig. 3.3(g)] and a “gapped semimetal" [Fig. 3.3(h)].

In the next step we proceeded to the fitting of the BHZ model, with different electric field profiles, in the range from -30 to 70 meV. The fittings of selected systems are presented on Figure 3.4. From the fittings, one may conclude that the BHZ Hamiltonian provides all the features necessary to the analysis of these four states under the application of an electric field.

As a final step to parameterize our system, we proceed to the fitting of the curves of the relevant parameters under the influence of the applied electric field. The dependence of

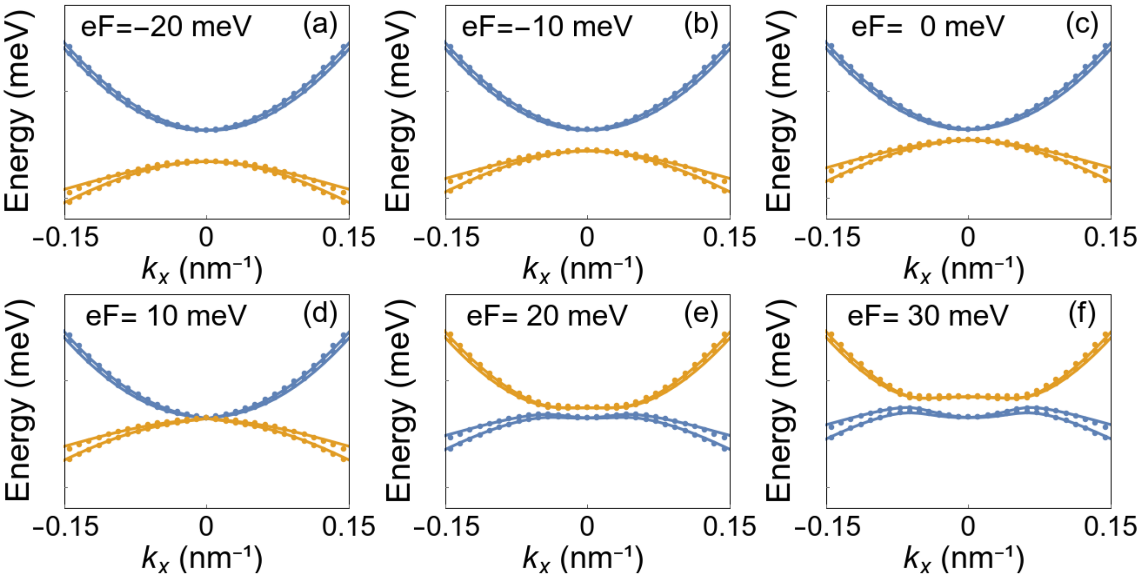

Figure 3.4: Band structures of the BHZ (dotted lines) and 8×8 k.p (solid lines) models under the influence of eF. From a) to f), eF = -20, -10, 0, 10, 20 and 30 meV, respectively. Yellow (blue) bands have hole-like (electron-like) character at Γ-point.

the parameters in Eq. (3.9) on the electric field eF is given by the following expressions:

$$\begin{aligned} E_{(c,v)}(eF) &= A_{(c,v)}.eF + B_{(c,v)} \\ \gamma_{(c,v)}(eF) &= C_{(c,v)}.eF + D_{(c,v)} \\ \alpha_{(c,v)}(eF) &= F_{(c,v)}.eF + G_{(c,v)} \\ P(eF) &= p_0 + p_1.eF \end{aligned} \tag{3.12}$$

with the fittings are presented in fig. 3.5. Each of these parameters depend on the quantum well thickness, as show in Table 3.1. Notice that the linear coefficients $\alpha_{c,v}$ are essentially two orders of magnitude smaller than the other relevant terms in the range $0 \leq eF \lesssim 60$ meV. As such, the linear terms of type $\alpha_{c,v}\mathbf{k}$ can be safely neglected near the Γ-point for all field values considered.

	$d_1 = 91$ Å	$d_1 = 97$ Å
A_c	1.613×10^{-6}	9.000×10^{-5}
A_v	3.729×10^{-5}	3.644×10^{-5}
B_c	3.177×10^{-2}	3.109×10^{-2}
B_v	3.140×10^{-2}	3.136×10^{-2}
C_c	-5.007×10^{-2}	-5.379×10^{-2}
C_v	3.480×10^{-2}	5.680×10^{-2}
D_c	4.691×10^{1}	4.625×10^{1}
D_v	-2.105×10^{1}	-1.778×10^{1}
F_c	1.952×10^{-1}	1.318×10^{-1}
F_v	3.068×10^{-1}	4.260×10^{-1}
G_c	-5.545×10^{-4}	-5.419×10^{-4}
G_v	9.703×10^{-4}	8.421×10^{-4}
p_0	8.436×10^{-2}	7.429×10^{-2}
p_1	-3.727×10^{-4}	-3.863×10^{-4}

Table 3.1: BHZ Hamiltonian parameters extracted from the fittings of Figs. 3.4 and 3.5. Energies are expressed in eV, lengths in Åand electric field in V.

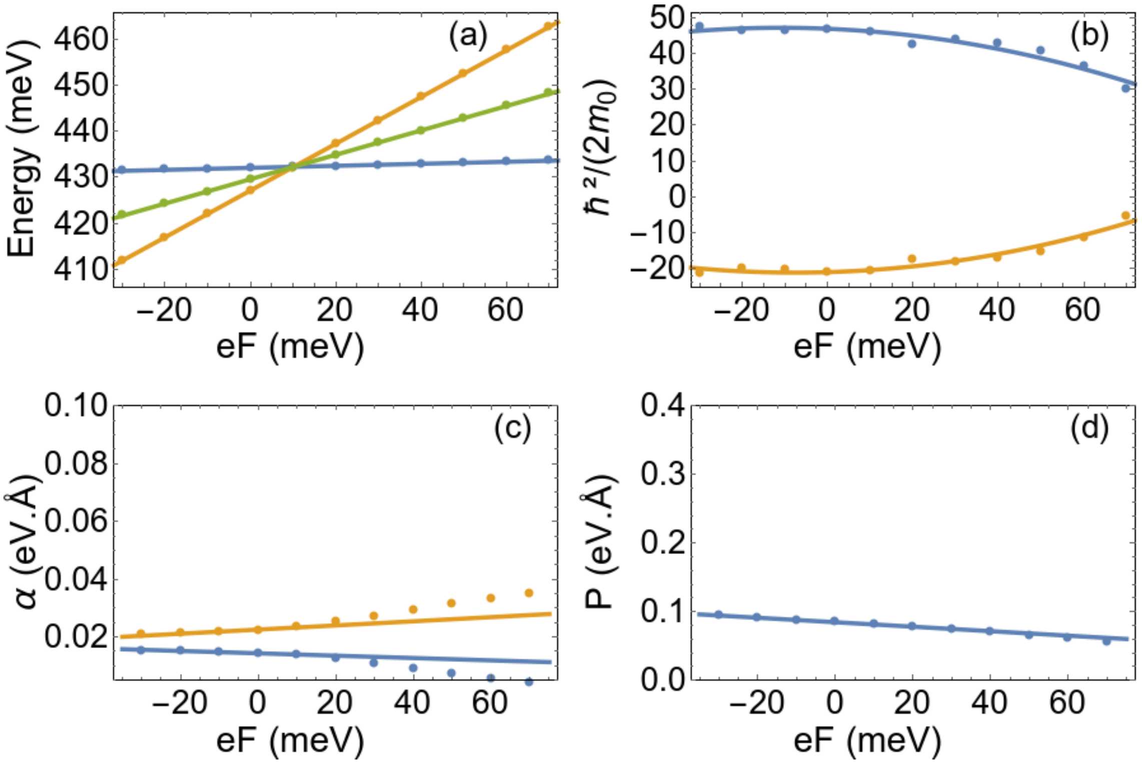

Figure 3.5: Fitting of the variation of BHZ relevant parameters under influence of eF. In solid lines the fitted curves and in dots, the original 8×8 Hamiltonian fitted values. a) valence band maximum (orange), conduction band minimum (blue) and Fermi level (green); b) effective mass parameter for valence (orange) and conduction (blue) bands; c) α parameter for valence (orange) and conduction (blue) bands; and d) interband interaction parameter P.

3.3 Results and conclusions

3.4 Topological edge states

Once the parametrization of the low-energy BHZ Hamiltonian has been established, we turn to the topological transition and the edge states. To this end, we work with real-space discretization of the $\hat{H}_{2\times2}$ block written as:

$$\hat{H}'_{2\times2} = \begin{bmatrix} \varepsilon'_c(\mathbf{k}) & iP\mathbf{k}_+ \\ -iP\mathbf{k}_- & \varepsilon'_v\mathbf{k} \end{bmatrix} \tag{3.13}$$

where the primed diagonal elements are given in terms of the parametric functions defined in Eq. (3.12) (and $\alpha_c = \alpha_v = 0$ as previously justified) by

$$\varepsilon'_{(c,v)}(\mathbf{k}) = E_{(c,v)} + \gamma_{(c,v)}\mathbf{k}^2 \,, \tag{3.14}$$

with the parameters set for the case of $d_1 = 91$ Å(InAs quantum well width) shown in Table 3.1.

In the following, we consider infinite strips with translational symmetry in x-direction and hard-wall boundary conditions in y-direction with width L_y. For concreteness, we focus on narrow ($L_y = 100$ nm) and wide ($L_y = 200$ nm) systems The calculations are performed with the Kwant package [27].

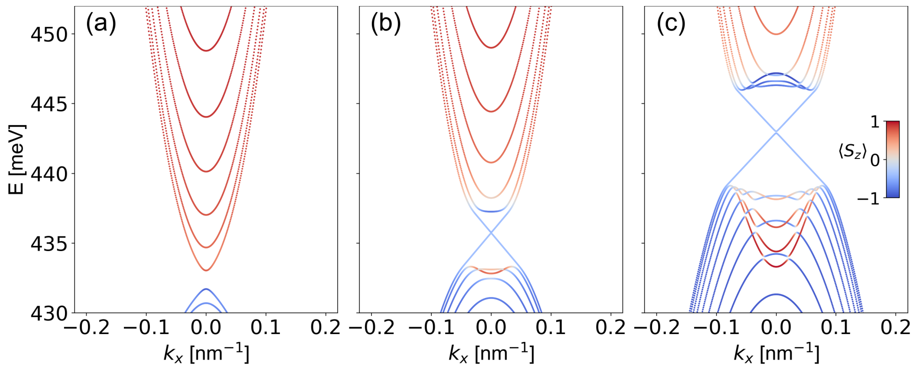

Figure 3.6: Electric field-driven topological phase transition for the InAs/GaSb double quantum well with $d_1 = 91$ Å and $d_2 = 48.8$ Å. BHZ energy spectra for $eF =$ (a) 10 meV, (b) 20 meV, and (c) 40 meV. The color bar corresponds to the pseudospin projection. Band inversion and topologically protected edge states are shown in panels (b) and (c).

3.4.1 Electric-field driven topological transition

We begin by characterizing the topological phase transition as a function of the Stark shift energy eF [33]. Figure 3.6 shows results for spectrum of the discretized Hamiltonian for different values of eF for wide strips ($L_y = 200$ nm).

The topological transition at $eF \approx 12$ meV is marked by the closing of the gap and subsequent band inversion, along with the appearance of edge states with linear dispersion (seen in Fig. 3.6-b and 3.6-c). The band inversion can be quantified by the z-component of the “pseudospin”, defined by $\langle S_z\rangle = \int(|\psi_e|^2 - |\psi_h|^2)$. As such, the color of each state indicates its composition of the states in terms of $|E,+\rangle$ and $|H,+\rangle$ components.

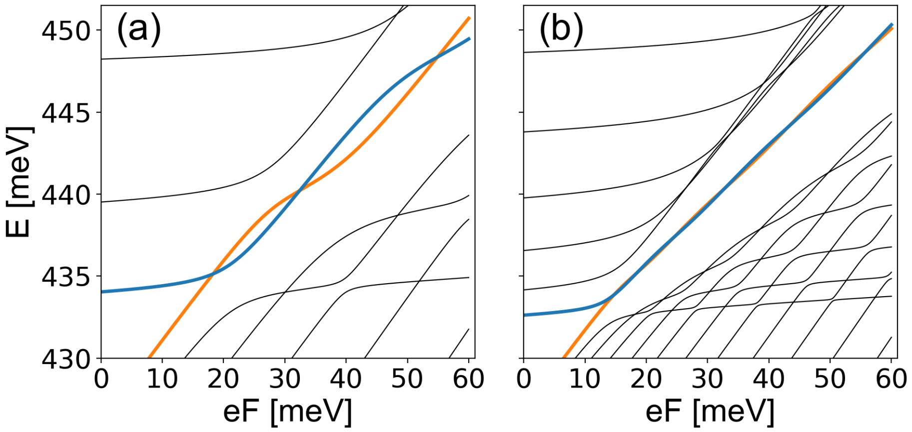

Figure 3.7: Energy spectra for at $k_x = 0$ versus the electric field for quantum well widths of $L_y =$ (a) 100 nm. and (b) 200 nm. Lines in blue and orange represent the low-lying states, which become the edge states after the transition. Note the oscillations arising from inter-edge coupling for narrow quantum wells.

3.4.2 Edge state energy oscillations

Next, we turn to the behavior of the edge states in the topological phase as the Stark shift is increased. Figure 3.7 shows the spectrum at $k_x = 0$ as a function of eF for two different values of L_y: (a) 100 nm (narrow strip) and (b) 200 nm (wide strip).

The electric-field induced topological phase transition is clearly seen in both cases, marked by a crossing of the states at the top of the conduction band and at the top of the valence band. These *low-lying energy states* become the sub-gap edge states in the topological phase.

More importantly, Fig. 3.7 shows a clear oscillatory pattern in the energy of the edge states as a function of eF. These oscillations are more pronounced in the case of narrow strips (Fig. 3.7-a).

The origin of such electric-field-driven oscillations, as it will become clear later, is the inter-edge coupling of the edge states localized at opposite edges.In a sense, these are equivalent to the magnetic field-driven oscillations appearing in short topological nanowires due to the coupling of Majorana zero modes at its ends [47, 48]As such, these low-lying oscillations occur only in the topological phase and can be regarded as true signatures of the presence of topological edge modes.

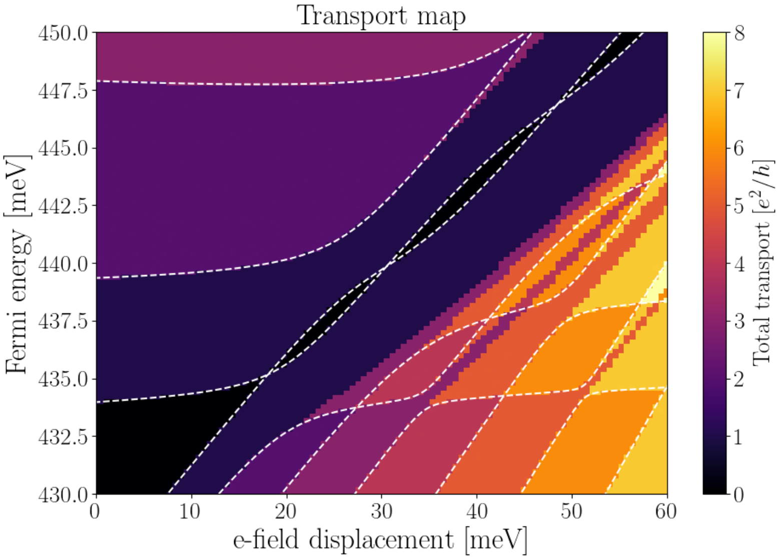

Figure 3.8: Transport mapped on the levels t kx = 0.

3.4.3 Edge state localization

The formal connection between the electric-field-driven edge state oscillations discussed above and those appearing in Majorana systems

In order to better understand how the coupling between edge states gives rise to oscillations as a function of magnetic field can be further explored in order to get a better understanding of the behavior of the edge states as the electric field increases. As such, inspired by Ref. [47] , we propose an ansatz of an oscillatory function with an exponential decay for the the electric field, we consider the following ansatz for the $k_x = 0$ edge state wave-functions as a function of the vertical coordinate y [47]

$$|\psi_{b(t)}(y)|^2 \propto e^{-\frac{2\tilde{y}_{b(t)}}{\xi}} \sin^2[k_f \tilde{y}_{b(t)}], \tag{3.15}$$

where which corresponds to an oscillatory function with an exponential decay where both the localization length ξ and the wave number k_f both depend on the electric field (see full expressions in section 3.5).

Figure 3.9 shows the evolution of $|\psi(y)|^2$ as a function of the electric field (eF) for $L_y = 100$ nm (Fig. 3.9-a) and 200 nm (Fig. 3.9-b). In both cases, it becomes clear that the low-lying states tend to localize at the edges. In the narrow strip (Fig. 3.9-a), the overlap between states at different edges leads to a stronger modulation as a function of the electric field.

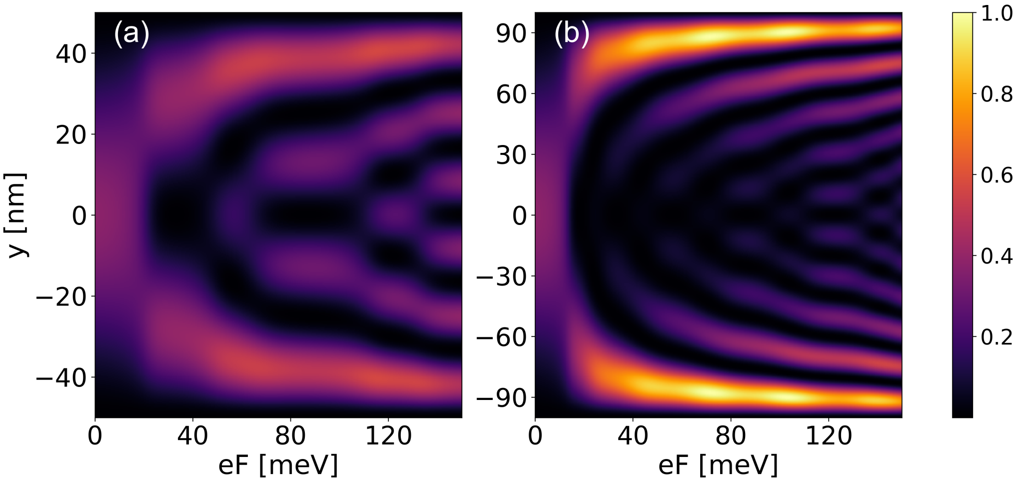

Figure 3.9: Electrically enhancement of the edge state localization for (a) $L_y = 100$ nm and (b) $L_y = 200$ nm. The color map indicates the transverse profile of the absolute squared value of the wave functions. In both panels, the wave functions adopted are those associated to the states represented by the blue line in the figure 3.6.

The localization length $\xi(eF)$ can be extracted by fitting an exponential through the first two local maxima of $|\psi(y)|^2$ (a linear fit in a semi-log plot). Similarly, the wave number $k_f(eF)$ can be extracted by averaging the distances between subsequent minima of $|\psi(y)|^2$.

In both cases, we can compare these fittings with analytical results (Eqs. (3.20) and (3.19) in section 3.5) obtained using the ansatz of by Eq. (3.15). The results shown in Figure 3.10 show an excellent agreement, further corroborating the choice of the ansatz. We note that,as shown in section 3.5, the exponentially localized form of Eq. (3.15) is derived for topologically protected states with energies at the center of the gap (“zero modes"). As such, non-topological states with a finite energy will *not*, in general, display these same features.

3.5 Analytical solution for the edge wave-function and hybridization energy

In this section, we derive the anaylical expressions for the edge state wave function $\psi(y)$ and energy, as well as the localization length $\xi(eF)$ and the wave number $k_f(eF)$ (which are functions of the Stark shift eF) appearing in Section 3.4.3. We note that a similar derivation for $\psi(y)$ can be found in Ref. [56].

First, in order to derive an analytic expression for the wave-function wave function and energy, we first define the energy of the $k_x = 0$ edge states for a infinitely wide strip, i.e. $E_\infty(eF) = \lim_{L_y\to\infty} E_{\text{edge}}(k_x = 0)$. This can be obtained as an order-3 polynomial approximation from numerical calculations. For a wide strip, the edge state wavefunction $\psi(y)$ will obey $H_{2x2}\psi(y) = E_\infty(eF)\psi(y)$, which can be written as

$$\begin{bmatrix} E_c - \gamma_c\partial_y^2 - E_\infty & iP\partial_y \\ iP\partial_y & E_v - \gamma_v\partial_y^2 - E_\infty \end{bmatrix} \psi(y) = 0 \ . \tag{3.16}$$

Since these states are exponentially localized at the edges, we can expand the edge mode in the form $\psi(y) \sim e^{\pm zy}$ with $z = ik_f - 1/\xi$ with ξ being the localization length. The solution of z must satisfy the quartic equation:

$$\det \begin{bmatrix} E_c - \gamma_c z^2 - E_\infty & iPz \\ iPz & E_v - \gamma_v z^2 - E_\infty \end{bmatrix} = 0 \ . \tag{3.17}$$

For $\xi > 0$, there are only two solutions for z:

$$z_\pm = -\sqrt{\frac{\Omega \pm \sqrt{\Lambda - \Omega^2}}{2\gamma_c\gamma_v}} \tag{3.18}$$

where $\Omega = -P^2 + (E_c - E_\infty)\gamma_v + (E_v - E_\infty)\gamma_c$ and $\Lambda = 4\gamma_c\gamma_v(E_c - E_\infty)(E_v - E_\infty)$. Both $k_f = \text{Im}[z]$ and $1/\xi = \text{Re}[z]$ can be rewritten in terms of Ω and Λ:

$$k_f = \frac{1}{2}\sqrt{\frac{\sqrt{\Lambda} + \Omega}{\gamma_c\gamma_v}} \ , \tag{3.19}$$

$$\xi = -\frac{4\gamma_c\gamma_v k_f}{\sqrt{\Lambda - \Omega^2}} \ . \tag{3.20}$$

We can classify the two solutions as wave functions ψ_t and ψ_b localized at the top ($y = L_y$) and bottom ($y = 0$) edges respectively. We can write, say, $\psi_b(y)$ as:

$$\psi_b(y) = ue^{zy} \begin{bmatrix} A_0 \\ B_0 \end{bmatrix} + ve^{z^* y} \begin{bmatrix} A_1 \\ B_1 \end{bmatrix} \ . \tag{3.21}$$

By imposing time-reversal symmetry and the boundary condition $\psi_b(y=0)=0$, it is clear that $u=-v=i$ and $A(B)_0=A(B)_1$. Thus, a solution of Eq. (3.16) assuming Eq. (3.17) is given by:

$$A_{0(1)}=\frac{(E_v-z^2\gamma_v-E_\infty)}{Pz}, B_{0(1)}=I \ . \tag{3.22}$$

Taking all of this into account, $\psi_b(y)$ is given by:

$$\psi_b(y)\propto e^{-y/\xi}\sin(k_f y) \ , \tag{3.23}$$

and $\psi_t(y)$ (localized at the top edge) will be given by

$$\psi_t(y)\propto e^{-(L_y-y)/\xi}\sin(k_f(L_y-y)) \ . \tag{3.24}$$

Finally, the energy difference associated with inter-edge coupling of the modes can be calculated by taking

$$\Delta E=\frac{\langle\psi_t|H|\psi_b\rangle}{\langle\psi_{edge}|\psi_{edge}\rangle} \tag{3.25}$$

where $|\psi_{edge}\rangle=a_0\,|\psi_t\rangle+a_1\,|\psi_b\rangle$ with the constant $|a_0|^2+|a_1|^2=1$ and $\langle\psi_{edge}|\psi_{edge}\rangle=\kappa$ is the normalization factor. In the limit of large system, $L_y\gg\xi$, the normalization can be approximated as

$$\kappa\approx\frac{k_f^3\xi^3}{4(k_f+k_f^3\xi^2)} \tag{3.26}$$

and the energy becomes

$$\Delta E\approx\frac{k_f L}{2\xi\kappa}e^{-L/\xi}\left(\frac{|A_0|^2}{|A_0|^2+1}\gamma_c+\gamma_v\right)\sin(k_f L) \ . \tag{3.27}$$

For the parameters of Table 3.1, this means that ΔE oscillates with the electric field as

$$\Delta E\approx\frac{2k_f L}{\xi^2}e^{-L/\xi}\left(\gamma_c+\gamma_v\right)\sin(k_f L) \ , \tag{3.28}$$

with k_f given by Eq. (3.19).

This derivation is analogous to that of [47] for Majorana bound states in topological nanowires. This underscores the fact that there is a formal connection between the electric-field-driven edge state oscillations discussed in the main text and those appearing in Majorana systems as a function of magnetic field. In fact, this analogy can be in principle applied to other topological systems [49] in order to get a better understanding the oscillatory behavior of edge state energies as a function of external parameters.

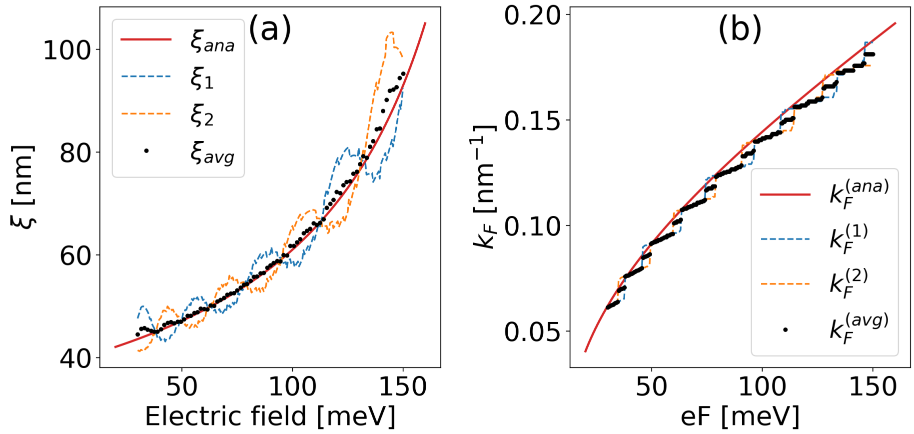

Figure 3.10: Evolution of the localization length ξ (a) and the wave number k_f (b) for the low-lying energy states for a system with $L_y = 200$ nm. In dashed lines we have the values obtained from numerical fitting over the wave functions, while the dotted values are the average of the results for both states and the continuum line is the analytical result.

Chapter 4

From edge to bulk transport in GaSb/InAs/GaSb quantum wells

4.1 System and effective Hamiltonian definition

As mentioned in the introduction chapter on topological insulators, the InAs/GaSb quantum wells are more accessible than those made of HgTe/CdTe. This is because InAs/GaSb quantum wells have brought the attention for decades due to their technological applicability [57, 58] and for the possibility that this system has to present semimetallic behavior [59, 60], turning, in this way, the fabrication process of such systems known worldwide by the scientific community.

Beyond the samples fabrication issue, InAs/GaSb symmetric quantum wells have been winning space in the research for 2D topological insulators that present a large energy gap between the bulk states. For some specific *strain* conditions, it is possible to reach an energy gap of the order of 60 meV [25], which is comparable to the value achieved for HgTe/CdTe quantum wells [1] with the advantage of being insensitive to temperature.

In this chapter, we are interested in the transport properties of *strips* formed perpendicularly to the quantum well growth direction of GaSb/InAs. We are also interested in the conditions to improve control of such properties, for example, by applying an electric field in the growth direction, which would act as a gate. In the figure (4.1), we present a representative draw of the system's profile in which we are interested.

It is necessary to consider spin-orbit effects to describe the system more realistically.

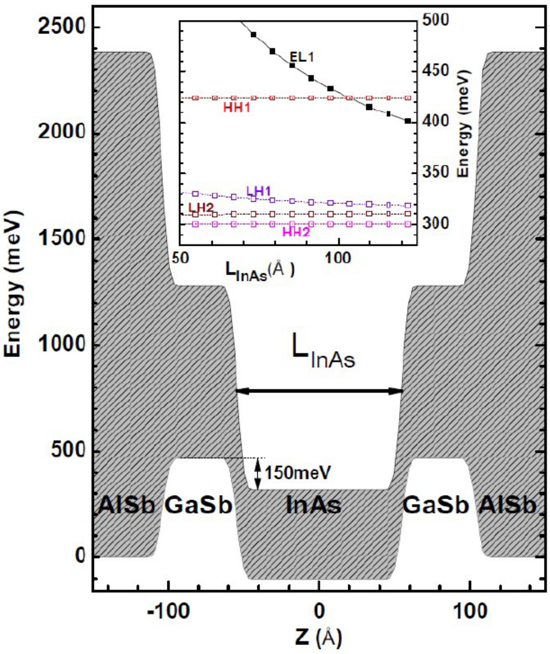

Figure 4.1: Model for an InAs/GaSb triple quantum well. In the inset plot, one can see the energy levels ordering for both electron-like and ($EL1$) and heavy hole-like ($HH1$) where it can be seen the band inversion for $L_{InAs} > 103.7$ Å. Source [5].

In this way, the electron wavefunctions $\psi(\boldsymbol{r})$ at the bulk of these materials must be solutions of the Schrödinger equation given by:

$$\left[\frac{p^2}{2m_0} + V(\boldsymbol{r}) + \frac{\hbar}{4m_0^2c^2}(\boldsymbol{\sigma} \times \nabla V) \cdot \boldsymbol{p}\right] \psi(\boldsymbol{r}) = \varepsilon\psi(\boldsymbol{r}). \tag{4.1}$$

Since we are dealing with a system that is symmetric by translations of unit vectors of the crystal lattice, Bloch's theorem applies. Thus, one can write the equation for the periodic part of the Bloch wave functions as

$$\begin{aligned} &\left\{\frac{p^2}{2m_0} + V(r) + \frac{\hbar}{4m_0^2c^2}(\boldsymbol{\sigma} \times \nabla V) \cdot \boldsymbol{p} + \right. \\ &\left. \frac{\hbar^2k^2}{2m_0} + \frac{\hbar\mathbf{k}}{m_0}\left(\boldsymbol{p} + \frac{\hbar}{4m_0c^2}\boldsymbol{\sigma} \times \nabla V\right)\right\} u_{nk} = \varepsilon_{nk}u_{nk}. \end{aligned} \tag{4.2}$$

Similar to what was done in chapter 3, we adopted the 8-band Kane model for the $\mathbf{k} \cdot \mathbf{p}$ method with Luttinger corrections for the effective masses. Given the symmetry of the crystal represented by its point group, it is possible to arrive at basis functions defined for the Γ-point such functions describe the energy states corresponding to the top of the valence band and the bottom of the conduction band. These states are usually denoted $|S, \uparrow (\downarrow)\rangle$, $|X, \uparrow (\downarrow)\rangle$, $|Y, \uparrow (\downarrow)\rangle$ and $|Z, \uparrow (\downarrow)\rangle$, and their corresponding wave functions transform accordingly to the atomic orbitals *s, x, y* and *z* when subjected to group symmetry transformations point of the zinc-blende structure.

However, once one has considered the spin-orbit coupling, the spin projection is no longer a good quantum number. In such situations, the usual procedure is to change the Hamiltonian representation adopting a basis in which the matrix where the spin-orbit coupling is diagonal. In that spirit, expressing the conduction band, we have

$$|\Gamma_6, \pm 1/2\rangle = |S \uparrow (\downarrow)\rangle$$

while for the valence bands we have

$$\begin{aligned}
|\Gamma_8, \pm 1/2\rangle &= \sqrt{\frac{2}{3}}\, |Z \uparrow (\downarrow)\rangle \mp \frac{1}{\sqrt{6}}\, |(X \pm iY) \downarrow (\uparrow)\rangle\,, \\
|\Gamma_8, \pm 3/2\rangle &= \mp \frac{1}{\sqrt{2}}\, |(X \pm iY) \uparrow (\downarrow)\rangle \text{ and} \\
|\Gamma_7, \pm 1/2\rangle &= \mp \frac{1}{\sqrt{3}}\, |Z \uparrow (\downarrow)\rangle - \frac{1}{\sqrt{3}}\, |(X \pm iY) \downarrow (\uparrow)\rangle\,,
\end{aligned}$$

where we have the *heavy-hole*, *ligght-hole* and the *split-off* states respectively.

With such a model, one can describe the band structures for the bulk of each of the materials. Usually by applying perturbative methods in the vicinity of high symmetric points, the Γ point, for example. To describe the heterostructure formed by the symmetric quantum well, the envelope function approximation [61] was adopted, in which the confinement in the z-direction results in the substitution $k_z \to -i\partial_z$. This procedure leads to a system of coupled equations that one can solve numerically by applying a plane-wave expansion using [26] Fourier transforms.

In addition, we adopted the Löwdin method (quasi-degenerate perturbation theory) to derive the effective Hamiltonian. In this way, the effect of the outermost subbands could be considered [62, 63]. Initially, without the application of an external electric field, we considered a model composed of 3 bands with parameters obtained from a *fitting* of the $\mathbf{k} \cdot \mathbf{p}$ described above. Such an adjustment of the parameters was performed by Sipahi et. al. [5]. Without an external electric field, it was possible to unify the description for different thicknesses of the quantum well (central layer of InAs) in a single Hamiltonian with a distinct set of parameters for each case:

$$H = \begin{bmatrix} \varepsilon_E + \gamma_E(k_x^2 + k_y^2) & 0 & -iP\,(k_x - ik_y) \\ 0 & \varepsilon_{H_S} + \gamma_{H_S}(k_x^2 + k_y^2) & -i\Delta_R \\ +iP\,(k_x - ik_y) & +i\Delta_R & \varepsilon_{H_A} + \gamma_{H_A}(k_x^2 + k_y^2) \end{bmatrix}. \tag{4.3}$$

The matrix presented in the equation (4.3) is written in the basis $\{|E\rangle\,,\ |H_1\rangle\,,\ |H_2\rangle\}$ where the three states that make up the basis are given by an 'electron-like' state $|E\rangle$ and two states formed by symmetrical (H_S) and anti-symmetrical (H_A) combinations of hole-like states located in the GaSb layers.

The parameters vary according to the thickness of the layers that make up the quantum well. Here we will only be interested in the dependence on the thickness of the central layer of InAs. The table presented below shows the parameters obtained for the three thicknesses studied.

	97 Å	103 Å	110 Å	Units
ε_C	0.032	0.031	0.031	(Ry)
ε_V	0.031	0.031	0.031	(Ry)
γ_C	36.927	39.907	42.946	(Ry a_0^2)
γ_V	-22.478	-21.674	-15.416	(Ry a_0^2)
η_2	-0.280	-0.296	0.310	(Ry a_0^2)
η_3	-1.161	-1.174	1.189	(Ry a_0^2)
P	-0.109	0.097	0.087	(Ry a_0)

The Δ_R parameter is defined by the value of the electric field in the growth direction of the quantum well. Such parameter has a paramount importance since, among our goals, is to find a way to control the system topology through an electric field that will act as a *gate*. The formulation of the Hamiltonian given by (4.3) presents an approximation for the electric field, while a more accurate formulation was left for the following sections.

Rewriting the Hamiltonian (4.3) discretizing the y-dimension and limiting the system to consider a two-dimensional strip, we arrive at the band structures that can be seen in the plots in the figures (4.2), (4.3) and (4.4). We can see that the smaller the thickness of the quantum wells, the greater the range of electric field values for which we have a trivial insulator. The three thicknesses studied show such behavior with the notable difference that the 110 Å system presents a kind of Dirac cone “buried" in the hole-like bands, as can be seen in the leftmost panel of the figure (4.4).

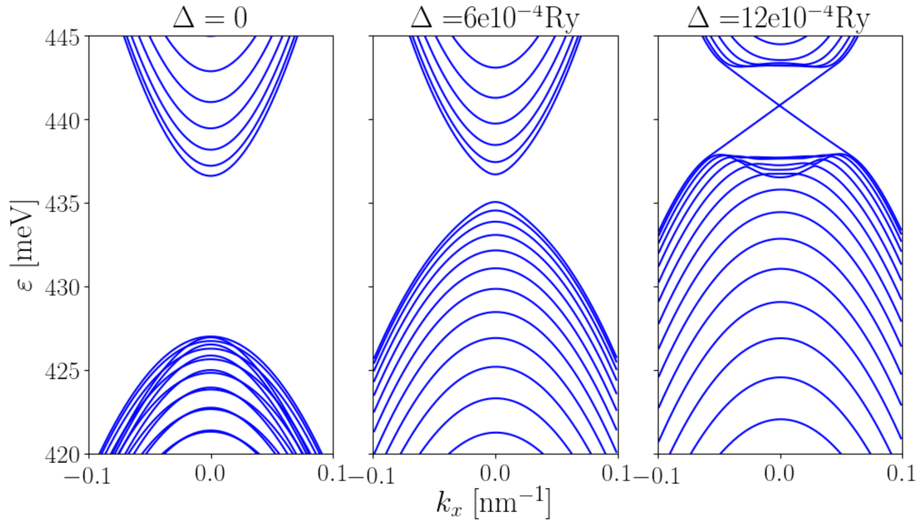

Figure 4.2: Band structure for a 300 nm wide and 97 Å thick strip format system. Each of the three plots shows the band structure for a different value of applied electric field (values of Δ in the Hamiltonian given by Eq. (4.3).

4.2 The effect of the electric field on the Hamiltonian

To approximate the behavior to the situation where we have an electric field perpendicular to the plane of the quantum well, some modifications in the Hamiltonian led to a new formulation. In this alternative expression, we use a description in which the states of different spin projections, designated by the plus (+) and minus (-) signs, are coupled in such a way that the Hamiltonian matrix is given by

$$H = \begin{bmatrix} H_{11}(k_x, k_y) & H_{12} \\ H_{12}^* & H_{11}^*(-k_x, -k_y) \end{bmatrix}, \tag{4.4}$$

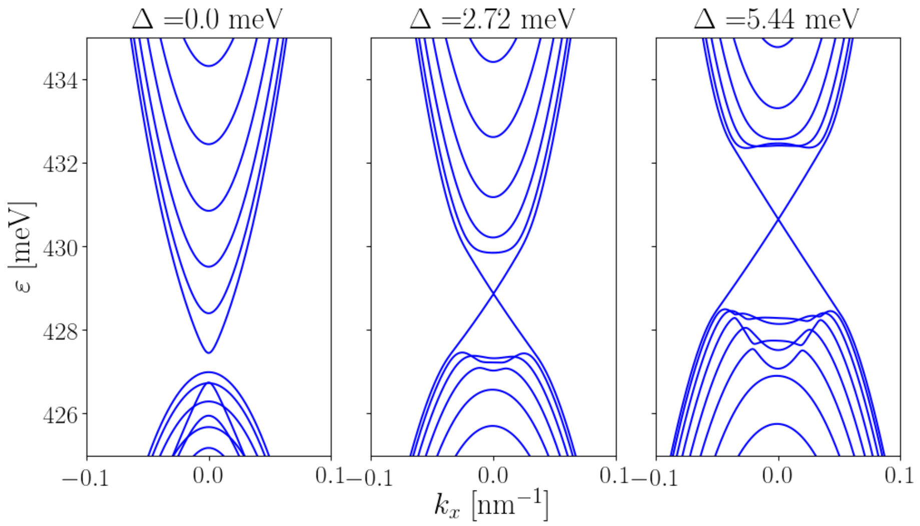

Figure 4.3: Band structure for a 300 nm wide and 103 Å thick strip format system. We see again the evolution of the band structure with the increase of the applied electric field (values of Δ in the Hamiltonian given by Eq. (4.3).

where H_{11} and H_{12} are given by

$$H_{11}(k_x, k_y) = \begin{bmatrix} \varepsilon_C + \gamma_C(k_x^2 + k_y^2) & iP(k_x - ik_y) & -(k_x^2 - k_y^2)\eta_2 - ik_xk_y\eta_3 \\ -iP(k_x + ik_y) & \varepsilon_V + \gamma_V(k_x^2 + k_y^2) & 0 \\ -(k_x^2 - k_y^2)\eta_2 + ik_xk_y\eta_3 & 0 & \varepsilon_V + \gamma_V(k_x^2 + k_y^2) \end{bmatrix}, \tag{4.5}$$

and for

$$H_{12} = \begin{bmatrix} 0 & 0 & 0 \\ 0 & 0 & i\Delta \\ 0 & i\Delta & 0 \end{bmatrix}. \tag{4.6}$$

This matrix representation for the Hamiltonian follows the basis given by

$$\{|E_1+\rangle, |H_1+\rangle, |H_2-\rangle, |E_1-\rangle, |H_1-\rangle, |H_2+\rangle\}. \tag{4.7}$$

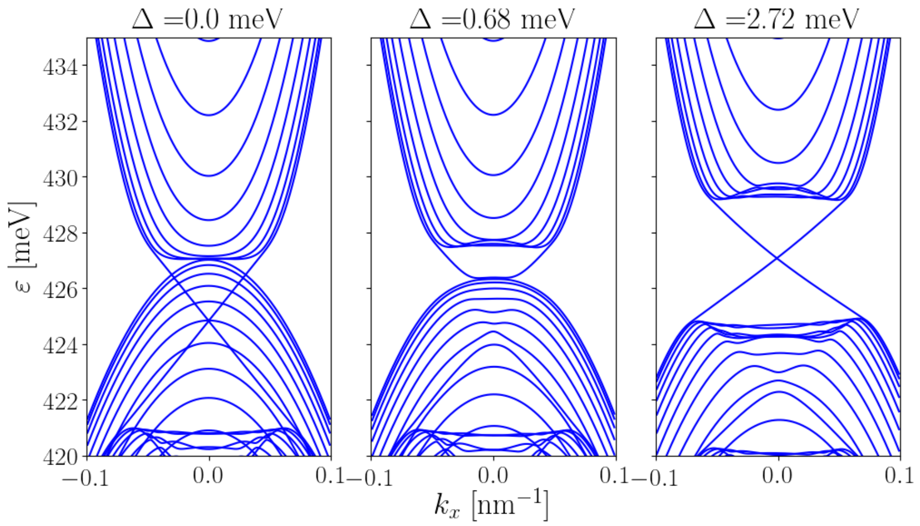

Figure 4.4: Band structure for a 300 nm wide and 110 Å thick strip format system. As in the graphs of the figures (4.2) and (4.3) we see the formation of edge states with linear dispersion with the difference that in this case we have the formation of what appears to be a Dirac cone ‘ ‘*buried*" in hole-type bulk states.

4.3 Electric field dependence of the parameters

In what follows we will talk a lot about dependence on the *electric field*, however, it is necessary to clarify what exactly we mean by this term. Whenever we refer to an electric field applied in the direction perpendicular to the plane of the quantum well, we are referring to the difference between the backgrounds of the conduction bands of the outer layers of the quantum well. energy represented by the “*x*" in the figure 4.5.

Until then, we were treating the parameters of the Hamiltonian, except for Δ, as independent of the electric field. However, this is an approximation of the behavior of these parameters. An update of the definition of the Hamiltonian matrix is necessary to consider such dependence accordingly.

Such definition for the Hamiltonian operator proved to be structurally dependent on the system’s thickness (97 Å, 103 Å, or 110 Å). In other words, until now, it has not been possible to find a closed-form for the Hamiltonian in which the size of the quantum well reflects only on the parameters’ values. Furthermore, for systems with thicknesses of 103 Å and 110 Å, it was only possible to find approximate forms that do not hold quantitatively for all energies of the first Brillouin zone. However, by analyzing these

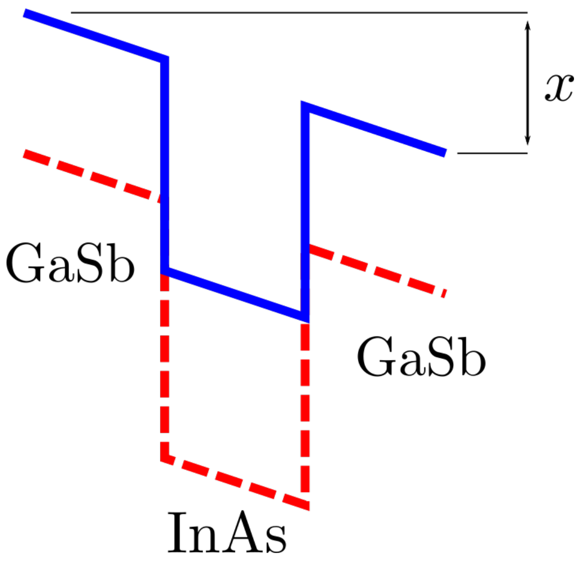

Figure 4.5: Representation of the limits of the conduction (blue) and valence (red) bands when there is an electric field applied in the direction of growth of the well.

mentioned Hamiltonians, it is possible to obtain a qualitative view of such systems.

4.3.1 System with thickness of 97 Å

So let's start with the 97 Å thick system. For this system, a closed-form was obtained for the entire first Brillouin zone. Thus, in this case, we have that the Hamiltonian is given by

$$H = \begin{bmatrix} H_+(\mathbf{k}) & H_{+-}(\mathbf{k}) \\ H_{-+}(\mathbf{k}) & H_-(\mathbf{k}) \end{bmatrix}, \tag{4.8}$$

where the matrix H_+ is given by the expression (4.9), while $H_-(\mathbf{k}) = H_+^*(-\mathbf{k})$.

$$H_+(\mathbf{k}) = \begin{bmatrix} \varepsilon_C(\mathbf{k}) & iPk_- & 0 \\ -iPk_+ & \varepsilon_V(\mathbf{k}) & 0 \\ 0 & 0 & \varepsilon_{VB}(\mathbf{k}) \end{bmatrix}. \tag{4.9}$$

The coupling matrix that gives the interaction between the Hamiltonian diagonal blocks is given by

$$H_{+-}(\mathbf{k}) = \begin{bmatrix} 0 & 0 & N_-(\mathbf{k}) \\ 0 & 0 & 0 \\ N_+^*(\mathbf{k}) & 0 & 0 \end{bmatrix}, \tag{4.10}$$

and $H_{-+} = (H_{+-})^\dagger$.

The functions that are dependent on $\mathbf{k}$, which appear in both the definition of H_+ and the definition of H_{+-} are defined as follows,

$$\begin{aligned}
\varepsilon_C(\mathbf{k}) &= E_C + \gamma_C(k_x^2 + k_y^2) + \alpha_C k_\parallel, \\
\varepsilon_V(\mathbf{k}) &= E_V + \Delta E + (\gamma_C + \Delta\gamma)(k_x^2 + k_y^2) + \alpha_V k_\parallel, \\
\varepsilon_{VB}(\mathbf{k}) &= E_{VB} - \Delta E + (\gamma_V - \Delta\gamma)(k_x^2 + k_y^2) + \alpha_V k_\parallel, \\
N_\pm(\mathbf{k}) &= \pm\eta_2(k_x^2 - k_y^2) - i\eta_3 k_x k_y,
\end{aligned}$$

where $k_\parallel = k_x + k_y$, and the parameters given by $\Delta\gamma$ and $\alpha_{C(V)}$ are functions of the magnitude of the electric field

$$\begin{aligned}
\Delta\gamma(x) &= A_1 + B_1 \exp(C_1 x), \\
\Delta E(x) &= A_2 x, \\
\alpha_C(x) &= A_3 + B_3 x, \text{ and} \\
\alpha_V(x) &= A_4 + B_4 \exp(C_4 x),
\end{aligned}$$

with x representing the magnitude of the electric field in the growth direction of the well. The values adopted for the parameters in the simulations presented in the following section are given in the tables 4.1 and 4.2.

Table 4.1: Parameters for 97 Å

Parameter	Value	Units
E_C	.032088	Ry
E_{VB}	.0314028	Ry
γ_C	40.7246	Ry a_0^2
γ_V	-19.8633	Ry a_0^2
P_x	-.0766887	Ry a_0
η_2	-.19853	Ry a_0^2
η_2	-.0317535	Ry a_0^2

Table 4.2: Parameters for the Δ and α functions

Parameter	Value
A_1	-.231075
B_1	4.11407
C_1	-.255277
A_2	2.79538E-5
A_3	3.24001E-5
B_3	8.28089E-5
A_4	.0219519
B_4	-.02344
C_4	-.286293

4.4 Results and discussion

Translating the Hamiltonian described in the previous section to a tight-binding formulation, where the following substitution is made $k_\alpha \to -i\partial_\alpha$ where $\alpha = x,\ y$. Then, for the partial derivatives, one can translate them in terms of finite differences. In such a way, we can arrive at an appropriate model to serve as input for KWANT. In this way, it was possible to calculate the band structure, map the local currents over the system and calculate the total conductance in the linear response regime.

One of the main differences between the results obtained with the Hamiltonian from the previous section and the new one with parameters dependent on the electric field is the appearance of two non-degenerate Dirac cones in the gap between the bulk states. In the figure 4.6 we see the band structure for a system subjected to an electric field of 50 meV, in which, in the panels *(a)* and *(b)*, we see the bands obtained by diagonalizing the subblocks separately. In these calculations, we disregarded the values of the couplings between the pseudo-spins. In the *(c)* panel, we see very few differences between the cases with and without coupling between pseudo-spins.

We see in the graphs in the figure (4.7) some of the interesting results obtained with KWANT. In this first calculation, we adopted the Hamiltonian for a 97 Å thick system and simulated a tape with translational symmetry in the x-direction. The dimensions adopted

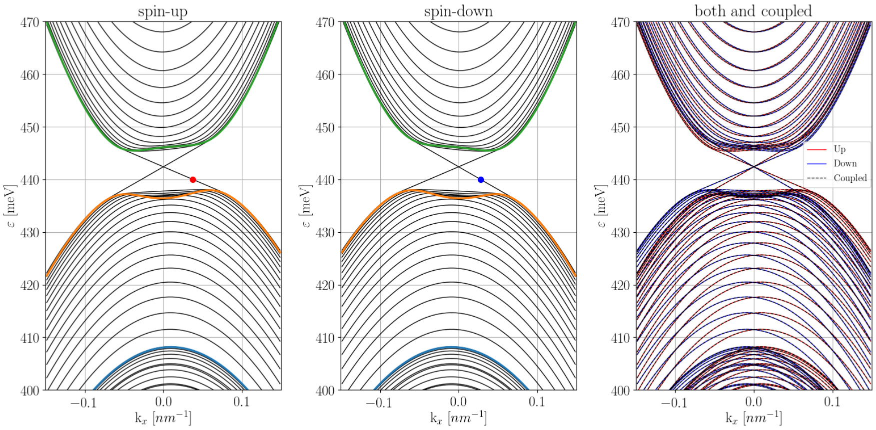

Figure 4.6: Spin separated bands for 97 Å thick system. In the rightmost panel we have both the uncoupled bands and those obtained with coupling, it is noted that the coupling has little effect on the energy scale of interest.

for the scattering region were 500×300 nm and the electric field applied in the growth direction is compatible with a band shift of 136 meV. Placing the Fermi energy in the region of the insulating gap, where we also see the formation of the double Dirac cone, we see the formation of helical edge states.

In order to study the behavior of the system with the variation of the electric field, we also analyzed the energy levels at $k_x = 0$ and their dependence on the electric field ($eF = \textit{electric field}$), such results appear in the figure graph (4.8). The question we want to answer here is whether or not we can speak of analogs to Landau levels for electric fields in this system.

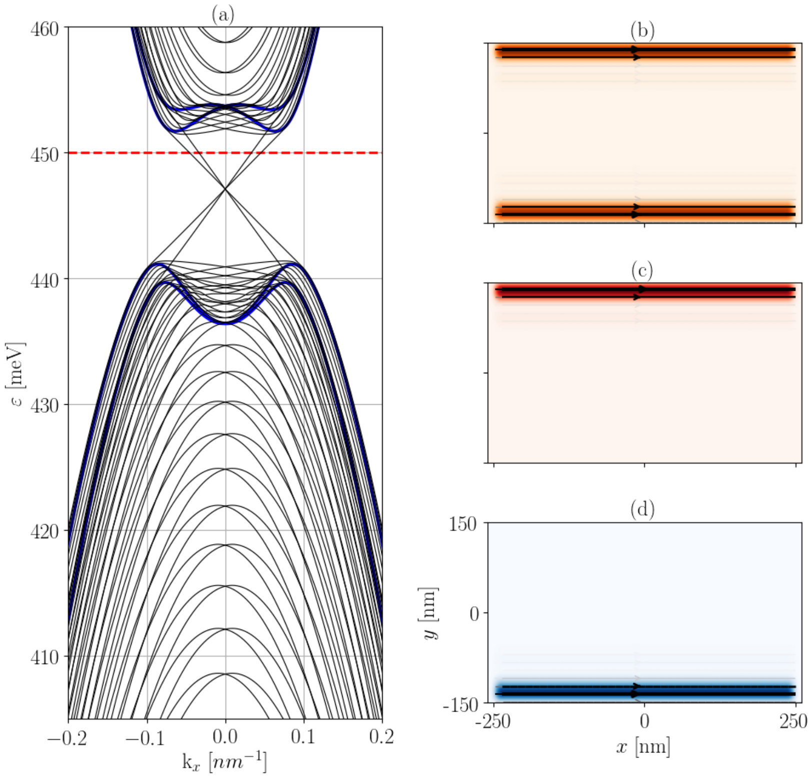

Figure 4.7: (*a*) Band structure for the 97 Å thick system subjected to an electric field of 70 meV in the growth direction; thin and black lines show the situation where we have confinement in the y-direction and the thick and colored lines show the situation without confinement; the dashed line shows the Fermi energy adopted in the current simulations. (*b*) The probability density that is defined by the wave function at the energy indicated by the dashed line in (a), (*c*) current density for the spin-Up component, and (*d*) current density for the spin-Down component.

4.5 Results for transport with metallic *leads*

As mentioned before, the results presented in the figure 4.7 were obtained with a system with translational symmetry in the x-direction. In this section, we present the results for systems whose semi-infinite leads have a Hamiltonian different from that of the scattering region. To simulate metallic behavior leads, the Hamiltonian adopted for the lead region represents free electrons of effective mass m_{ef}, that is

$$H_{\text{leads}} = \frac{\hat{p}^2}{2m_{\text{ef}}} + \hat{V}_{\text{cons}}, \tag{4.11}$$

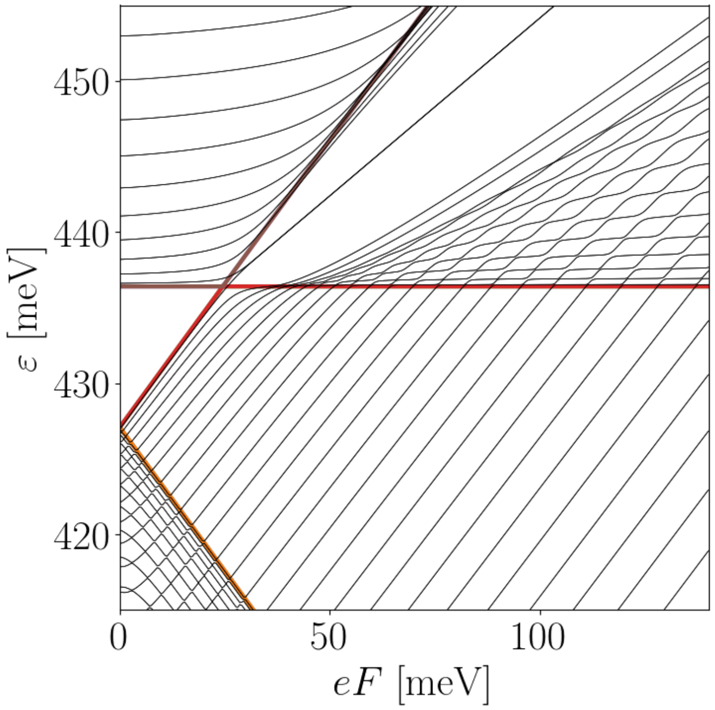

Figure 4.8: Dependence of energy levels on $k_x = 0$ with the electric field in the direction perpendicular to the plane of the well. Black lines represent the situation where there is confinement in the y-direction (strip), while thick and colored lines show levels calculated in a system with periodic boundary conditions (no edges).

where the potential $\hat{V}_{\text{cons}}$ is simply an additive constant to adjust the Fermi level, and in view of little or no effect on the final results, the effective mass was chosen so that it has the same order of magnitude as the conduction band of the scattering region.

When we place the Fermi energy in the region of the double Dirac cone, we see that current density accumulates at the edges of the scattering region. Furthermore, as anticipated by the shape of the band structure, the wave function is asymmetric in the y-direction. However, as the system is symmetrical by time-reversal when changing the incidence lead, the shape of the probability density is maintained, changing only the character of the pseudo-spins. This behavior is clear in the figure 4.9.

Analyzing the current patterns, we see that in the energy range where we have the Dirac cones there is still formation of edge states. In the figure 4.10 we see the separation of pseudo-spin currents. However, interesting patterns stop when the Fermi energy is

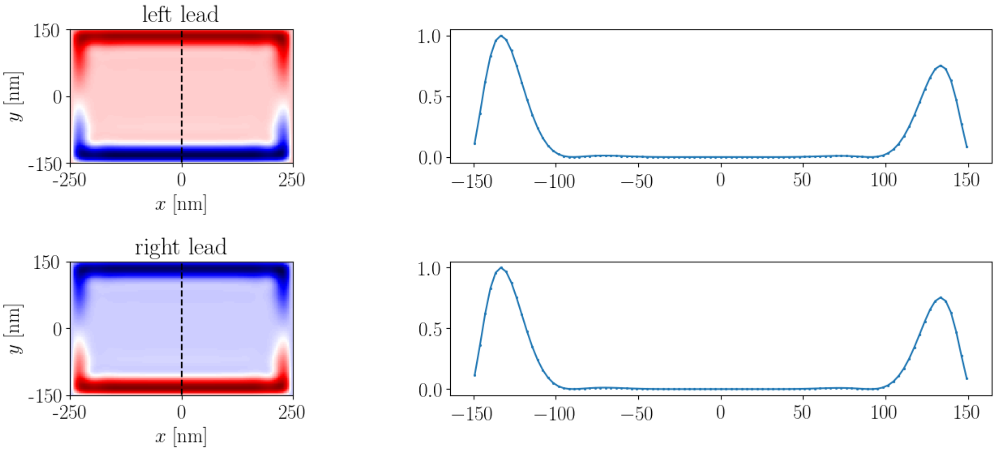

Figure 4.9: Spin density in the system of 97 Å with a Fermi energy of 440 meV and an *out-of-plane* electric field of 50 meV. In the upper panels, we have the spin density (red and blue represent the Up and Down spins respectively) when we have incident waves from the left lead while the lower panels represent the results obtained for waves incident to the right. The graphs on the right show the wave function profile in the dashed lines of the mappings on the left. Note the edge-dependent asymmetry.

placed in the vicinity of the bulk states. We see one of these patterns in the maps for the pseudo-spin currents present in the figure 4.11. What you see is the formation of current vortices that are evident when analyzing the pseudo-spin currents.

Calculating the system conductance for different values for the Fermi energy, we see that, in the region close to the bulk states of the valence band, the conductance peaks relate to the formation of these circular-current patterns. In the figure 4.12 we see how each current maxima is related to the formation of vortices. Very similar behavior is observed in the case of variable width systems, where a small gap in the Dirac spectrum is induced by the edge-states hybridization [64]. In that situation, the leads and the scattering region share the same Hamiltonian, and a constriction in the scattering region is responsible for the Fabry-Pérot resonances.

The origin of the Fabry-Pérot circular resonances, in the case presented here, is the mismatch between the Hamiltonians describing the leads and the scattering region. Similar to what is presented in [64], the crucial element for the emergence of these current patterns is the difference in carrier velocities for the leads and scattering region. This ex-

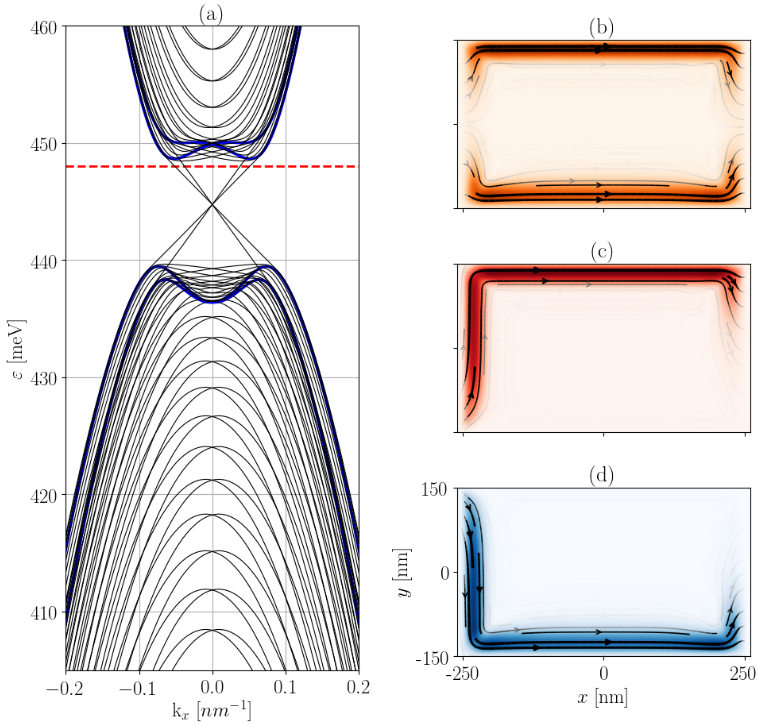

Figure 4.10: Results for the local current density in a 97 Å thick system with an *out-of-plane* electric field of 60 meV and a Fermi energy of 448 meV. (*b*) The probability density that for the energy indicated by the dashed line in (a), (*c*) current density for the spin-Up component, and (*d*) current density for the spin-Down component.

planation is supported by the fact that the formation of vortices occurs when the chemical potential crosses the local maxima of energy levels.

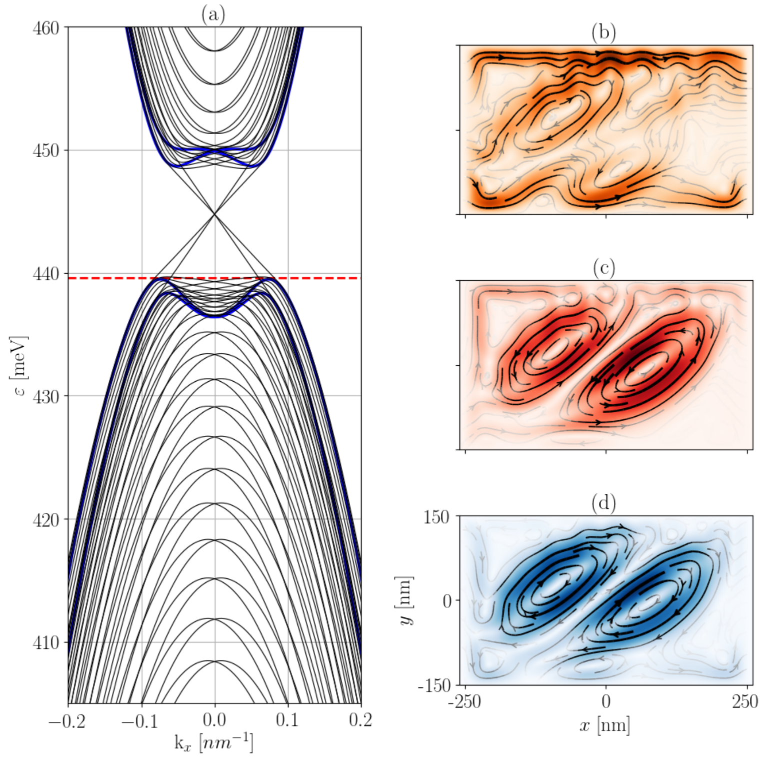

Figure 4.11: Results for the local current density in a 97 Å thick system with an *out-of-plane* electric field of 60 meV and a Fermi energy of 439.57 meV. Notice how the chemical potential in proximity to the bulk states leads to formation of vortices.(*b*) The probability density that for the energy indicated by the dashed line in (a), (*c*) current density for the spin-Up component, and (*d*) current density for the spin-Down component.

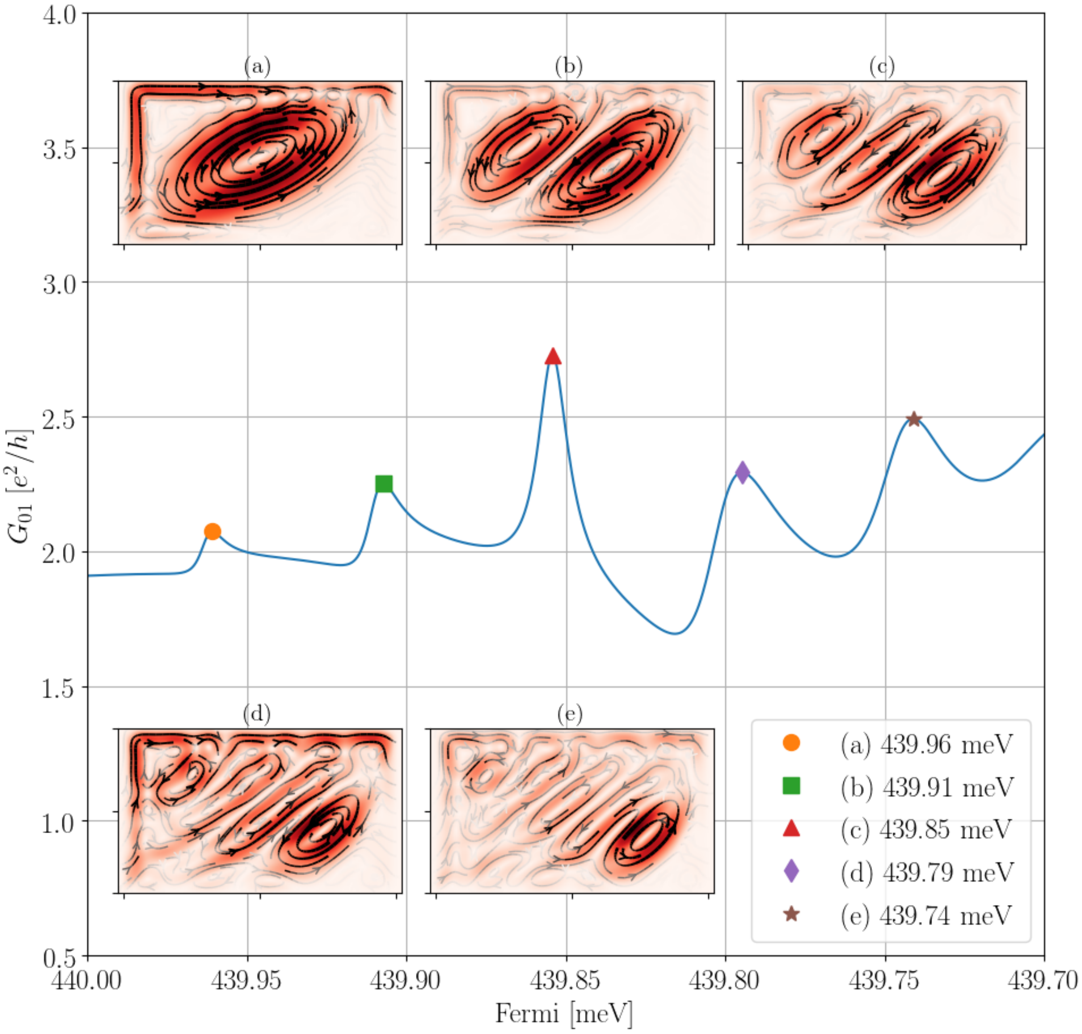

Figure 4.12: Curve obtained for the conductance between the metallic leads when varying the Fermi energy close to the boundary between the double Dirac cone and the bulk states. Panels (a)-(e) show the pseudo spin-Up current densities for the Fermi energies corresponding to the maximum conductance points.

Chapter 5

Excitons in transition metal dichalcogenides monolayers

The present and the next chapter describe the work carried out in collaboration with the group headed by Professor Jaroslav Fabian in Regensburg, Germany. The work focused on two distinct bidimensional systems: transition metal dichalcogenide monolayer and graphene. However, different phenomena were investigated in each of these systems. In this chapter, we present the research done to calculate and understand the excitonic states in encapsulated transition metal dichalcogenides. In the next chapter, we report the preparation stage for the investigation of weak localization in hydrogenated graphene.

5.1 Introduction

This introduction is greatly inspired by the text in Ref. [65]. In general, an exciton is a two-body system composed of an electron and a hole bonded via Coulomb interaction. Therefore, to describe an exciton, one can write its wave function as the linear combination of the product of a single (uncorrelated) electron and hole Bloch functions

$$\psi(\mathbf{r}_e, \mathbf{r}_h) = \sum_{\mathbf{k}_e} \sum_{\mathbf{k}_h} A(\mathbf{k}_e, \mathbf{k}_h) \psi_{ck_e}(\mathbf{r}_e) \psi_{ck_h}(\mathbf{r}_h), \tag{5.1}$$

where $A(\mathbf{k}_e, \mathbf{k}_h)$ represents the amplitude function. We can also write the envelope function for the exciton $\Phi(\mathbf{r}_e, \mathbf{r}_h)$, which is defined as the Fourier transform of the amplitude function $A(\mathbf{k}_e, \mathbf{k}_h)$:

$$\Phi(\mathbf{r}_e, \mathbf{r}_h) = \sum_{\mathbf{k}_e} \sum_{\mathbf{k}_h} A(\mathbf{k}_e, \mathbf{k}_h) \frac{e^{i\mathbf{k}_e \cdot \mathbf{r}_e}}{\sqrt{V}} \frac{e^{i\mathbf{k}_h \cdot \mathbf{r}_h}}{\sqrt{V}}, \tag{5.2}$$

which can be interpreted as the plane-wave expansion of the two-particle wave function.

One can adopt a effective mass approximation to find the wave function in Eq. (5.2), i.e.

$$[E_g + E_c(-i\nabla_e) - E_v(-i\nabla_h) + V(\mathbf{r}_e, \mathbf{r}_h)]\Phi(\mathbf{r}_e, \mathbf{r}_h) = E\Phi(\mathbf{r}_e, \mathbf{r}_h), \tag{5.3}$$

where we have replaced the $\mathbf{k}_{e(h)}$ in the dispersion relation for electron (hole) $E \equiv E(\mathbf{k}_{e(h)})$ to its corresponding differential operator $(-i\nabla_{e(h)})$ which acts on the electron (hole) coordinate space $\mathbf{r}_{e(h)}$.

In the parabolic approximation we can write $E_c(\mathbf{k}_e) = \hbar^2 k_e^2/2m_e^*$ for electrons, and $E_v(\mathbf{k}_h) = -\hbar^2 k_h^2/2m_h^*$ for holes. The potential part of the Hamiltonian may be of the form

$$V(\mathbf{r}_e, \mathbf{r}_h) = e\mathbf{F} \cdot (\mathbf{r}_e - \mathbf{r}_h), \tag{5.4}$$

which leads to the Franz-Keldysh effect when **F** is a uniform electric field. The interaction can also be of the form of a Coulomb interaction between the hole and the electron

$$V(\mathbf{r}_e, \mathbf{r}_h) = -\frac{e^2}{4\pi\varepsilon_s |\mathbf{r}_e - \mathbf{r}_h|}, \tag{5.5}$$

in this situation we will have the exciton effect, which will be matter of our primarily concern. In this work we have adopted a different potential to study excitons, the so-called Rytova-Keldysh potential, such a choice will be explained later in this chapter.

The Wannier equation

Replacing the operators into the equation 5.3 we get

$$[E_g - \frac{\hbar^2 \nabla_e^2}{2m_e} - \frac{\hbar^2 \nabla_h^2}{2m_h} + V(\mathbf{r}_e, \mathbf{r}_h)]\Phi(\mathbf{r}_e, \mathbf{r}_h) = E\Phi(\mathbf{r}_e, \mathbf{r}_h), \tag{5.6}$$

which can be rearranged in terms of the center of mass and relative coordinates, and, by separating the variables with the ansatz $\Phi(\mathbf{r}, \mathbf{R}) = \psi(\mathbf{r})\chi(\mathbf{R})$, one get a free particle equation for the center of mass, and a single particle equation submitted to a central potential $V(r)$:

$$\left[-\frac{\hbar^2\nabla_R^2}{2M}\right]\chi(\mathbf{R}) = E_R\chi(\mathbf{R}), \tag{5.7}$$

$$\left[-\frac{\hbar^2\nabla_r^2}{2\mu}+V(\mathbf{r})\right]\psi(\mathbf{r}) = E_r\psi(\mathbf{r}). \tag{5.8}$$

By Fourier transform the Eq. 5.8, and taking the summations properly, we arrive at

$$\sum_{\mathbf{k}} e^{i\mathbf{k}\cdot\mathbf{r}}\left[\frac{\hbar^2}{2\mu}k^2c_{\mathbf{k}}+\sum_{\mathbf{k}'}V_{\mathbf{k}-\mathbf{k}'}c_{\mathbf{k}'}\right] = E_r\sum_{\mathbf{k}} e^{i\mathbf{k}\cdot\mathbf{r}}c_{\mathbf{k}}. \tag{5.9}$$

Eliminating the summations and the exponentials on both sides of the Eq. 5.9, we get the equation for a single $\mathbf{k}$

$$\frac{\hbar^2}{2\mu}k^2c_{\mathbf{k}}+\sum_{\mathbf{k}'}V_{\mathbf{k}-\mathbf{k}'}c_{\mathbf{k}'} = E_rc_{\mathbf{k}}, \tag{5.10}$$

which is called the *Wannier equation* in reciprocal space.

Noticing that the Eq. 5.10 can be recast into matrix form, one can use well established numerical libraries to solve for the eigenvalues and eigenvectors. Basically, if the Fourier expansion coefficients $c_{\mathbf{k}}$'s is rearranged into a column vector $\mathbf{c}$, we can write the Wannier equation as

$$\left(\hat{P}+\hat{V}\right)\mathbf{c} = E_r\mathbf{c}. \tag{5.11}$$

The diagonal matrix $\hat{P}$ represents the kinetic part of the system, and its elements are given by $P_{\mathbf{k}} = \hbar^2\mathbf{k}^2/2\mu$. The interaction part of the equation is given by $\hat{V}$, which, in general, will be non-diagonal in k-space. The elements of $\hat{V}$ will depend on the actual potential used for the system. We will address this choice in the following section.

The effective Bethe-Salpeter equation

The Bethe-Salpeter equation (BSE) came from quantum field theory and is based on Feynman diagrams describing all interactions between two particles [66]. In the context of condensed matter physics, the BSE can be adapted to describe the excitons in semiconductors. Following [67, 68] the effective BSE for direct intralayer excitons can be written as an eigenvalue problem similar to the Wannier equation:

$$[E_c(\vec{k}) - E_v(\vec{k}) - \Omega_\lambda] F_{cv,\lambda}(\mathbf{k}) + \sum_{c'v'\mathbf{k}'} [\mathbb{D}^{cv\mathbf{k}}_{c'v'\mathbf{k}'} + \mathbb{X}^{cv\mathbf{k}}_{c'v'\mathbf{k}'}] F_{c'v',\lambda}(\mathbf{k}') = 0, \tag{5.12}$$

which can be treated as an eigenvalue equation, where Ω_λ is the λ-th eigenvalue we want, and the corresponding eigenstate is defined by

$$\Psi_\lambda(\mathbf{r}, \mathbf{r}') = \sum_{cv\mathbf{k}} F_{cv,\lambda}(\mathbf{k}) \psi_{c,\mathbf{k}}(\mathbf{r}) \psi_{v,\mathbf{k}}(\mathbf{r}'). \tag{5.13}$$

The interaction part of the BSE equation can be separated into the direct Coulomb term, represented by the matrix $\mathbb{D}^{cv\mathbf{k}}_{c'v'\mathbf{k}'}$,

$$\mathbb{D}^{cv\mathbf{k}}_{c'v'\mathbf{k}'} = \Delta^{cv\mathbf{k}}_{c'v'\mathbf{k}'} V(\mathbf{k} - \mathbf{k}'), \tag{5.14}$$

$$\Delta^{cv\mathbf{k}}_{c'v'\mathbf{k}'} = \left[\sum_l \alpha^*_{cl}(\mathbf{k}) \alpha_{c'l}(\mathbf{k}')\right] \left[\sum_m \alpha^*_{v'm}(\mathbf{k}') \alpha_{vm}(\mathbf{k})\right]. \tag{5.15}$$

and the exchange part given by the matrix $\mathbb{X}^{cv\mathbf{k}}_{c'v'\mathbf{k}'}$:

$$\mathbb{X}^{cv\mathbf{k}}_{c'v'\mathbf{k}'} = \frac{1}{A} \left[\int d\mathbf{r} \nabla^2 v(\mathbf{r})\right] \left[\frac{\langle c, \mathbf{k} | \vec{\Pi} | v, \mathbf{k} \rangle}{E_c(\mathbf{k}) - E_v(\mathbf{k})}\right] \left[\frac{\langle v', \mathbf{k}' | \vec{\Pi} | c', \mathbf{k}' \rangle}{E_{v'}(\mathbf{k}') - E_{c'}(\mathbf{k}')}\right] \tag{5.16}$$

The values designated as α_{cj} and α_{vm} are the components of the eigenvectors of the single-particle Hamiltonian adopted. The first index of α_{cj} (α_{vm}) identifies the conduction (valence) band to which the eigenvector is related, while the second index identifies the components of the eigenstate on chosen basis.

The results presented here were obtained disregarding the exchange contribution given by Eq. 5.16. The reason for that relies on the fact that the inclusion of the exchange term does not change qualitatively observables such as absorption spectra, leading to the same conclusions.

The Rytova-Keldysh potential

To include into the model the screening effect caused by the difference between the dielectric constant of the monolayer and its incapsulation, we adopted the Rytova-Keldysh (RK) potential [69]. Following the calculation presented in [70], one can get the expression for the RK potential in k-space

$$V(\vec{q}) = -\frac{1}{A}\left(\frac{e^2}{2\varepsilon_0}\right)\frac{1}{\varepsilon q + r_0 q^2}. \tag{5.17}$$

where $q = |\mathbf{k} - \mathbf{k}'|$, ε_0 is the vaccuum dielectric constant and r_0 is the screening length. For the semiconducting TMDCs such as WSe$_2$, MoSe$_2$ and MoS$_2$, r_0 is about 4.5 nm [71, 72]. Adopting the assumption that the TMDC has a negligible thickness, is common to see in the literature the value for ε defined as the average of the dielectric constants of the encapsulation materials,

$$\varepsilon = \frac{\varepsilon_t + \varepsilon_b}{2}, \tag{5.18}$$

being $\varepsilon_{t(b)}$ the value for the dielectric constant for the top (bottom) material.

5.1.1 Comparing results

Here we are primarily interested in investigating a general model describing a system where two conduction bands interact with one valence bands. Thus, an effective 3×3 model is adopted. Let us start by defining the Hamiltonian of the system of interest:

$$H(\vec{k}) = \begin{bmatrix} E_1 + \frac{\hbar^2}{2m_1^*}k^2 & 0 & 0 \\ 0 & E_2 + \frac{\hbar^2}{2m_2^*}k^2 & 0 \\ 0 & 0 & -\frac{\hbar^2}{2m_3^*}k^2 \end{bmatrix}, \tag{5.19}$$

which describes two conduction bands ($m_1^*$and $m_2^* > 0$) interacting with a valence band ($m_3^* > 0$). Here, we are adopting all effective masses positive and defining the kinetic energy for the hole as negative. First, we take the two possible electron-hole pairs and treat them using the Wannier equation to find the excitonic spectra. Then, we compare the results obtained by the BSE for the respective two-by-two Hamiltonians, and finally,

Table 5.1: Binding energy calculated with Wannier.

index	$m_1^* = 0.15$	$m_2^* = 0.25$
1	-320.3818	-339.4469
2	-0.7204	-98.4229
3	64.9041	-40.5658
4	64.9041	-40.5658
5	93.5776	-8.4528

we present the problem with the three-by-three model when the conduction bands cross each other.

For the sake of testing, we have adopted, for all calculations, a k-space grid of 11×11 points covering the values of $k_{x(y)}$ in the interval $\{-5, 5\}$ [nm^1]; for the effective masses we've used $m_1^* = 0.15$, $m_2^* = 0.25$, and $m_3^* = 0.4$; and the electron-hole interaction is mediated by Rytova-Keldysh potential:

$$V(\vec{q}) = -\frac{1}{A}\left(\frac{e^2}{2\varepsilon_0}\right)\frac{1}{\varepsilon q + r_0 q^2}, \tag{5.20}$$

The first five results for the binding energies obtained by solving the Wannier equation for both conduction effective masses (m_1^*, m_2^*) are presented in the table 5.1. To reach such results we have adopted, only for testing purposes, a 2D square k-space defined by an 11×11 grid with ± 5 nm^{-1} as its limits.

Now let's see what the most simple BSE equation gives us when we insert the same parameters adopted above. The Hamiltonian considered here is given by

$$H_{2x2} = \begin{bmatrix} E_g + \frac{\hbar^2}{2m_e}k^2 & 0 \\ 0 & -\frac{\hbar^2}{2m_h}k^2 \end{bmatrix}, \tag{5.21}$$

the dispersion relation for the parameters adopted here is presented in the figure 5.1.

The effective Bethe-Salpeter equation is given by

$$\left[E_c(\mathbf{k}) - E_v(\mathbf{k}) - \Omega_\lambda\right] F_{cv,\lambda}(\mathbf{k}) + \sum_{c'v'\mathbf{k}'} \mathbb{D}^{cv\mathbf{k}}_{c'v'\mathbf{k}'} F_{c'v',\lambda}(\mathbf{k}') = 0, \tag{5.22}$$

where we are not considering the exchange term and in which $\Omega_\lambda$is the λ-th eigenvalue

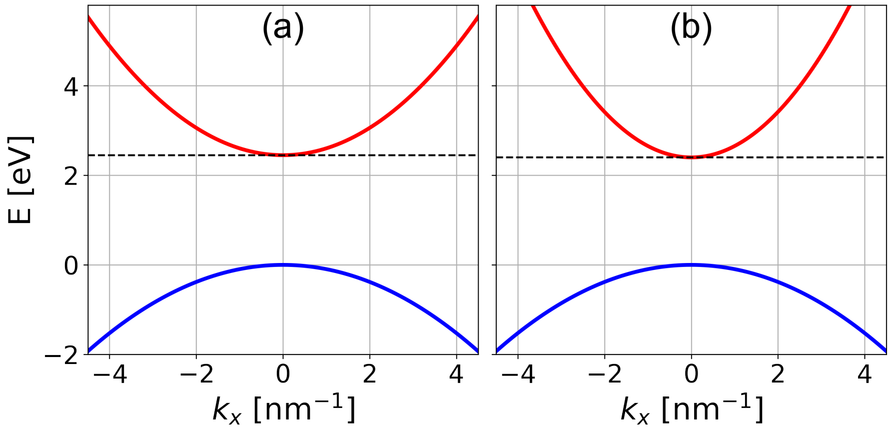

Figure 5.1: Energy dispersion for two different values of electron mass and energy gap: (a) $m_e = 0.25\, m_0$ and $E_g = 2.45$ eV, while (b) $m_e = 0.15\, m_0$ and $E_g = 2.40$ eV.

Table 5.2: Binding energy calculated with BSE, using the 2×2 model.

index	$m_1^* = 0.15$	$m_2^* = 0.25$
1	-320.3818	-339.4469
2	-0.7204	-98.4229
3	64.9041	-40.5658
4	64.9041	-40.5658
5	93.5776	-8.4528

corresponding to the eigenfunction in k-space $F_{cv,\lambda}(\mathbf{k})$ that, by its turn, is related to the envelope wave function for the λ-th excitonic state

$$\Psi_\lambda(\mathbf{r}, \mathbf{r}') = \sum_{cv\mathbf{k}} F_{cv,\lambda}(\mathbf{k}) \psi_{c\mathbf{k}}(\mathbf{r}) \psi_{v\mathbf{k}}(\mathbf{r}'). \tag{5.23}$$

The results for the binding energies in this case match those obtained by the Wannier equation, as one can see in the table 5.2.

Notice that, the Bethe-Salpeter equation for a 2×2 uncoupled system is equivalent to the Wannier equation. It's easy to see that if the following correspondencies are made

$$E_c(\mathbf{k}) = E_{gap} + \frac{\hbar^2}{2m_c^*} k^2, \tag{5.24}$$

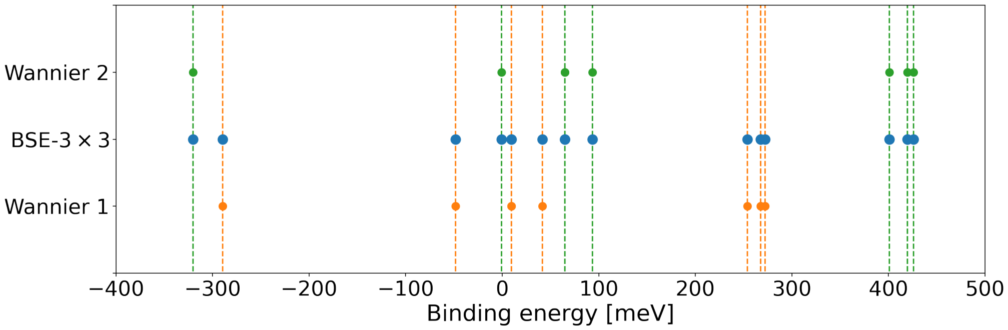

Figure 5.2: Comparison between the binding energies obtained by Wannier equation and by the Bethe-Salpeter equation. Notice that the BSE provide the same results the separated Wannier equations get.

$$E_v(\mathbf{k}) = -\frac{\hbar^2}{2m_v^*}k^2, \tag{5.25}$$

$$\mathbb{D}_{\mathbf{k}'}^{\mathbf{k}} = V(\mathbf{k}-\mathbf{k}'), \tag{5.26}$$

$$E_c(\mathbf{k}) - E_v(\mathbf{k}') = E_{gap} + \frac{\hbar^2}{2\mu}k^2. \tag{5.27}$$

5.1.2 Bethe-Salpeter equation with a 3×3 Hamiltonian

As a benchmark, we solved the BSE for the same set of parameters adopted in the previous section, but for the 3×3 Hamiltonian 5.19. To see if the Hamiltonian provides the same results obtained by the Wannier equation, we put the results in the figure 5.2 where we can see both sets of values.

Another important part of our results is the set of eigenfunctions corresponding to the binding energies. In a system composed of N conduction bands, M valence bands, and J k-space points, the $\lambda-$th eigenvector for the BSE can be written as

$$\mathbf{F}_\lambda = \sum_{cv\mathbf{k}} F_{cv}^{\lambda}(\mathbf{k})|c_{\mathbf{k}}, v_{\mathbf{k}}\rangle. \tag{5.28}$$

In the case we are working on, we have just one valence band and two conduction bands. Therefore, we can write the $\mathbf{F}_\lambda$ as a column vector following the order in which the conduction valence indexes run faster than the k-space vectors:

$$\mathbf{F}_\lambda = \begin{bmatrix} F^\lambda_{c_1 v}(\mathbf{k}_1) \\ F^\lambda_{c_2 v}(\mathbf{k}_1) \\ F^\lambda_{c_1 v}(\mathbf{k}_2) \\ F^\lambda_{c_2 v}(\mathbf{k}_2) \\ \vdots \\ F^\lambda_{c_2 v}(\mathbf{k}_N) \end{bmatrix} . \tag{5.29}$$

Moreover, the way that we identify the different conduction bands is an important detail that has to be addressed. By classifying based on their energy, the band crossings might be overlooked. As an example, let us consider the example where the states c_j are classified as follows:

- c_1 is the band with the highest value of energy; and
- c_2 is the second most energetic band.

Clearly our list of conduction bands has only two bands, while the valence bands list isn't even necessary, since we have just one valence band. However, our code is capable to handle an arbitrary number of conduction and valence bands. In general, the order of the states follows the following rule:

$$E_{c_1} > E_{c_2} > \cdots > E_{c_N} > E_{v_M} > E_{v_{M-1}} > \cdots > E_{v_2} > E_{v_1} \tag{5.30}$$

By following this rule, we can identify the bands of the dispersion relation presented in the figure 5.3. Notice the "inversion" of the conduction bands around the $k_x = 0$. This situation indicates that we have to analyze the wave functions to characterize the energy bands.

5.1.3 Results for the general 3×3 model

Let us focus on a more general model, which allows couplings between the conduction and the valence bands and between the conduction bands as well. The three bands model we are going to investigate has the following structure:

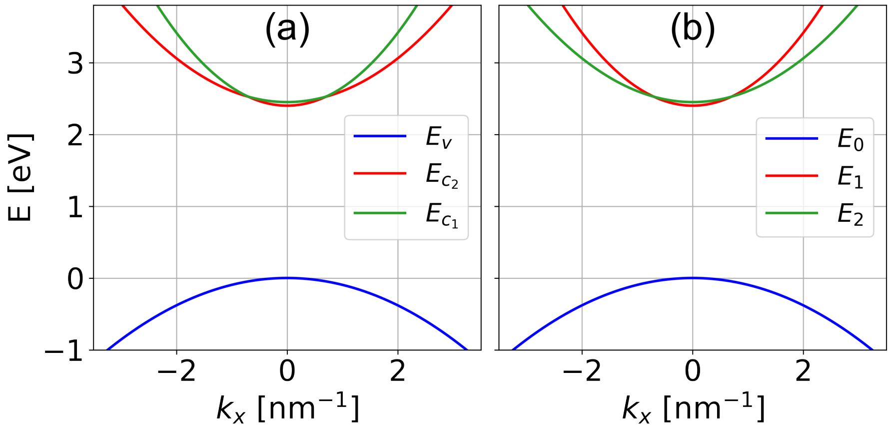

Figure 5.3: Band dispersion for the 3×3 model with bands identified, both cases without couplings ($P_{10} = P_{20} = P_{21} = 0$). (a) Identification based on the energy values, like indicated in Eq.(5.30). (b) The identification of the bands is based on their respective eigenvectors, which are the basis of the Hamiltonian in this uncoupled case. Notice that the energy order Eq.(5.30) still holds at a finite interval of k-values around $k_x = 0$ in (b).

$$H(\vec{k}) = \begin{bmatrix} E_2^{(0)} + F_2 k^2 & P_{21} k_\pm & P_{20} k_\pm \\ & E_1^{(0)} + F_1 k^2 & P_{10} k_+ \\ \text{c.c.} & & E_0^{(0)} + F_0 k^2 \end{bmatrix}, \tag{5.31}$$

where we have identified the basis adopted as $\{|2\rangle, |1\rangle, |0\rangle\}$ instead of $\{|c_2\rangle, |c_1\rangle, |v_1\rangle\}$ to allow the description of mixture when we turn the couplings on.

Among all the parameters available in our model, including the Hamiltonian 5.31 and the Rytova-Keldysh potential 5.20, the effective dielectric constant ε has the most direct way to control. Since the value of ε depends on the encapsulation of the TMDC monolayer, it is important to know how the excitonic spectra vary as one increases the value of ε. Starting from the resonance regime between the first exciton states, i.e. setting the values of E_2 and m_0 that make the first exciton states overlap in energy, the figure 5.4 shows how the binding energies change with ε.

Taking $P_{20} < P_{10}$ and changing P_{21}, we see that the resonating states separate in energy, even though the color of the lines in Figure (5.6) indicates that the states present a more degree of mixture. It is an interesting property and deserves more attention in future investigations.

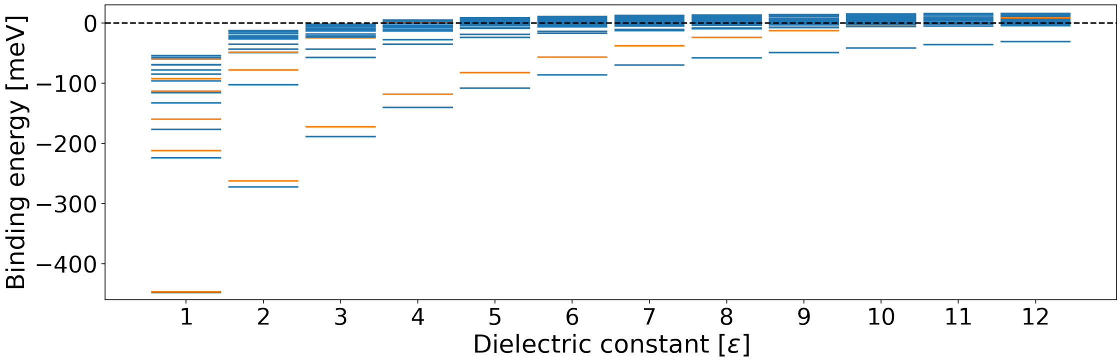

Figure 5.4: First 30 energy levels versus the value of dielectric constant. The different colors represent the different conduction band that contributes to the exciton wavefunction.

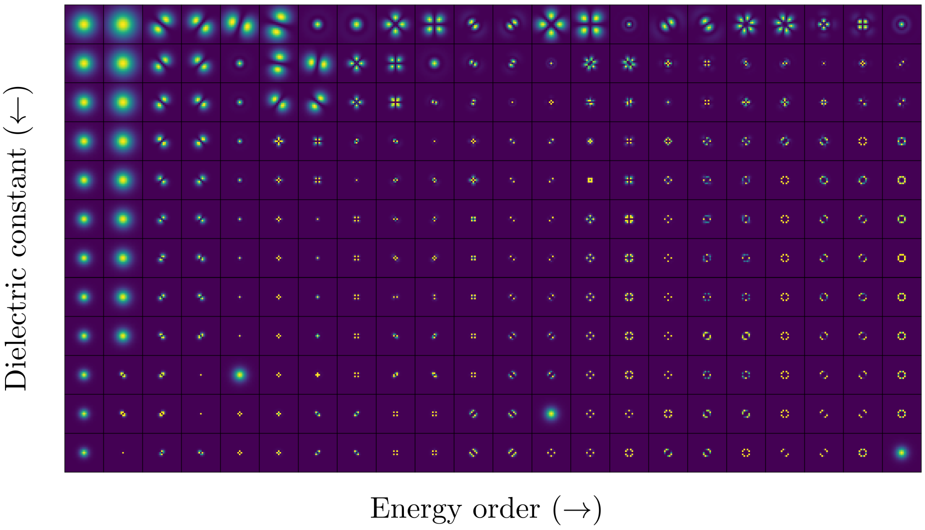

Figure 5.5: Wavefunctions in k-space for calculated excitons in the uncoupled regime. The horizontal direction represent the order in energy corresponding to each state, the vertical direction is related to the value of the dielectric constant, where each row correspond to a value of ε, starting on the top with $\varepsilon = 1$ and ending at the bottom with $\varepsilon = 12$.

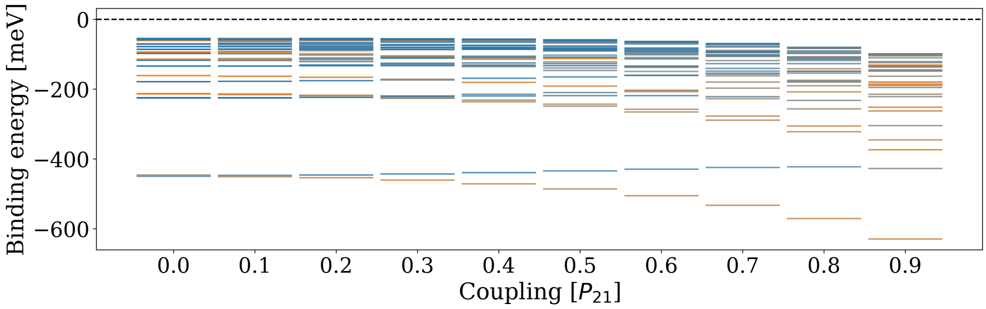

Figure 5.6: Energy levels for $P_{10} > P_{20}$ ($P_{10} = 2$ and $P_{20} = 0.5$ meV nm).

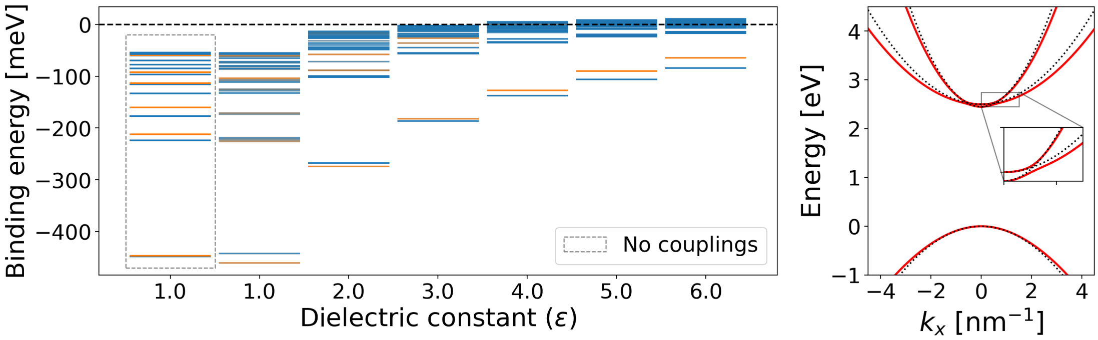

Figure 5.7: $P_{10} = 2$, $P_{20} = 0.5$, and $P_{21} = 0.3$

- $P_{10} = 2.0$ meV nm
- $P_{20} = 0.5$ meV nm
- $P_{21} = 0.3$ meV nm

To measure the mixing of the excitonic states we have used the difference of the projections over the conduction bands, i.e

$$\mathcal{P} = \sum_{\mathbf{k}} \left(|F_{c_2,v}(\mathbf{k})|^2 - |F_{c_1,v}(\mathbf{k})|^2 \right), \tag{5.32}$$

P_{10} [meV nm]	P_{20} [meV nm]	P_{21} [meV nm]
2.0	0.5	0.0
		0.3

Table 5.3: Coupling values

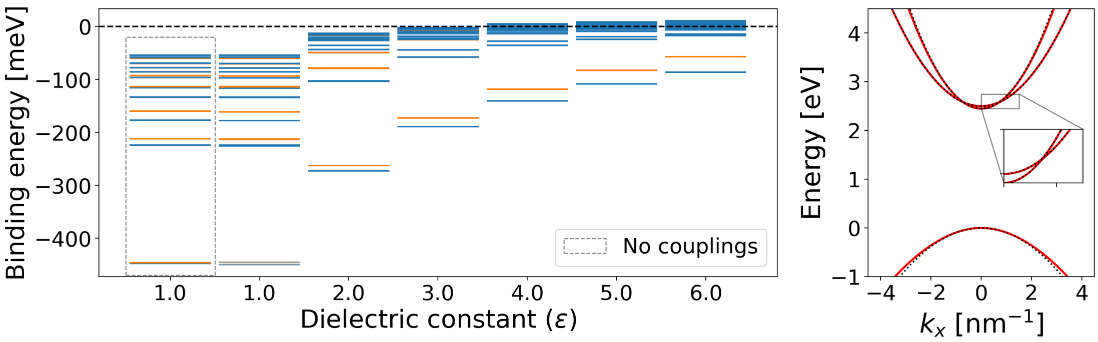

Figure 5.8: $P_{10} = 2$, $P_{20} = 0.5$, and $P_{21} = 0$

where the total wave function for the exciton is supposed normallized

$$\sum \left(|F_{c_2,v}(\mathbf{k})|^2 + |F_{c_1,v}(\mathbf{k})|^2\right) = 1. \tag{5.33}$$

5.1.4 Absorption analysis

The absorption spectrum considering the excitonic effects can be calculated by

$$\alpha^a(\hbar\omega) = C_0 \sum_N \left| \sum_{cv\vec{k}} F_{cv\vec{k}}(N) p^a_{vc}(\vec{k}) \right|^2 \delta(\Omega_N - \hbar\omega), \tag{5.34}$$

where the superindex a indicates the light polarization. The prefactor C_0 is given by $C_0 = 4\pi^2 e^2/\varepsilon_0 c_l \omega A \hbar^2$, where c_l being the speed of light, and A the 2D unit area. The quantity represent by p^a_{nm} is known as the dipole matrix element and is defined by

$$p^a_{nm} = \frac{\hbar}{m_0} \langle n, \vec{k} | \hat{e}_a \cdot \vec{p} | m, \vec{k} \rangle, \tag{5.35}$$

where the light polarization given by the unity vector $\hat{e}_a$. For the absorption final result, we apply a Lorentzian broadening

$$L(x, x_0; \Gamma) = \frac{1}{\pi} \frac{\frac{1}{2}\Gamma}{(x - x_0)^2 + (\frac{1}{2}\Gamma)^2}, \tag{5.36}$$

with a constant width at half-maximum $\Gamma = 10$ meV.

Exploring the coupled three bands model, the results in the figure 5.9 shows how the spectra dependence with the effective dielectric constant (ε). The most prominent peak

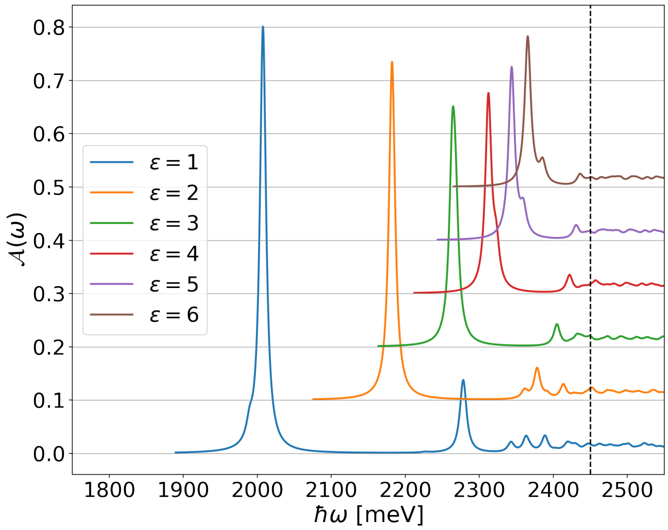

Figure 5.9: Excitonic absorption spectra for different values of dielectric constant. The vertical shift was introduced only to improve visualization.

indicates the absorption of the exciton composed of an electron from the most strongly coupled conduction band, whose wavefunction has the s-orbital symmetry. Notice the existence of a weaker peak passing through the larger one, from left to right, as the dielectric constant increases. This second peak comes from the exciton whose electron comes from the weakly coupled conduction band and, similarly to the first peak, it also has an even wavefunction.

Until now, the freedom in the definition of the signs in the coupling terms was not relevant, in the sense that the choice between plus and minus in $P_{AB}k_{\pm}$ did not reflect in the results. However, for the absorption spectra for different light polarizations, this choice is important. In the results presented in Fig. 5.10, we see that, depending on the sign present in the coupling between the second conduction band and the valence band, it is possible to get a separated spectrum for excitons of different conduction bands. The coupling between the first conduction band and the valence bands was kept constant and depending on momentum by $P_{10}k_{+}$. By the particular choice of parameters, the influence of $P_{21}k_{\pm}$ was not clear, and more investigations are required.

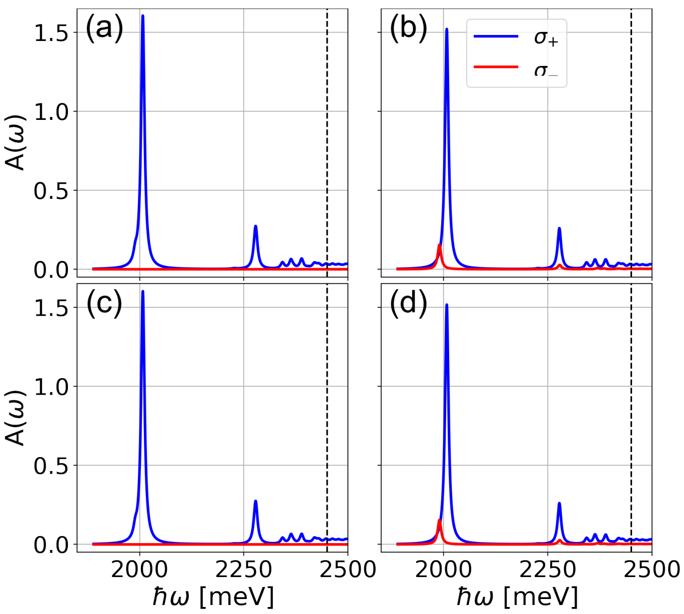

Figure 5.10: Excitonic absorption spectra for light with different polarization for models with different chiralities. (a) $P_{20}k_+$ and $P_{21}k_+$, (b) $P_{20}k_-$ and $P_{21}k_+$, (c) $P_{20}k_+$ and $P_{21}k_-$, (d) $P_{20}k_-$ and $P_{21}k_-$.

5.1.5 Rashba SOC in TMDC

The next steps in this project consist to change our focus towards a more realistic model. Using a modified model based on the whork in [71], the $\mathbf{k} \cdot \mathbf{p}$ Hamiltonian in the vicinity of K-point of the Brillouin zone of the TMDC could be written as a sum of the following components:

$$H_0 = \begin{bmatrix} E_{vb} & 0 & 0 & 0 \\ 0 & E_{vb} & 0 & 0 \\ 0 & 0 & E_{cb} & 0 \\ 0 & 0 & 0 & E_{cb} \end{bmatrix}, \tag{5.37}$$

$$H_{SO} = \begin{bmatrix} \Delta_{vb} & 0 & 0 & 0 \\ 0 & -\Delta_{vb} & 0 & 0 \\ 0 & 0 & +\Delta_{cb} & 0 \\ 0 & 0 & 0 & -\Delta_{cb} \end{bmatrix}, \tag{5.38}$$

$$H_{1kp} = \pm\gamma \begin{bmatrix} 0 & 0 & k_+ & 0 \\ 0 & 0 & 0 & k_+ \\ k_- & 0 & 0 & 0 \\ 0 & k_- & 0 & 0 \end{bmatrix}, \tag{5.39}$$

$$H_{2kp} = \begin{bmatrix} \tilde{\alpha}_\uparrow k^2 & 0 & \kappa_\uparrow k_+^2 & 0 \\ 0 & \tilde{\alpha}_\downarrow k^2 & 0 & \kappa_\downarrow k_+^2 \\ \kappa_\uparrow k_-^2 & 0 & \tilde{\beta}_\uparrow k^2 & 0 \\ 0 & \kappa_\downarrow k_-^2 & 0 & \tilde{\beta}_\downarrow k^2 \end{bmatrix}. \tag{5.40}$$

Such matices are written in the basis given by $\{|v_K \uparrow\rangle, |v_K \downarrow\rangle, |c_K \uparrow\rangle, |c_K \downarrow\rangle\}$. Now, let's insert a term of Rashba spin orbit coupling between the two conduction bands only. Following the work in [73] we can write the Rashba term, in the spin basis $\{|\uparrow\rangle, |\downarrow\rangle\}$ as

$$\begin{aligned} \tilde{H}_R &= \alpha(k_x\sigma_x - k_y\sigma_x) \\ &= \alpha\left[k_x \begin{pmatrix} 0 & -i \\ i & 0 \end{pmatrix} - k_y \begin{pmatrix} 0 & 1 \\ 1 & 0 \end{pmatrix}\right] = \alpha \begin{pmatrix} 0 & -ik_x - k_y \\ ik_x - k_y & 0 \end{pmatrix} \\ &= \alpha \begin{pmatrix} 0 & -i(k_x - ik_y) \\ i(k_x + ik_y) & 0 \end{pmatrix} = \alpha \begin{pmatrix} 0 & -ik_- \\ ik_+ & 0 \end{pmatrix}. \end{aligned} \tag{5.41}$$

In this way, one can write the Rashba contribution to the Hamiltonian in the basis $\{|v_K \uparrow\rangle, |v_K \downarrow\rangle, |c_K \uparrow\rangle, |c_K \downarrow\rangle\}$ as

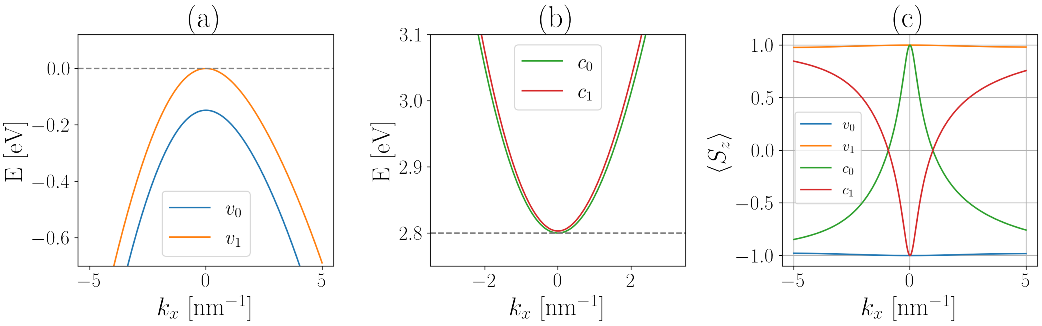

Figure 5.11: Energy bands of MoS$_2$ with Rashba SOC for both conduction and valence bands given by $\alpha_{c(v)b} = 5$ meV nm. In the panels, we see (a) the valence bands, (b) the conduction bands, and (c) the s_z-projection of each band. Notice that one can adopt a model without the SOC between the valence bands, since the s_z-projection is approximately constant.

$$H_R = \begin{bmatrix} 0 & -i\alpha_{vb}k_- & 0 & 0 \\ i\alpha_{vb}k_+ & 0 & 0 & 0 \\ 0 & 0 & 0 & -i\alpha_{cb}k_- \\ 0 & 0 & i\alpha_{cb}k_+ & 0 \end{bmatrix}. \tag{5.42}$$

From now on, we're going to adopt $\alpha_{vb} = 0$, which means that we'll ignore the Rashba coupling between the valence bands. Since the systems we're interested in have large spin-splitting for the valence bands when one compares it with the splitting of the conduction bands, such an approximation is quite reasonable. This feature can be easily seen by comparing the spin polarization of the conduction bands with that for the valence band as shown in the c-panel of Fig. 5.11 and both panels at Fig. 5.12.

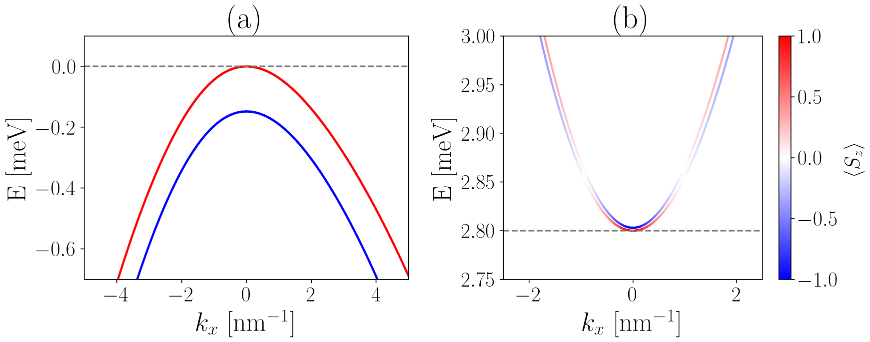

Figure 5.12: Energy bands for MoS$_2$ with a color scale indicating the z-projection of spin in unities of $\hbar/2$. In panel (a) we see the valence bands that have the spin projection well defined in the interval. Panel (b) shows the conduction bands, which present crossings and changings in the spin projection.

Chapter 6

Weak localization in Hydrogenated Graphene

6.1 Introduction

When the distances between the scatterers in a conducting system are greater than the phase relaxation length, Ohm's law describes a linear dependence of the resistance with the length of the conductor ℓ_ϕ. This scenario can change for low temperatures in systems with low mobilities. In this situation the free mean path can be smaller than ℓ_ϕ. In this way, the overall conductance of the such systems will decrease due to interference effects. For conductors with conductance much greater than e^2/h, this decrease is approximate to e^2/h. If the physical system meets such conditions, we say it is in the *weak localization* (WL) regime. Since a small magnetic field, around 100 G, could destroy the effects of WL, one can use magnetoresistance measurements to identify the phenomenon.

Here, the idea is to study the weak localization in Graphene with Hydrogen adatoms. Using tight-binding modeling, we can implement a numerical simulation using the Kwant Python package [27]. The Hydrogen adatoms on the system will play the role of scatterers and will cause the reflections responsible for the weak localization.

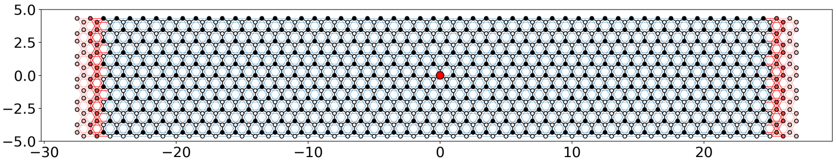

Figure 6.1: Graphene strip with zig-zag boundaries and an adatom on top of the Carbon atom at the position $\mathbf{r} = 0$. At both ends of the strip, we have semi-infinite leads.

6.2 Tight-binding model

To start the investigations, we have been exploring the simpler system composed of a zig-zag nanoribbon with an adatom in the middle, see Fig. 6.1. The tight-binding model adopted for this system is that given by the reference [74]. Basically, our model can be split into two parts, an orbital part, and the spin-orbit part,

$$H = H_{\text{orb}} + H_{\text{so}}. \tag{6.1}$$

In what follows we have adopted the notation where $c_{i\sigma}^{\dagger} = (a_{i\sigma}^{\dagger}, b_{i\sigma}^{\dagger})$ and $c_{i\sigma} = (a_{i\sigma}, b_{i\sigma})$ represent the creation and annihilation operators for the p_z-orbitals on both A and B graphene sublattices. The creation and annihilation operators for the Hydrogen s-orbitals located at the site m are given respectivelly by $h_{m\sigma}^{\dagger}$ and $h_{m\sigma}$. The orbital part of 6.1 is given by

$$H_{\text{orb}} = \varepsilon_h \sum_{m} h_{m\sigma}^{\dagger} h_{m\sigma} - t \sum_{\langle i,j \rangle} c_{i\sigma}^{\dagger} c_{j\sigma} + T \sum_{\langle m,i \rangle} h_{m\sigma}^{\dagger} c_{i\sigma} + \text{h.c.} \tag{6.2}$$

where $\varepsilon_h = 3$ eV is the adatom on-site energy, $T = 6.5$ eV is the Hydrogen-Carbon hopping term, and $t = 2.6$ eV is the hopping between the Carbon atoms energy [74].

The minimal realistic model for SOC has its effects confined up to the second-nearest neighbors of the hydronated site C_H (in sublattice A), which defines our impurity region. Defining $A_{\sigma}^{\dagger}$ (A_{σ}) as the creation (annihilation) operator on C_H and $B_{m\sigma}^{\dagger}$ $(B_{m\sigma})$ as the creation (annihilation) operator on the three nearest neighbors of C_H. The tight-binding Hamiltonian can be written as

$$
\begin{aligned}
H_{\text{so}} = &\frac{i}{3} \sum_{\langle\langle i,j\rangle\rangle}^{\prime} c_{i\sigma}^{\dagger} c_{j\sigma'} \left[\frac{\lambda_I}{\sqrt{3}} \nu_{ij} \hat{s}_z\right]_{\sigma\sigma'} \\
&+ \frac{i}{3} \sum_{\langle\langle C_H,j\rangle\rangle} A_{\sigma}^{\dagger} c_{j\sigma'} \left[\frac{\Lambda_I}{\sqrt{3}} \nu_{C_H,j} \hat{s}_z\right]_{\sigma\sigma'} \\
&+ \frac{2i}{3} \sum_{\langle C_H,j\rangle} A_{\sigma}^{\dagger} B_{j\sigma'} \left[\Lambda_{\text{BR}} (\hat{\mathbf{s}} \times \mathbf{d}_{C_H,j})_z\right]_{\sigma\sigma'} + \text{h.c.} \\
&+ \frac{2i}{3} \sum_{\langle\langle i,j\rangle\rangle} B_{i\sigma}^{\dagger} B_{j\sigma'} \left[\Lambda_{\text{PIA}} (\hat{\mathbf{s}} \times \mathbf{D}_{i,j})_z\right]_{\sigma\sigma'},
\end{aligned}
$$

where the individual terms and parameters assume the following interpretation and values:

- The first term models the intrinsic spin-orbit coupling for the Graphene, and it is characterized by $2\lambda_I = 24\ \mu$eV. It couples every next-nearest-neighbor pairs that do not contain C_H (indicated by the prime).
- The second term indicates the adatom-induced intrinsic SOC, and its strength is given by $\Lambda_I = -0.21$ meV (17 times stronger than λ_I). It couples the same spin in the same sublattice.
- The third term is the Bychkov-Rashba term, which induces the nearest neighbors spin-flip. The value of $\Lambda_{\text{BR}} = 0.33$ meV is more than 60 times stronger than the value for Graphene in a representative electric field of 1 V/nm ($\lambda_{\text{BR}} = 5\ \mu$eV).
- The last term comes from the pseudo-spin asymmetry and couples different spins from next-nearest-neighbors. The value of $\Lambda_{\text{PIA}} = -0.77$ meV has no counterpart in flat Graphene.

To introduxe an out-of-plane magnetic field into our system, we have implemented the Peierls substitution, where the original hoppings are replaced by

$$
t_{i,j} \to t_{i,j} e^{i\phi_{ij}}, \tag{6.3}
$$

where the Peierls phase is defined by

$$
\phi_{ij} = \frac{e}{\hbar} \int_{\mathbf{r}_i}^{\mathbf{r}_j} \mathbf{A} \cdot d\mathbf{l}, \tag{6.4}
$$

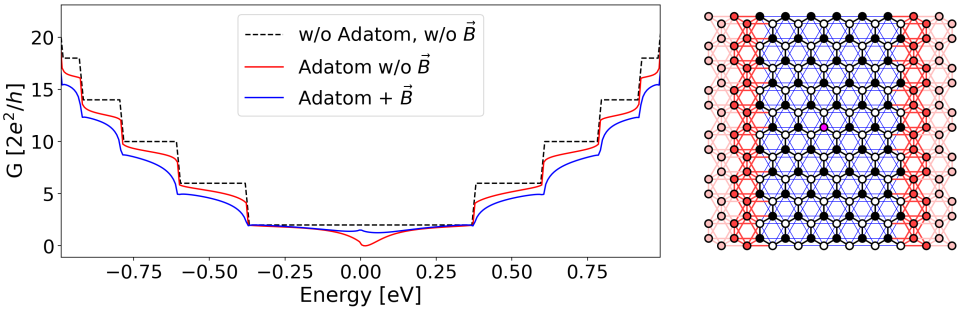

Figure 6.2: Comparison between systems with a single Adatom in the middle, with and without magnetic field.

with $\mathbf{A}$ being the vector potential, and $\mathbf{r}_i$ the position of the i-th atom. To get a zero magnetic field in the leads, and a magnetic field pointing in the z-direction we adopt the Landau gauge given by

$$\mathbf{A}(\mathbf{r}) = \hat{\mathbf{y}} B \bar{x}, \tag{6.5}$$

$$\bar{x} = \begin{cases} 0, & x < 0 \\ x, & 0 \leq x \leq d \\ d, & x > d \end{cases} . \tag{6.6}$$

Notice that the vector potential can not be set to zero in the $x > d$ region, as this would imply an infinite magnetic field at the $x = d$ interface.

6.3 Preliminar results

The first step was to model the system using Kwant and benchmarking some preliminary results. In the current stage, we still deciding the best way to benchmark, trying to find reliable sources in the literature. The following results present the first outcomes of our numerical calculations.

Since our main interest is to investigate the weak localization in Graphene, we need a system with $N > 1$ adatoms distributed sparsely. The sparsity of the adatom distribution is necessary given the validity of our tight-binding model [74]. Initially, however, before

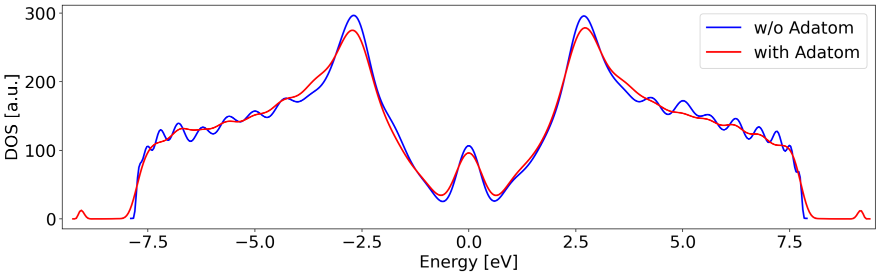

Figure 6.3: Total density of states comparison between the systems with and withou the adatom. Both the systems have a rectangular shape and zig zag bouraries. The adatom was placed on top of the Carbon atom at the origin of the coordinate system, which is approximately the center of the system.

including more than a single adatom, it is crucial to guarantee that the model is well defined in the simplest scenario.

Firstly, we calculated the conductance of the system without adatoms. Then, we compared it when an adatom was included, both with and without the presence of magnetic field. In Fig. 6.2 we see that the presence of an adatom decreases the transmission through the system for all values of chemical potential. When a non-zero magnetic field is applied, the transmission decrease even further, except for energies close to zero.

Looking into the density of states of the system could give us some insights into the system. In Fig. 6.3 the density of states shown was obtained using the kernel polynomial method (KPM), where we can see that the inclusion of an adatom does not modify significantly the total density of states. On the other hand, we calculate the local density of states in the central position, we have a dramatic change when we add the adatom. The important features are the appearance of a peak for energy zero and the very high peaks at both ends of the energy range.

Exploring further to better understand the differences between the systems with and without the adatom, we the plotted the local density over the system for specific values of energy. In the color maps in the Fig. 6.5 we see, in the upper panel, the existence of an edge states which contribute to the total density around zero energy. The bottom panel of Fig. 6.5 shows the extended states away from zero.

The results in Fig. 6.6 shows us the concentration of states around the adatom site. In

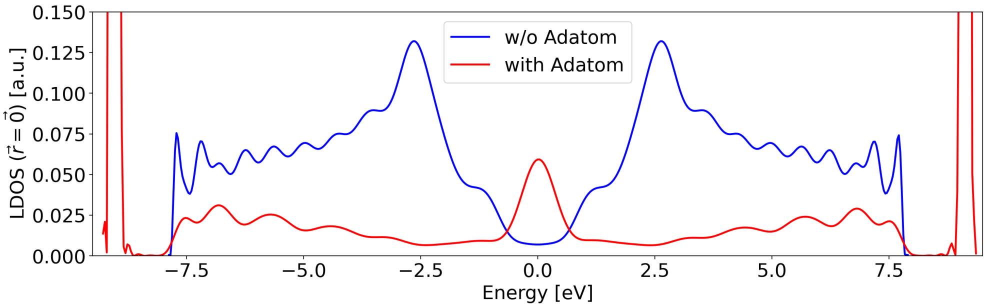

Figure 6.4: Local density of states (LDOS) for the position $\vec{r} = 0$. In blue we have the results for the system without the adatom while the red line shows the results for the system with the adatom positioned at the center. The important features here is the presence of the peak for energy zero, and the very high peaks at the both ends of the energy range.

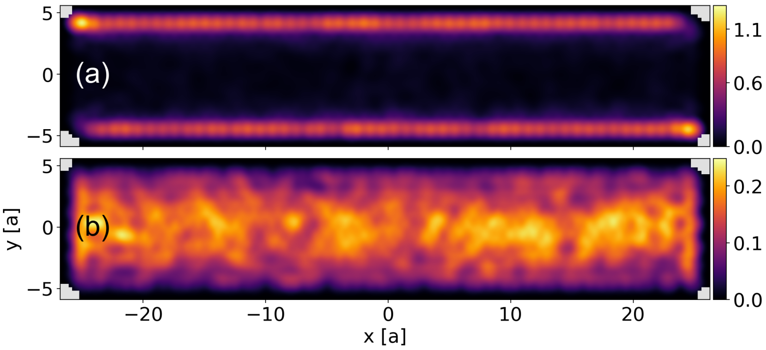

Figure 6.5: Color map for the local density of states for the system without adatom. In the panel (a) we have the mapping for $E = 0$, and in (b) we have the mapping for the $E = 1$ eV.

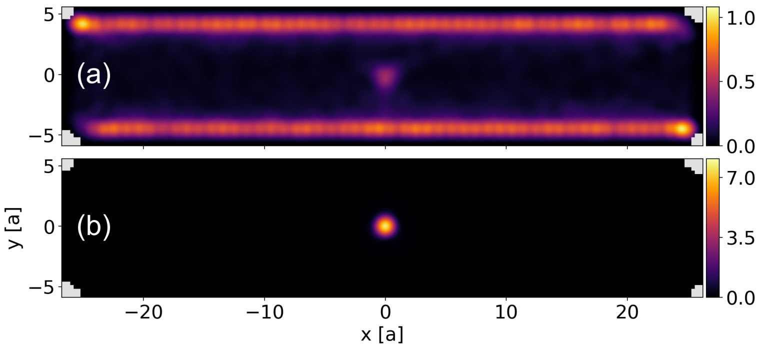

Figure 6.6: Local density of states for the system with a Hydrogen adatom in the center. The panel (a) shows the results for $E = 0$, while the panel (b) presents the mapping for energy corresponding to the highest value of density $E = 9.17$ eV.

the upper panel of Fig. 6.6 we see that, for zero energy, the edge states have the company of states localized in the middle site. The bottom panel, on the other hand shows the high density in the adatom site for energy around 9.17 eV, which correspond to the pronounced peaks at the ends of the plot in Fig. 6.4.

6.4 Spin relaxation benchmark tests

Seeking to validate the tight-binding model and obtain a benchmark for the code, we decided to reproduce some results already published. Since most of the published results refer to systems with translational symmetry in both directions of the plane, we will use the artifice of joining the edges of the system by means of additional hoppings, thus creating a system equivalent to a nanotube, as can be seen in Figure 6.7. In this way, an approximation of a system that would extend in both directions of the plane can be obtained.

Initially, the density of states of the system without the presence of Adatoms was calculated, i.e. pure graphene, and with the addition of hydrogen and fluor. The results with which we compare our results can be seen in Figure 6.8 which in turn presents the density of states obtained through calculations using the T-matrix formalism [6]. To efficiently use computational resources, we adopted the method known as *kernel polynomial method*, or KPM [75]. In this method, the density of states is approximated by an expansion of Chebyshev polynomials of a stochastic trace, which in turn is understood as the average

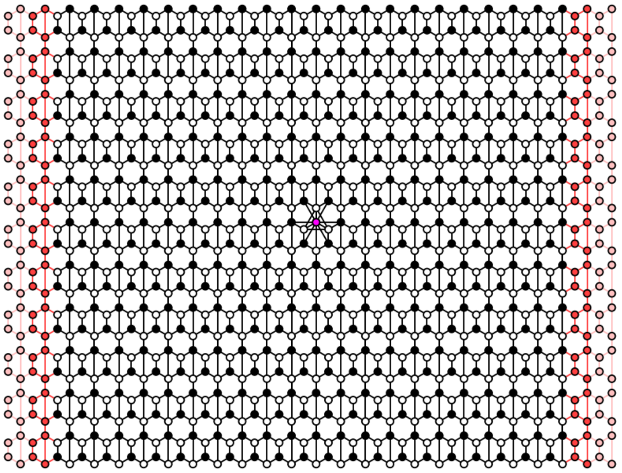

Figure 6.7: Graphene lattice with periodic boundarie conditions in y-direction and an adatom on top of the Carbon atom at the center. At the both ends of the system we have the semi infinite leads both with periodic boundarie conditions in y-direction as well.

of the expected value calculated on random vectors:

$$\rho(E) = \mathrm{Tr}(\delta(E-H)) \sim \frac{1}{R}\sum_r \langle r|\delta(E-H)|r\rangle. \tag{6.7}$$

To validate the implementation of the spin-orbit and magnetic moment terms, we chose to compare the results for the spin relaxation rate. Initially, we calculated the spin exchange probability (*spin-flip*) $\Gamma_s(E)$, defined by

$$\Gamma_s(E) = \sum_{\sigma\in\{\pm1\}}\sum_{i,j}\left(|t_{i,j;\sigma,-\sigma}|^2 + |r_{i,j;\sigma,-\sigma}|^2\right), \tag{6.8}$$

where $t_{i,j;\sigma,-\sigma}$ and $r_{i,j;\sigma,-\sigma}$ are the transmission and reflection coefficients with spin-flip, which were obtained numerically using KWANT. Then, the spin relaxation rate, for zero temperature, was calculated by the expression

$$\tau_s^{-1}(E) = \frac{2\pi}{\hbar}\eta\frac{t}{\pi a}\sum_{\tau\in\{\pm\}}\sigma_s^\tau(E) = \frac{4t}{\hbar}\eta\frac{W}{a}\Gamma_s(E), \tag{6.9}$$

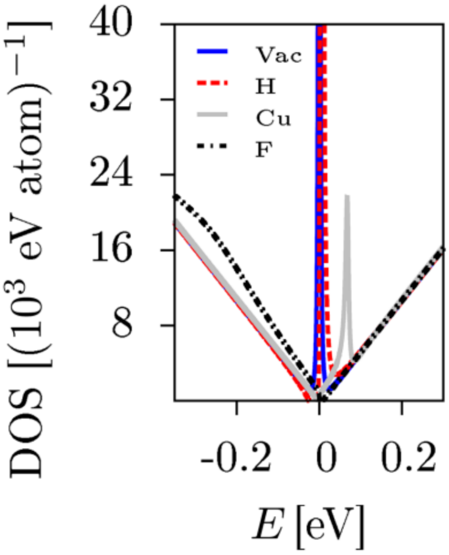

Figure 6.8: T-matrix formalism results for the density o states for pristine graphene, vacancy model (Vac) and with different adatoms in top position: Hydrogen (H), $\omega = 7.5$ eV and $\varepsilon = 0.16$ eV, copper (Cu), $\omega = 0.81$ eV and $\varepsilon = 0.08$ eV, and florine (F), $\omega = 5.5$ eV and $\varepsilon = -2.2$ eV. This image was published as Fig. 7 in [6].

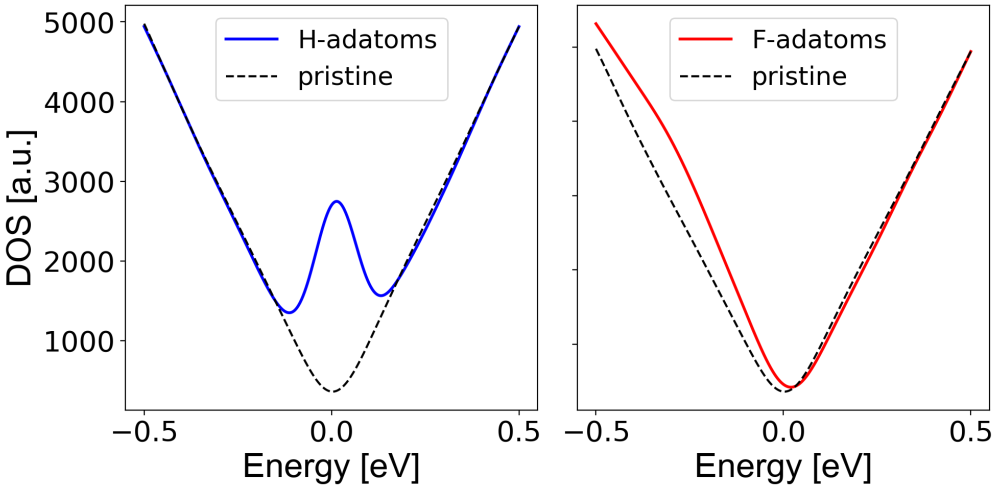

Figure 6.9: (a): Numerical results, using KWANT implementation of kpm, for the density of states for graphene with 0.1% of hydrogen adatoms concentration; and (b): DOS for graphene with 0.1% of fluorine. Even though the approximations required to perform the calculations have smoothed out the sharp resosance of the result for Hydrogenated adatom, we have a very good qualitative result in comparison with those in Fig. 6.8.

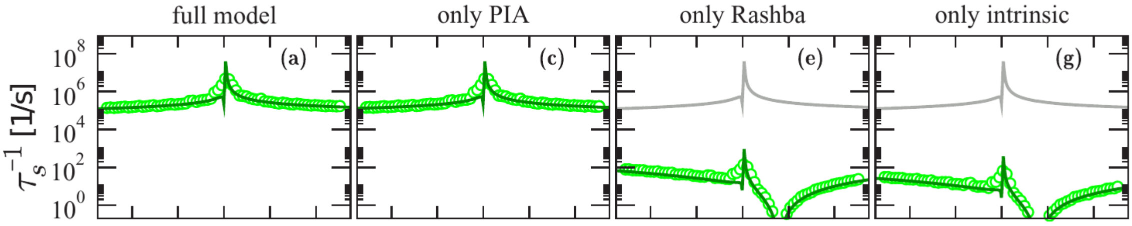

Figure 6.10: Calculated spin-relaxation rates as functions of the Fermi level for hydrogenated graphene. Symbols represent numerical Landauer-type (recursive Green's functions) calculations and solid lines come from the analytical T-matrix analysis. (a) result considering the full Hamiltonian, (c),(e) and (g) show the results when only one spin-orbit term is considered. This figure is part of a larger figure published in [7].

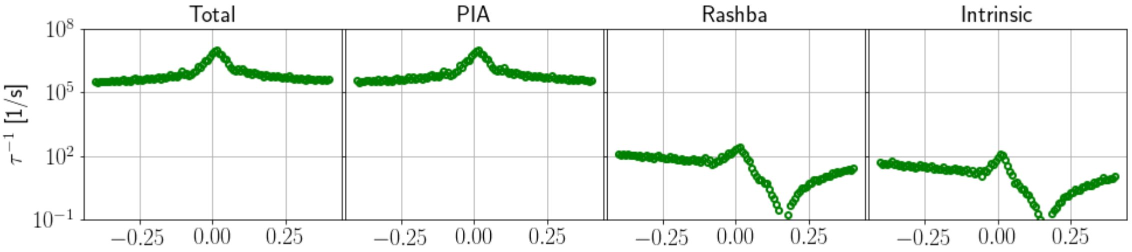

Figure 6.11: Reproduction of the results of [7] presented in Fig. 6.10, using only numerical calculations using KWANT. Similar to what is shown in Fig.6.10, in each panel we can see the results due to each spin orbit coupling term of the Hamiltonian. The exception is the leftmost panel, where we see the result obtained considering the full Hamiltonian model.

where η is the concentration of adatoms per carbon atoms, $t = 2.6$ eV is the value of hopping between first neighbors for pure graphene and a is simply the lattice constant adopted for the graphene structure [7].

In Fig.6.10 we can see the results for the spin relaxation rate published in [7]. Such results served us as reference to validate the implementation of the SOC terms in the Hamiltian. Our results is presented in the Fig. 6.11 from which one can easily see an apparently perfect match between our results and those in Fig.6.10. In addition to that, we also have obtained a confirmation for the quality of our results by comparing the results for the spin-relaxation anisotropy, presented in the figures 6.12 (from [7]) and 6.13.

It is of our interest to investigate the situation where the magnetic moment of the

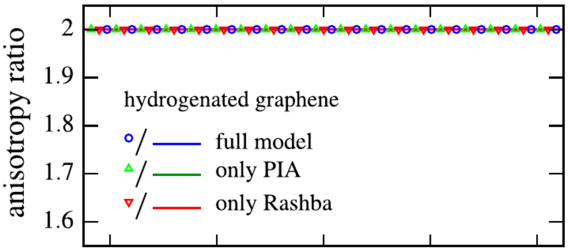

Figure 6.12: Figure extracted from the referece [7]. Calculated spin-relaxation anisotropy as the defined ratio of $1/\tau_s$ for electron spins out-of-plane and in-plane for hydrogenated graphene. The symbols representing the numerical results and solid lines the analytical model. The anisotropy here is 2 as expected spin-orbit fields with no role played by the intrinsic coupling.

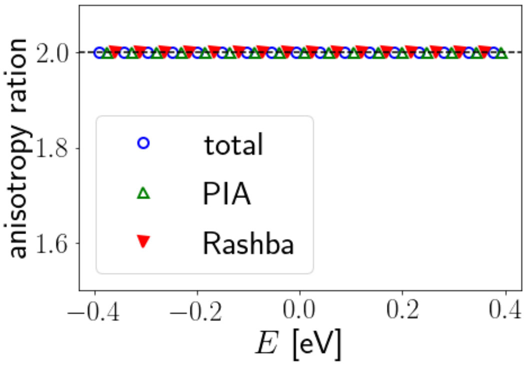

Figure 6.13: Calculated spin-relaxation anisotropy using the numerical results from KWANT. The obtained result matches the expected anisotropy of 2 obtained by Green's functions calculation [7] presented above.

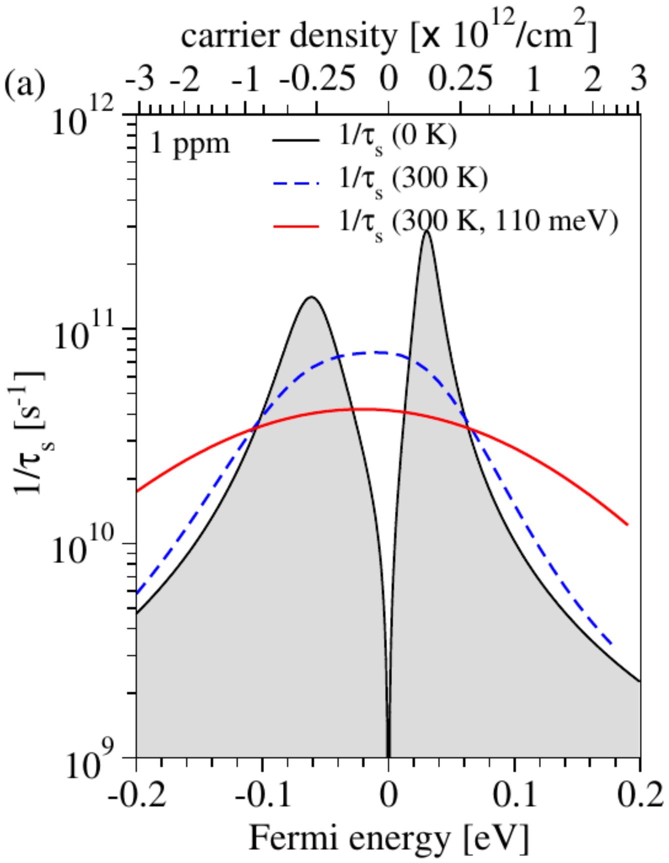

Figure 6.14: Figure from [8] where we can see the spin relaxation rate in graphene with magnetic impurities for different temperatures calculated using the T-matrix formalism. The value of the exchange coupling adopted was $J = -0.4$ eV and the impurity concentration is indicated in the figure.

adatoms are also considered. To add such an aspect in our calculations we had to include an exchange term in the Hamiltian, which is given by

$$H_{ex} = -J\hat{\mathbf{s}} \cdot \hat{\mathbf{S}} = -J(\hat{s}_x \otimes \hat{S}_x + \hat{s}_y \otimes \hat{S}_y + \hat{s}_z \otimes \hat{S}_z), \tag{6.10}$$

where $\hat{s}_i$ stands for the spin operators for the electron in the impurity site while $\hat{S}_i$ model the intrinsic magnetic moment.

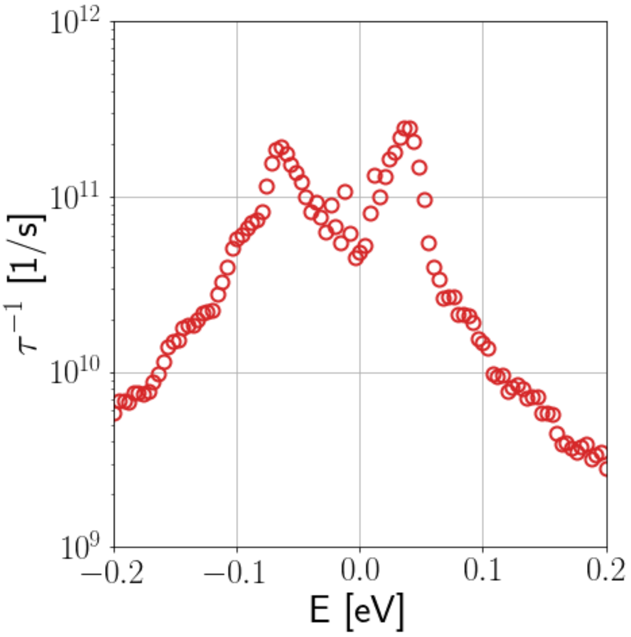

Figure 6.15: Numerical results for the spin relaxation rate obtained purelly by extracting the transmission and reflection coefficients from KWANT calculations. We have adopted the same parameters used in the reference [8]: exchange coupling given by $J = -0.4$ eV and the impurity concentration given by $\eta \sim 1$ ppm.

Chapter 7

Conclusions and final remarks

In summary, as presented in chapter 3, we studied the behavior of topological edge states in an realistic effective electronic model for InAs/GaSb quantum wells in the presence of an applied electric field. Using a $\mathbf{k}\cdot\mathbf{p}$ approach, were able to derive a realistic low-energy BHZ-like model for the system and probe the electric-field driven topological transition of quantum spin Hall phase of InAs/GaSb quantum-well systems. In this context, one of our main results is establishing that the electric-field-driven energy oscillations in the edge states in narrow systems are a clear signature of the onset of the topological phase. Such oscillations are related to intra-edge coupling between the states localized on opposite edges.

More interestingly, we are able to provide an ansatz for the edge states as a function of the electric field with the same formal structure of those found in exponentially localized Majorana edge modes as a function of the magnetic field. Moreover other topological systems with exponentially localized edge modes. With this, we were able to find analytical expressions for the localization length and wave vector behave as a function of the electric field, which nicely match our numerical results.

We are confident our results can motivate experimental search to investigate such oscillations in edge state conductance experiments, which could be an additional element in confirming for the presence of topologically-protected helical edge modes in InAs/GaSb quantum-well devices. Although a full transport calculation is beyond the scope of the present paper, we believe that conductance maps from a four-probe set up with front- and back-gates can show the oscillatory pattern consistent with our results.

The key ingredient in such experiments would be the enhancement of the coupling between edge states. We believe this could be achieved by adding a sub-micron lateral constriction (similar to that of a quantum point contact) in the device's Hall bar. The oscillations would appear in four-terminal experiments where both the density and the electric field can be tuned, a procedure similar to that of Ref. [36]. As such, a conductance map as a function of both front- and back-gates should show oscillations in the topological region near charge neutrality.

In chapter 4, by investigating a symmetrical quantum well, we observed the tunability of the topological phase by verifying the presence of the electric-field driven topological transition in this system. By adopting dissimilar Hamiltonians for the leads and the scattering region, the numerical quantum transport calculations have shown the formation of current-circulating patterns that are accompanied to peaks of conductance. Such a Fabry-Perot analogous is similar to what is observed in systems where the scattering region have a narrower width in comparison with the leads [64] or when the band structure of the leads mismatch the band structure for the scattering region by the application of a gate voltage [76].

Among the several possible directions to the exciton project, we include the inverstigation of excitonic states using a $\mathbf{k}\cdot\mathbf{p}$ Hamiltonian for the TMDC monolayer with Rashba SOC. Besides the case with Rashba SOC, we also intend to explore the recently predicted case where excitons are composed by quasi-particles with negative mass [77].

On the weak localization in hydrogenated Graphene, some important steps have to be executed in this early stage of the project. First and foremost, we need to benchmark our kwant code using published results as comparison. Once we have confidence in our code, the idea is to introduce $N > 1$ adatoms and through magnetoresistance calculations, to observe weak localization.

Appendix A

Quantum transport: Landauer's approach

A.1 Problem formulation

Fundamentally speaking, to describe a nanoscopic system composed by a battery (electron source) and a scattering region, we need a total Hamiltonian given by

$$\hat{H}_{\text{tot}} = \hat{H}_S + \hat{H}_{\text{battery}} + \hat{H}_{\text{int}} = \hat{H}_S \otimes \hat{1}_{\text{battery}} + \hat{1}_S \otimes \hat{H}_{\text{battery}} + \hat{H}_{\text{int}}, \tag{A.1}$$

where $\hat{H}_{\text{int}}$ describes the interaction between the scattering region and the battery, which, by their turn, are described by the operators $\hat{H}_S$ and $\hat{H}_{\text{battery}}$ respectively. By battery we mean every component of the circuit that is external to the nanojunction.

First approximation: open quantum system

Due to the complexity of writing an operator that describes the battery in a precise manner, what is usually done is to replace the idea of a bettery for the concept of an open system with two electron reservoirs. To stablish a charge current between such reservoirs, it is necessary that they have an unbalenced chemical potential. This unbalence are called the *bias* of the system.

$$V = \frac{\mu_L - \mu_R}{e} \tag{A.2}$$

In other words, considering a density operator that could describe the total system (including the battery) $\hat{\rho}(t)$, the battery replacement for two electron reservoirs is equivalent to perform a trace over the battery degrees of freedom.

$$\hat{\rho}_S(t) = \mathrm{Tr}_{\mathrm{battery}} \left\{ \hat{\rho}_{tot}(t) \right\} \tag{A.3}$$

In this way, making a couple of other considerations about the battery degrees of freedom we could derive the Lindblad equation:

$$\frac{d\hat{\rho}_S(t)}{dt} = \mathcal{L}\hat{\rho}_S(t) \tag{A.4}$$

and then, we would be able to find a solution once an initial condition and an appropriate super-operator $\mathcal{L}$ were provided.

Second approximation: Ideal steady state

Assuming that the equation given by A.4 admit a stationary solution, where the current steady state can be measured at all times instead of just as time average. In other words

$$\langle \hat{I} \rangle_t = \mathrm{Tr} \left\{ \hat{\rho}_S(t) \hat{I} \right\} \to \mathrm{Tr} \left\{ \hat{\rho}_S^{ss} \hat{I} \right\} = \langle \hat{I} \rangle = \text{ constante },\tag{A.5}$$

we can concentrate ourselves in the limit scenario, adopting the $\hat{\rho_S^{ss}}$ instead of the time-dependent density operator $\hat{\rho}_S(t)$.

Third approximation: Boundary condition

We are going to abandon the idea of solving the quantum open system altogether and, instead of that, focus in solving the problem of a closed, although infinite, system. The strategy for that is to explore the boundary conditions of the system. Since we are interested in the stationary solution, the reservoirs role become to prepare wave packages that move towards the scattering region and, after that, go away of the system keeping the current constant. In this way, the system Hamiltonian will describes two infinite *leads* and a scattering system.

Fourth approximation: Mean field

We will also consider the approximation where the system's Hamiltonian may be witten as

$$\hat{H}_S = \hat{H}^{mf} + \hat{V}, \tag{A.6}$$

where $\hat{H}^{mf}$ is the individual electrons Hamiltonian in the presence of a mean field produced by every other electrons and the ions that make up the scattering system, and in the operator $\hat{V}$ we will concentrate every contribution that is not compreended by the mean field approximation.

In this work, the Hamiltonian adopted will be defined by the $\mathbf{k}\dot{\mathbf{p}}$ theory. In this perturbative approximation, we are going to negect the electron-electron interactions altogether and the ionic landscape will be translated in terms of an electronic effective mass. The spin-orbit coupling and the lattice symmetries will be considered by the Kane model [61] for the binary compounds of interest (GaSb and InAs).

Fifth approximation: Independent channels

This last approximation relies on the assumption that our system is connected to charge reservoirs, which are in thermal equilibrium. By considering our system as being in contact with an environment, we are allowed to neglect the correlations between the single particle states. In other words, we need to assume that the system have evolved into a incoherent (or Independent) set of (single-particle) channels. Where by channel we mean a set of quantum numbers that describes completely a scattering solution.

Another important consideration is that regarding how such incoherent states are occupied. The assumption assumed in the Landauer formulation is that the charge carriers injected from the left reservoir (right-moving electrons) has the occupancy given by the Fermi-Dirac distribution

$$f_L(E) = \frac{1}{e^{(E-\mu_L)/k_B T} + 1}, \tag{A.7}$$

while the electrons from the right reservoir (left-moving) have the same distribution but with different local chemical potential:

$$f_R(E) = \frac{1}{e^{(E-\mu_R)/k_B T} + 1}. \tag{A.8}$$

Following the definitions above, one can write the single-particle statistical operator for the scattering problem as the sum of the operator for the left-moving and the operator for the right-moving particles:

$$\hat{\rho}_S^{ss} = \sum_L |\Psi^L\rangle f_L(E) \langle \Psi^L| + \sum_R |\Psi^R\rangle f_R(E) \langle \Psi^R| \tag{A.9}$$

Bibliography

[1] B. A. Bernevig, T. L. Hughes, and S.-C. Zhang, "Quantum spin hall effect and topological phase transition in hgte quantum wells," *Science*, vol. 314, no. 5806, pp. 1757–1761, 2006.

[2] M. König, S. Wiedmann, C. Brüne, A. Roth, H. Buhmann, L. W. Molenkamp, X.-L. Qi, and S.-C. Zhang, "Quantum spin hall insulator state in hgte quantum wells," *Science*, vol. 318, no. 5851, pp. 766–770, 2007.

[3] C. Liu, T. L. Hughes, X.-L. Qi, K. Wang, and S.-C. Zhang, "Quantum spin hall effect in inverted type-ii semiconductors," *Physical review letters*, vol. 100, no. 23, p. 236601, 2008.

[4] B. Scharf, A. Matos-Abiague, and J. Fabian, "Magnetic properties of hgte quantum wells," *Physical Review B*, vol. 86, no. 7, p. 075418, 2012.

[5] G. M. Sipahi, T. Campos, and M. A. T. Sandoval, "Tunable band gap inversion in broken gap quantum wells," *Proceedings of the 18th Brazilian Workshop on Semiconductor Physics*, 2018.

[6] S. Irmer, D. Kochan, J. Lee, and J. Fabian, "Resonant scattering due to adatoms in graphene: Top, bridge, and hollow positions," *Physical Review B*, vol. 97, no. 7, p. 075417, 2018.

[7] J. Bundesmann, D. Kochan, F. Tkatschenko, J. Fabian, and K. Richter, "Theory of spin-orbit-induced spin relaxation in functionalized graphene," *Physical Review B*, vol. 92, no. 8, p. 081403, 2015.

[8] D. Kochan, M. Gmitra, and J. Fabian, “Spin relaxation mechanism in graphene: resonant scattering by magnetic impurities,” *Physical review letters*, vol. 112, no. 11, p. 116602, 2014.

[9] P. Anderson, “Basic notions of condensed matter physics (boulder, co,” 1997.

[10] L. D. Landau, E. M. Lifshitz, and L. P. Pitaevskii, *Statisticheskaia fizika*, vol. 5. Pergamon, 1980.

[11] K. v. Klitzing, G. Dorda, and M. Pepper, “New method for high-accuracy determination of the fine-structure constant based on quantized hall resistance,” *Physical Review Letters*, vol. 45, no. 6, p. 494, 1980.

[12] R. B. Laughlin, “Quantized hall conductivity in two dimensions,” *Physical Review B*, vol. 23, no. 10, p. 5632, 1981.

[13] D. J. Thouless, M. Kohmoto, M. P. Nightingale, and M. den Nijs, “Quantized hall conductance in a two-dimensional periodic potential,” *Physical review letters*, vol. 49, no. 6, p. 405, 1982.

[14] M. Nakahara, *Geometry, topology and physics*. CRC Press, 2003.

[15] F. D. M. Haldane, “Model for a quantum hall effect without landau levels: Condensed-matter realization of the" parity anomaly",” *Physical review letters*, vol. 61, no. 18, p. 2015, 1988.

[16] C. L. Kane and E. J. Mele, “Quantum spin hall effect in graphene,” *Physical review letters*, vol. 95, no. 22, p. 226801, 2005.

[17] C. L. Kane and E. J. Mele, “Z 2 topological order and the quantum spin hall effect,” *Physical review letters*, vol. 95, no. 14, p. 146802, 2005.

[18] L. Fu and C. L. Kane, “Topological insulators with inversion symmetry,” *Physical Review B*, vol. 76, no. 4, p. 045302, 2007.

[19] C.-C. Liu, W. Feng, and Y. Yao, “Quantum spin hall effect in silicene and two-dimensional germanium,” *Physical review letters*, vol. 107, no. 7, p. 076802, 2011.

[20] Z. Liu, C.-X. Liu, Y.-S. Wu, W.-H. Duan, F. Liu, and J. Wu, “Stable nontrivial z 2 topology in ultrathin bi (111) films: a first-principles study,” *Physical review letters*, vol. 107, no. 13, p. 136805, 2011.

[21] X. Qian, J. Liu, L. Fu, and J. Li, “Quantum spin hall effect in two-dimensional transition metal dichalcogenides,” *Science*, vol. 346, no. 6215, pp. 1344–1347, 2014.

[22] F. Reis, G. Li, L. Dudy, M. Bauernfeind, S. Glass, W. Hanke, R. Thomale, J. Schäfer, and R. Claessen, “Bismuthene on a sic substrate: A candidate for a high-temperature quantum spin hall material,” *Science*, vol. 357, no. 6348, pp. 287–290, 2017.

[23] A. Roth, C. Brüne, H. Buhmann, L. W. Molenkamp, J. Maciejko, X.-L. Qi, and S.-C. Zhang, “Nonlocal transport in the quantum spin hall state,” *Science*, vol. 325, no. 5938, pp. 294–297, 2009.

[24] L. Du, T. Li, W. Lou, X. Wu, X. Liu, Z. Han, C. Zhang, G. Sullivan, A. Ikhlassi, K. Chang, *et al.*, “Tuning edge states in strained-layer inas/gainsb quantum spin hall insulators,” *Physical review letters*, vol. 119, no. 5, p. 056803, 2017.

[25] S. S. Krishtopenko and F. Teppe, “Quantum spin hall insulator with a large bandgap, dirac fermions, and bilayer graphene analog,” *Science advances*, vol. 4, no. 4, p. eaap7529, 2018.

[26] T. Campos, M. T. Sandoval, L. Diago-Cisneros, and G. Sipahi, “Electrical tuning of helical edge states in topological multilayers,” *Journal of Physics: Condensed Matter*, vol. 31, no. 49, p. 495501, 2019.

[27] C. W. Groth, M. Wimmer, A. R. Akhmerov, and X. Waintal, “Kwant: a software package for quantum transport,” *New Journal of Physics*, vol. 16, no. 6, p. 063065, 2014.

[28] D. S. Fisher and P. A. Lee, “Relation between conductivity and transmission matrix,” *Physical Review B*, vol. 23, no. 12, p. 6851, 1981.

[29] D. N. F. Sanches and L. G. G. d. V. D. d. Silva, “Transporte eletrônico em isolantes topológicos 2d,” Master’s thesis, Universidade de São Paulo, 2017.

[30] I. Knez, R.-R. Du, and G. Sullivan, “Evidence for helical edge modes in inverted inas/gasb quantum wells,” *Physical review letters*, vol. 107, no. 13, p. 136603, 2011.

[31] H. Sakaki, L. Chang, R. Ludeke, C.-A. Chang, G. Sai-Halasz, and L. Esaki, “In1- x ga x as-gasb1- y as y heterojunctions by molecular beam epitaxy,” *Applied Physics Letters*, vol. 31, no. 3, pp. 211–213, 1977.

[32] M. H. de Medeiros, R. L. Teixeira, G. M. Sipahi, and L. G. D. da Silva, “Electric field induced edge-state oscillations in inas/gasb quantum wells,” *Physical Review B*, vol. 104, no. 19, p. 195307, 2021.

[33] L.-H. Hu, C.-X. Liu, D.-H. Xu, F.-C. Zhang, and Y. Zhou, “Electric control of inverted gap and hybridization gap in type-ii inas/gasb quantum wells,” *Physical Review B*, vol. 94, no. 4, p. 045317, 2016.

[34] I. Knez, R. R. Du, and G. Sullivan, “Finite conductivity in mesoscopic hall bars of inverted inas/gasb quantum wells,” *Phys. Rev. B*, vol. 81, p. 201301(R), May 2010.

[35] L. Du, I. Knez, G. Sullivan, and R.-R. Du, “Robust helical edge transport in gated $\mathrm{InAs}/\mathrm{GaSb}$ bilayers,” *Phys. Rev. Lett.*, vol. 114, p. 096802, Mar 2015.

[36] F. Qu, A. J. A. Beukman, S. Nadj-Perge, M. Wimmer, B.-M. Nguyen, W. Yi, J. Thorp, M. Sokolich, A. A. Kiselev, M. J. Manfra, C. M. Marcus, and L. P. Kouwenhoven, “Electric and magnetic tuning between the trivial and topological phases in inas/gasb double quantum wells,” *Phys. Rev. Lett.*, vol. 115, p. 036803, Jul 2015.

[37] F. Nichele, M. Kjaergaard, H. J. Suominen, R. Skolasinski, M. Wimmer, B.-M. Nguyen, A. A. Kiselev, W. Yi, M. Sokolich, M. J. Manfra, F. Qu, A. J. A. Beukman, L. P. Kouwenhoven, and C. M. Marcus, “Giant spin-orbit splitting in inverted $\mathrm{InAs}/\mathrm{GaSb}$ double quantum wells,” *Phys. Rev. Lett.*, vol. 118, p. 016801, Jan 2017.

[38] K. Suzuki, Y. Harada, K. Onomitsu, and K. Muraki, “Edge channel transport in the inas/gasb topological insulating phase,” *Phys. Rev. B*, vol. 87, p. 235311, Jun 2013.

[39] K. Suzuki, Y. Harada, K. Onomitsu, and K. Muraki, “Gate-controlled semimetal-topological insulator transition in an inas/gasb heterostructure,” *Phys. Rev. B*, vol. 91, p. 245309, Jun 2015.

[40] M. Kim, C. H. Kim, H.-S. Kim, and J. Ihm, “Topological quantum phase transitions driven by external electric fields in sb2te3 thin films,” *PNAS*, vol. 109, no. 3, pp. 671–674, 2012.

[41] J. L. Collins, A. Tadich, W. Wu, L. C. Gomes, J. N. B. Rodrigues, C. Liu, J. Hellerstedt, H. Ryu, S. Tang, S.-K. Mo, S. Adam, S. A. Yang, M. S. Fuhrer, and M. T. Edmonds, “Electric-field-tuned topological phase transition in ultrathin na3bi,” *Nature*, vol. 564, no. 7736, pp. 390–394, 2018.

[42] M. Karalic, S. Mueller, C. Mittag, K. Pakrouski, Q. Wu, A. A. Soluyanov, M. Troyer, T. Tschirky, W. Wegscheider, K. Ensslin, and T. Ihn, “Experimental signatures of the inverted phase in inas/gasb coupled quantum wells,” *Phys. Rev. B*, vol. 94, p. 241402(R), Dec 2016.

[43] M. Karalic, C. Mittag, T. Tschirky, W. Wegscheider, K. Ensslin, and T. Ihn, “Lateral p-n junction in an inverted $\mathrm{InAs}/\mathrm{GaSb}$ double quantum well,” *Phys. Rev. Lett.*, vol. 118, p. 206801, May 2017.

[44] F. Nichele, H. J. Suominen, M. Kjaergaard, C. M. Marcus, E. Sajadi, J. A. Folk, F. Qu, A. J. A. Beukman, F. K. de Vries, J. van Veen, S. Nadj-Perge, L. P. Kouwenhoven, B.-M. Nguyen, A. A. Kiselev, W. Yi, M. Sokolich, M. J. Manfra, E. M. Spanton, and K. A. Moler, “Edge transport in the trivial phase of InAs/GaSb,” *New Journal of Physics*, vol. 18, p. 083005, jul 2016.

[45] B.-M. Nguyen, A. A. Kiselev, R. Noah, W. Yi, F. Qu, A. J. A. Beukman, F. K. de Vries, J. van Veen, S. Nadj-Perge, L. P. Kouwenhoven, M. Kjaergaard, H. J. Suominen, F. Nichele, C. M. Marcus, M. J. Manfra, and M. Sokolich, “Decoupling edge versus bulk conductance in the trivial regime of an $\mathrm{InAs}/\mathrm{GaSb}$ double quantum well using corbino ring geometry,” *Phys. Rev. Lett.*, vol. 117, p. 077701, Aug 2016.

[46] S. Das Sarma and H. Pan, “Disorder-induced zero-bias peaks in majorana nanowires,” *Phys. Rev. B*, vol. 103, p. 195158, May 2021.

[47] S. Das Sarma, J. D. Sau, and T. D. Stanescu, “Splitting of the zero-bias conductance peak as smoking gun evidence for the existence of the majorana mode in a superconductor-semiconductor nanowire,” *Phys. Rev. B*, vol. 86, p. 220506(R), Dec 2012.

[48] C.-K. Chiu, J. D. Sau, and S. Das Sarma, “Conductance of a superconducting coulomb-blockaded majorana nanowire,” *Phys. Rev. B*, vol. 96, p. 054504, Aug 2017.

[49] T. Devakul, Y. H. Kwan, S. L. Sondhi, and S. A. Parameswaran, “Quantum oscillations in the zeroth landau level and the serpentine landau fan,” *arXiv:2101.05294*, 2021.

[50] E. Kane, *The* $\mathbf{k}\cdot\mathbf{p}$ *method*, vol. 1. Amsterdam: Elsevier, 1966.

[51] S. C. P. Rodrigues, L. M. R. Scolfaro, J. R. Leite, and G. M. Sipahi, “Valence band structure of cubic algan/gan superlattices,” *Applied Physics Letters*, vol. 76, no. 8, pp. 1015–1017, 2000.

[52] S. C. P. Rodrigues, M. N. d’Eurydice, G. M. Sipahi, L. M. R. Scolfaro, and E. F. da Silva, “White light emission from p-doped quaternary (alinga)n-based superlattices: Theoretical calculations for the cubic phase,” *Journal of Applied Physics*, vol. 101, no. 11, p. 113706, 2007.

[53] C. M. O. Bastos, F. P. Sabino, G. M. Sipahi, and J. L. F. Da Silva, “A comprehensive study of g-factors, elastic, structural and electronic properties of iii-v semiconductors using hybrid-density functional theory,” *Journal of Applied Physics*, vol. 123, no. 6, p. 065702, 2018.

[54] P.-O. Löwdin, “A note on the quantum-mechanical perturbation theory,” *The Journal of Chemical Physics*, vol. 19, no. 11, pp. 1396–1401, 1951.

[55] F. Zhang, ed., *The Schur Complement and Its Applications*. Numerical methods and algorithms, Berlin: Springer, 2005.

[56] S.-Q. Shen, *Topological Insulators: Dirac Equation in Condensed Matters*. Berlin: Springer, 2012.

[57] D.-Y. Ting, D. Collins, E. Yu, D. Chow, and T. McGill, "Large peak current densities in novel resonant interband tunneling heterostructures," *Applied physics letters*, vol. 57, no. 12, pp. 1257–1259, 1990.

[58] D. Z.-Y. Ting and X. Cartoixa, "Resonant interband tunneling spin filter," *Applied physics letters*, vol. 81, no. 22, pp. 4198–4200, 2002.

[59] G. Sai-Halasz, L. Esaki, and W. Harrison, "Inas-gasb superlattice energy structure and its semiconductor-semimetal transition," *Physical Review B*, vol. 18, no. 6, p. 2812, 1978.

[60] H. Kroemer, "The 6.1 a family (inas, gasb, alsb) and its heterostructures: a selective review," *Physica E: Low-dimensional Systems and Nanostructures*, vol. 20, no. 3-4, pp. 196–203, 2004.

[61] G. Bastard *et al.*, "Wave mechanics applied to semiconductor heterostructures," 1988.

[62] P.-O. Löwdin, "Studies in perturbation theory: Part i. an elementary iteration-variation procedure for solving the schrödinger equation by partitioning technique," *Journal of Molecular Spectroscopy*, vol. 10, no. 1-6, pp. 12–33, 1963.

[63] R. Winkler, "Quasi-degenerate perturbation theory," in *Spin–Orbit Coupling Effects in Two-Dimensional Electron and Hole Systems*, pp. 201–206, Springer, 2003.

[64] R. Maciel, A. Araújo, C. Lewenkopf, and G. Ferreira, "Fabry-pérot resonant vortices and magnetoconductance in topological insulator constrictions with magnetic barriers," *Physical Review B*, vol. 103, no. 20, p. 205124, 2021.

[65] S. L. Chuang, *Physics of optoelectronic devices*. New York, NY: Wiley-Interscience, 1995.

[66] N. Nakanishi, "A general survey of the theory of the bethe-salpeter equation," *Progress of Theoretical Physics Supplement*, vol. 43, pp. 1–81, 1969.

[67] M. Rohlfing and S. G. Louie, “Electron-hole excitations and optical spectra from first principles,” *Physical Review B*, vol. 62, no. 8, p. 4927, 2000.

[68] K. Zollner, P. E. F. Junior, and J. Fabian, “Giant proximity exchange and valley splitting in transition metal dichalcogenide/h bn/(co, ni) heterostructures,” *Physical Review B*, vol. 101, no. 8, p. 085112, 2020.

[69] B. Scharf, D. Van Tuan, I. Žutić, and H. Dery, “Dynamical screening in monolayer transition-metal dichalcogenides and its manifestations in the exciton spectrum,” *Journal of Physics: Condensed Matter*, vol. 31, no. 20, p. 203001, 2019.

[70] P. Cudazzo, I. V. Tokatly, and A. Rubio, “Dielectric screening in two-dimensional insulators: Implications for excitonic and impurity states in graphane,” *Physical Review B*, vol. 84, no. 8, p. 085406, 2011.

[71] A. Kormányos, G. Burkard, M. Gmitra, J. Fabian, V. Zólyomi, N. D. Drummond, and V. Fal’ko, “k· p theory for two-dimensional transition metal dichalcogenide semiconductors,” *2D Materials*, vol. 2, no. 2, p. 022001, 2015.

[72] T. C. Berkelbach, M. S. Hybertsen, and D. R. Reichman, “Theory of neutral and charged excitons in monolayer transition metal dichalcogenides,” *Physical Review B*, vol. 88, no. 4, p. 045318, 2013.

[73] A. Kormányos, V. Zólyomi, N. D. Drummond, and G. Burkard, “Spin-orbit coupling, quantum dots, and qubits in monolayer transition metal dichalcogenides,” *Physical Review X*, vol. 4, no. 1, p. 011034, 2014.

[74] M. Gmitra, D. Kochan, and J. Fabian, “Spin-orbit coupling in hydrogenated graphene,” *Physical review letters*, vol. 110, no. 24, p. 246602, 2013.

[75] A. Weiße, G. Wellein, A. Alvermann, and H. Fehske, “The kernel polynomial method,” *Reviews of modern physics*, vol. 78, no. 1, p. 275, 2006.

[76] D. Nanclares, L. R. Lima, C. H. Lewenkopf, and L. G. D. da Silva, “Tunable spin-polarized edge transport in inverted quantum-well junctions,” *Physical Review B*, vol. 96, no. 15, p. 155302, 2017.

[77] K.-Q. Lin, C. S. Ong, S. Bange, P. E. F. Junior, B. Peng, J. D. Ziegler, J. Zipfel, C. Bäuml, N. Paradiso, K. Watanabe, *et al.*, “Bright excitons with negative-mass electrons,” *arXiv preprint arXiv:2006.14705*, 2020.